CHALMERS

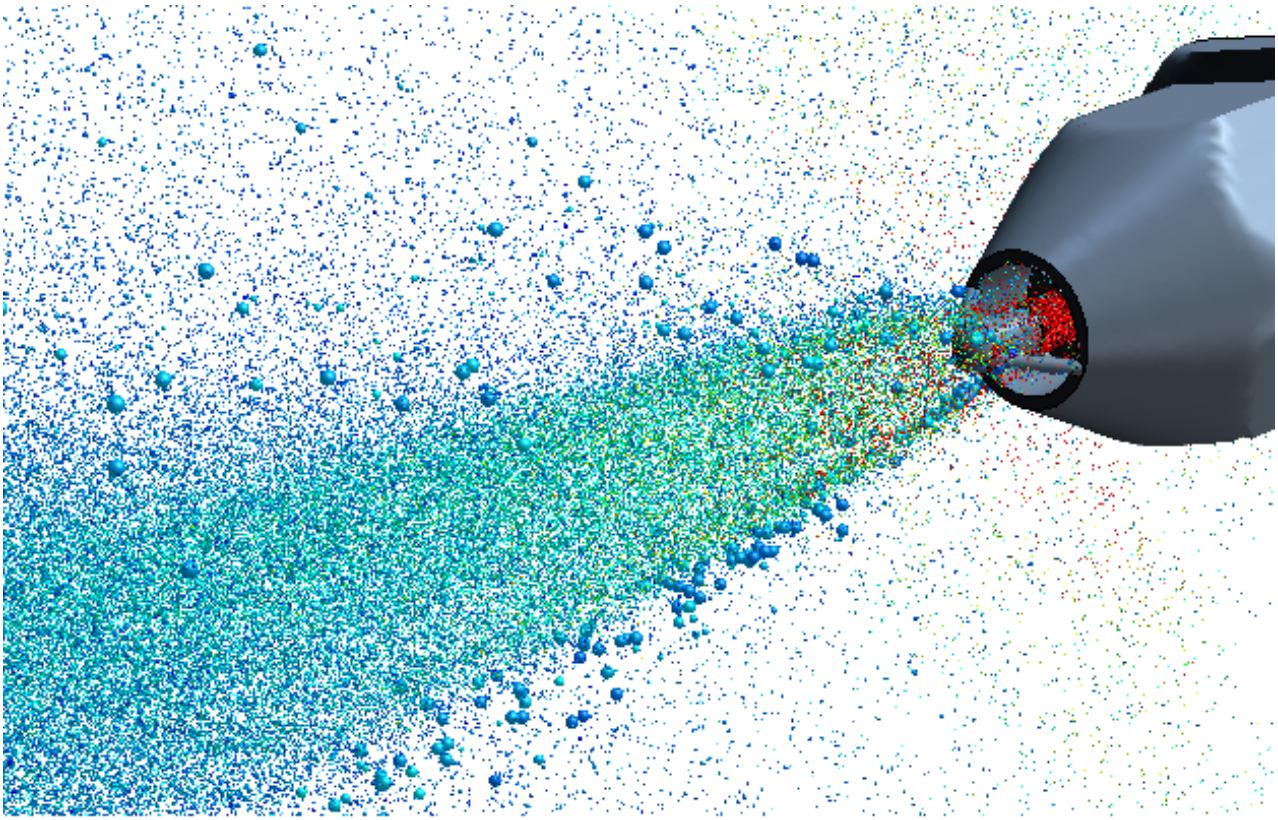

Eulerian-Lagrangian Modeling of Multicomponent Spray for Aseptic Treatment of Carton Bottles in the Food Process and Packaging Industry

Master's thesis in Applied Mechanics

TONY PERSSON

Department of Applied Mechanics
Division of Fluid Dynamics
CHALMERS UNIVERSITY OF TECHNOLOGY
Gothenburg, Sweden 2013
Master's thesis 2013:34

MASTER'S THESIS IN APPLIED MECHANICS

Eulerian-Lagrangian Modeling of Multicomponent Spray for Aseptic Treatment of Carton Bottles in the Food Process and Packaging Industry

TONY PERSSON

Department of Applied Mechanics

Division of Fluid Dynamics

CHALMERS UNIVERSITY OF TECHNOLOGY

Gothenburg, Sweden 2013

Eulerian-Lagrangian Modeling of Multicomponent Spray for Aseptic Treatment of Carton Bottles in the Food Process and Packaging Industry
TONY PERSSON

Master's thesis 2013:34
ISSN 1652-8557
Department of Applied Mechanics
Division of Fluid Dynamics
Chalmers University of Technology
SE-412 96 Gothenburg
Sweden
Telephone: +46 (0)31-772 1000

Cover:
The spray nozzle for the evaporator of the Tetra Pak A6 iLine. The point size represents real droplet diameters from 0.1 μm to 1.2 mm. The droplets are coloured from blue to red by velocity from 0 to 50 m/s.

Chalmers Reproservice
Gothenburg, Sweden 2013

Eulerian-Lagrangian Modeling of Multicomponent Spray for Aseptic Treatment of Carton Bottles in the Food Process and Packaging Industry
Master's thesis in Applied Mechanics
TONY PERSSON
Department of Applied Mechanics
Division of Fluid Dynamics
Chalmers University of Technology

Abstract

This thesis is a study of the fluid dynamic behaviour of a specific spray nozzle used in the evaporator unit of the Tetra Pak A6 iLine, as well as a sensitivity analysis and methodology development for general evaporating sprays used in industrial applications. The Tetra Pak A6 is a complete sterilisation, filling and packaging machine for the Tetra Evero Aseptic carton bottle. The package is specially designed for ambient white milk. It is developed to be more user friendly than old fashion prism shaped packages due to the easier handling and reclosing feature and more environmental friendly than plastic bottles due to the separable carton body and plastic top. A spray nozzle in the evaporator injects a high-speed liquid mixture of water and hydrogen peroxide that is evaporated, swirled down into the carton bottle and used as aseptic treatment of the inside of the package before the vapor mixture is vented out and the package is filled with beverage.

The behaviour of the multicomponent spray was numerically modeled using unsteady RANS and Lagrangian tracking of representative computational parcels of spray droplets. The simulations were performed using STAR-CCM+, a software package for computational fluid dynamic simulations.

To break down the complex fluid dynamic problem in the high-speed spray nozzle and be able to isolate and study important physical phenomenon, two different case studies with simplified geometries were performed. The first case study was a parameter and sensitivity analysis of the behaviour of a general evaporating spray in a small cubical domain. The injector is a solid cone injector originating from a single point. Responses such as penetration length, spray width, evaporated mass for the species, diameter- and velocity distributions were studied for varying spray parameters and solver settings. The second case study originates from an experimental and numerical study of wall impingement of diesel spray in an open channel with cross flow [3]. The aim of the study was to investigate the effect of droplet-droplet collisions, wall interaction and fluid film.

The conclusions from the case studies were applied to spray simulations of the nozzle and evaporator in the Tetra Pak A6. Comparison with experimental droplet velocities and diameters from laser measurements showed acceptable conformity.

The ambition is that the results from the aforementioned studies could be used for sprays in other industrial applications such as diesel or urea spray in the automotive industry since these applications use the same models for simulating spray behaviour.

Keywords: Eulerian-Lagrangian, Tetra Pak, CFD, multicomponent spray, aseptic treatment, droplets, evaporation, collisions, hydrogen peroxide, food process, packaging, liquid film, parameter sensitivity analysis, phase doppler interferometry

Preface

This report summarises the master thesis work performed by Tony Persson as a completion of the Master of Science degree in Applied Mechanics at Chalmers University of Technology in Gothenburg, Sweden. The thesis has been carried out at FS Dynamics Gothenburg during the spring 2013, in collaboration with Tetra Pak in Lund and the Department of Applied Mechanics, Division of Fluid Dynamics at Chalmers University of Technology. The research is part of a methodology development of numerical spray simulations for the Tetra Pak A6 packaging solution. The work was supervised by Ulf Engdar and Jonas Edman at FS Dynamics, opposed on by Emelie Samuelsson from the Innovative and Sustainable Chemical Engineering master programme and examined by Srdjan Sasic at Chalmers University of Technology.

This report was typeset using LaTeX

Acknowledgements

I would like to express my gratitude to the people who made this possible by adding a few lines to this thesis.

I am deeply grateful to Associate Professor Srdjan Sasic at the Department of Applied Mechanics, Division of Fluid Mechanics, for being my examiner and theoretical guide. Thanks for sparking my interest and teaching me the basic theory, approaches and modeling techniques of multiphase flow, for helping me to place the thesis in a relevant academic context and providing an objective view of the problems involved.

To all study colleges that have inspired and encouraged me to always do my best during the five years I spent at the university, regardless of whether the activity in question is a master thesis, building a formula race car, spending late nights together studying for an exam or just a pre-party for the mandatory Friday night party. Special thank you to Emilie Samuelsson for opposing on my thesis and providing me with useful feedback.

I am happy and thankful for my supervisors and Ulf Engdar and Jonas Edman for being very helpful and enthusiastic about both mine and their own work with spray simulations. I am thrilled that you let me work with this interesting and in many ways complex subject and thankful to you for trying to answer all my questions. I know I got you to think twice sometimes and I hope that you have developed your own skills and maybe widened you views by consulting me. Thanks to Ulf, I know almost as much about the bugs in STAR CCM+ and the tips and trick how get around them as the support personnel at CD-adapco do. Finally, a special expression of gratitude to Jonas for giving up his desk, computer and ergonomic chair at the office for me. I would like to show my appreciation to my new friends and colleagues at the Gothenburg office for their warming welcome and our interesting and thoughtful coffee break discussions about the important questions in life.

Thanks to Tetra Pak for providing a very complex fluid dynamics spray problem from the real world and for giving me access to their computational resources. For inviting me to a guided tour around their company premises that gave me a better understanding of the surrounding systems and the measurement techniques, processes and problems involved.

All respect to CD-adapco for providing me with Power-On-Demand license hours for STAR-CCM+ and to the helpful and skilled support engineer, Rodolfo Piccioli. Without your support the final results of this work would probably not be the same.

Many thanks to all my friends and family that supported me during my education.

Contents

1 Introduction

This research project was carried out in collaboration with Tetra Pak and FS Dynamics. Tetra Pak is an international food processing and packaging company, founded in Sweden in 1951 and built on the well known tetrahedral packing idea for cream and milk packages. Tetra Pak develops and provides complete solutions for processing, packaging and distribution of food and beverages to business customers worldwide. Their product range includes automated machine lines that complete the process by folding and producing carton packages, aseptically sterilizing products and packages, filling and closing packages and distributing the packages to the storage facility. The aseptic treatment enables liquid food to maintain its color, texture, natural taste and nutrition value for as long as one year without preservatives or refrigeration. The process lets food producing companies reach out to customers in remote locations.

FS Dynamics (Fluid Structural Dynamics) is a consultancy specializing in advanced numerical simulations and analysis of engineering problems using computational fluid dynamics (CFD) and finite element analysis (FEA), with recent applications in fluid-structure interaction (FSI) and automated design optimisation. Founded in Sweden 2004, FS Dynamics is one of the largest providers of qualified CFD simulations in Scandinavia, with offices in Sweden, Denmark and Finland. FS Dynamics provides technical services to development intensive industrial enterprises over a broad range of industries including automotive, aerospace and marine, nuclear and wind power, food processing and packaging, among others.

1.1 Background

Numerical simulation and analysis of evaporation and other physical phenomena in multi-component spray mixtures of hydrogen peroxide (H_2O_2) and water (H_2O) is important for the understanding and development of new aseptic sterilization products for the food processing and packaging industry. It can be used to predict the performance of a new design or concept before it is manufactured and tested in a laboratory, thus reducing development cost. Numerical simulation and analysis of sprays is a growing application within several industries and the physics, knowledge and methodology can often be transferred and applied to different areas.

The Tetra Pak A6 iLine is a complete sterilisation, filling and packaging machine for the Tetra Evero Aseptic carton bottle. The package is specially designed for distribution ambient white milk. It is developed to be more user friendly than old fashion prism shaped packages due to the easier handling and reclosing feature, and more environmentally friendly than plastic bottles due to the separable carton body and plastic top.

The spray nozzle injects a high-speed liquid mixture of water and hydrogen peroxide into the top of the evaporator. The spray droplets evaporate into vapor of its components before the gas mixture is swirled down into the carton bottles and used as aseptic treatment of the inside of the package. The vapor mixture is finally vented out of the package using hot swirling sterile air and the package is filled with ambient white milk.

Phase Doppler Interferometry or PDI [23] is a measurement technique used for experimental studies of droplet size, velocity and mass flux through two dimensional laser scanning of planes perpendicular to the flow direction. Experiments on the STERIS Turbosonic nozzle #007 used in the evaporator of the Tetra Pak A6 iLine packaging solution has been performed at the OPTIGAS evaporation rig at Tetra Pak. The experimental results are to be used as a reference when comparing results from simulations of the evaporator nozzle.

This project is based on the assumption that the liquid spray mixture of water and hydrogen peroxide and the gas mixture consisting of air and the vapor produced by the evaporation of the liquid components can be modeled using an Eulerian-Lagrangian framework. This means solving the continuity and Navier-Stokes equations for the continuous gas mixture and tracking individual parcels, representing a cloud of real droplets, by solving the equations of Newtons second law of motion for of the dispersed liquid droplets. The continuous and dispersed phases are two-way coupled through source terms in the governing equations for momentum, mass and energy for the fluid. Industrial application of this type of modeling is relatively new and the modeling techniques are developed and updated every year. New algorithms combined with Moores law stating that the performance and computational power approximately doubles every second year leads to the consequence that the limit of what can be simulated is advancing every year.

The availability of previous research and literature considering numerical modeling of spray for sterilization products is very limited. Almost all models used in spray simulations were originally developed for modeling diesel injection spray for commercial road vehicles and offshore ships. Spray combustion is becoming an essential part of the transport and energy industry, driven by increasing demands to improve fuel and energy efficiencies and to reduce the emission of pollutants to the surrounding environment. These models have then been adapted to other industrial spray applications, such as water/urea spray for engine after-treatment systems in commercial vehicles, but also for sterilizing packages in the food business process industry. Spray simulations are also used for spray painting and fuel injection in gas-turbine combustion chambers of aircraft engines, among others [8].

1.2 Objective

The objective of this thesis work is to strengthen the knowledge of how to perform numerical spray simulations for industrial applications for present and future assignments at FS Dynamics. This includes finding a methodology of best practice, a good enough compromise between reasonable computational cost and sufficient simulation accuracy. The methodology is to be applied to a real industrial case to study the behaviour of a complex spray nozzle referred to as STERIS Turbosonic nozzle #007, used in the evaporator for the aseptic treatment in the Tetra Pak A6. The simulation is to be performed using the software package STAR-CCM+ from CD-adapco and the results is to be compared to experimental data obtained from 1D and 2D PDI laser scans conducted on the specific nozzle at the Tetra Pak research center.

1.3 Aseptic treatment and regulations

During aseptic packaging the packaging material and the food being processed must be sterilised before the two are joined in a sterile environment. The sterile environment means that all internal surfaces in the packaging and filling machines must be sterile during the entire processing. Tetra Pak has solved this by submerging the flat unformed packaging material into a 70 °C water bath with a concentration of 30 % hydrogen peroxide for six seconds. The liquid is then eliminated from the material using hot sterile and pressure rollers. The hot air, steam and hydrogen peroxide vapor circulates the machine internally to keep it free from potentially contaminating bacteria before and during the packaging process. The material is then folded and shaped before it is filled with ultra high temperature treated food.

Hydrogen peroxide and other regulated substances used to control the growth of microorganisms in packaged food are described in [47]. To meet the demands and regulations less than 0.5 ppm of hydrogen peroxide must be measured in distilled water immediately after being packaged under production conditions. The properties, production methods, common applications and risks of hydrogen peroxide usage to human and environmental health was reviewed by [41]

1.4 Tetra Pak A6 iLine

The Tetra Pak A6 iLine, see Figure 1.4.1, is a complete production line filling machine developed specially for the Tetra Evero Aseptic packages, the first ever aseptic carton bottle, see Figure 1.4.2. The machine is capable of producing and filling 10 000 packages per hour, making it one of the fastest injection moulding machines in the world with four single-cavity moulds. The Tetra Evero Aseptic (TEA) is a carton bottle for ambient white milk that combines the easy handling and pouring of a bottle with the environmental advantages of a carton. It has a plastic high density polyethylene (HDPE) screw cap and a volume of 1000 ml. The specific package is developed to be more environmental friendly than standard plastic bottles and includes a feature which makes it easy to tear off and recycle the top of the package separately. The different stages of the machine works as described below.

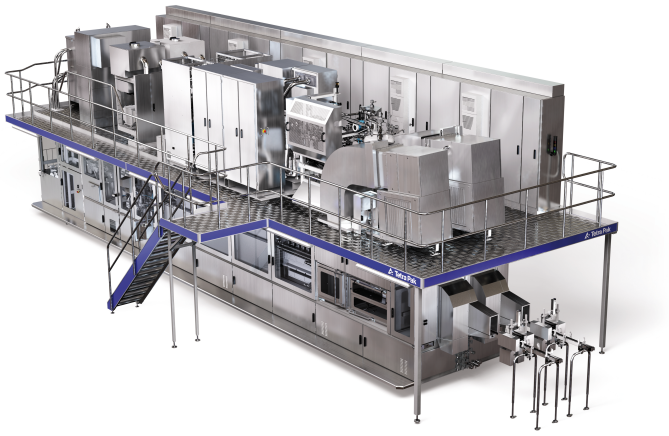

Figure 1.4.1: *Tetra Pak A6 iLine industrial filling and packaging solution for TEA [43]*

Production of the package:

- The carton material is supplied from a large roll feed
- The carton is cut into blanks, wrapped around a mould and the edge is sealed
- The capped neck at the top is injection moulded and fused together with the carton sleeve

Aseptic gas treatment:

- The folded and assembled packages are pre-heated to avoid the hydrogen dioxide from condensing on the surface inside the package
- Ambient high pressure air and a liquid mixture of water and hydrogen dioxide are injected through the nozzle
- The mixture is evaporated in a flow of hot air in the evaporator
- The aseptic gas is swirled down into the packages for a few seconds
- The aseptic sterilization mixture is ventilated out using swirling sterile air

Filling and packaging:

- The package is filled with product in four steps to minimise foaming
- The package is securely closed and ready for distribution

Figure 1.4.2: *Tetra Evero Aseptic carton bottle for ambient white milk [42]*

1.5 Problem definition

A mass flow of 80 kg/h hot air at 290 °C is supplied from a heater and passed through a swirler integrated in the evaporator connection tube, see Figure 1.5.1. The air then enters the evaporator radially from a perforated tube and passes the top of the nozzle and the thin tubes. The flow direction is then evened out by a perforated plate surrounding the nozzle head, which produces a vertical flow and a velocity of about 1 m/s.

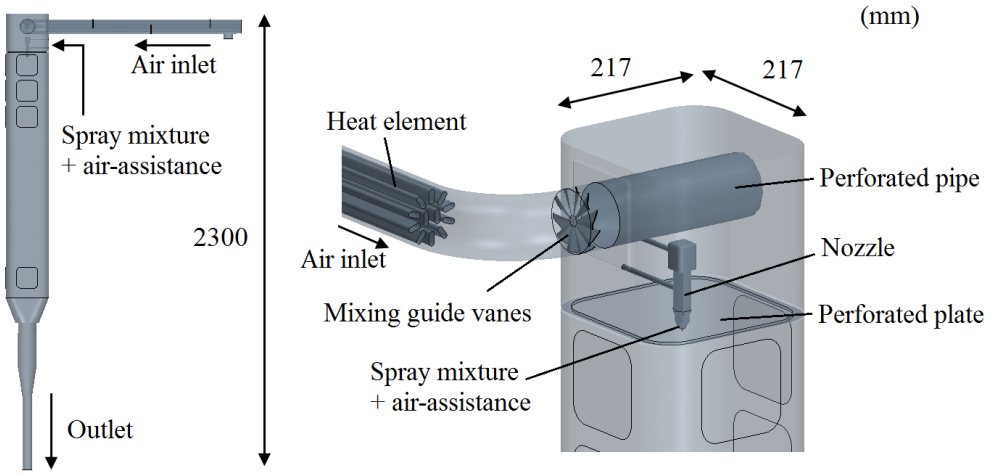

Figure 1.5.1: *Tetra Pak A6 evaporator geometry*

The nozzle, see Figure 1.5.2, is supplied by 6.2 kg/h of pressurized air at ambient temperature and 5 kg/h of a liquid mixture, consisting of 65 wt% water and 35 wt% hydrogen dioxide at ambient temperature. The figure also shows the location of the droplet measurement plane downstream of the nozzle tip. The spray exits the nozzle through a circular hole with diameter 2.54 mm. This results in a spray jet of approximately 250 m/s impinging, splashing and producing a liquid wall film on the small concave half-sphere cup with center located 4 mm downstream of the injector, all of these phenomenon being highly complex to model and simulate accurately. The high spray velocity relative to the hot air flow in combination with the density difference between the drops and the surrounding air makes the case strongly two-way coupled while the large temperature difference makes evaporation behaviour important. The performance of the evaporation system is crucial for the aseptic treatment of the packages. Unevaporated liquid droplets, containing the highly reactive oxidiser hydrogen peroxide, forming or remaining in the package could even be a risk to human health. The sterile air ventilating the packages will clear the gaseous hydrogen peroxide but there is no guarantee that liquid drops will be swirled out of the carton bottle.

Some of the boundary conditions, especially the thermal nozzle head condition and the spray temperature are uncertain and at the same time assumed to have a significant impact on the evaporator performance. The aim is to improve the modeling procedure and accuracy of the simulation without increasing computational cost.

1.6 Limitations

The simulation results will be compared to experimental data, but the objective is not to optimise modeling parameters or improve the performance of the current evaporator but rather to investigate the results of using different modeling techniques. Chemical reactions and phase changes other than evaporation of droplets and liquid film will not be modeled.

Since the goal is to strengthen the knowledge and find a best practice of how to set up and run spray simulations the focus will lie on methodology development rather than development of new theory, models and algorithms. This means that models and settings available in any version of STAR-CCM+ will exclusively be investigated and used for evaluation [5]. Since the goal is to find a good enough compromise between cost and accuracy, rather than finding the best combinations of variables using optimization algorithms, methodology for the later

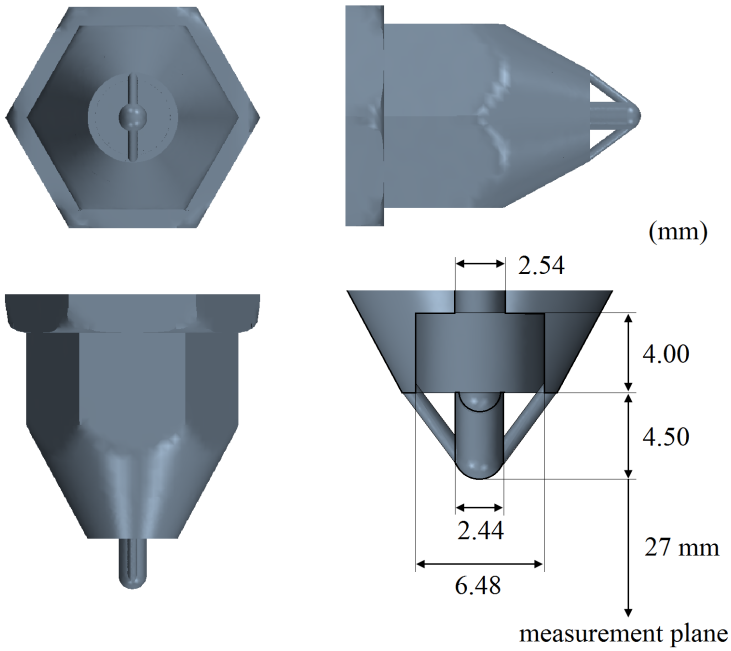

Figure 1.5.2: *Lower part of the STERIS Turbosonic nozzle #007 geometry*

will not be investigated. During the parameter sensitivity analysis part not all parameters and settings will be investigated and compared, in other words, only the most important and relevant parameters with large expected influence on the result will be considered.

Due to the unfeasible computational cost of LES or even DNS for engineering applications of multiphase flow with a discrete phase present, these types of modeling will not be assessed, only briefly introduced. Fluid-particle simulations using the Lattice Bolzmann method has become popular even though this type of modeling is relatively new and different from conventional CFD, it has shown to give satisfactory results. It is however not available in the software used and for this reason only introduced, not assessed or investigated further.

2 Computational Fluid Dynamics

The idea behind the following chapters is to provide the reader with a nomenclature and a basic understanding of the significant physical phenomena behind multiphase flow and spray simulations as well as references to further reading material. It is also meant to be used as a quick read through for CFD engineers in other fields who wants to widening their knowledge into new applications, possibly for consultancy assignments. Most of the theory is general while some parts are specific for this thesis or the software package used.

The behaviour of common fluids, such as air and water, is an everyday phenomena that most people probably have reflected on when seeing a mini tornado swirling some dust around on the street, raindrops falling from the sky or when feeling the resistance of the water when swimming or diving into the ocean. Fluid mechanics is the field within classical physics that studies fluids and the forces acting on them. It can be divided into fluid statics, fluid kinematics and fluid dynamics. Fluid dynamics is the natural science of fluids in motion and the related forces. Fluid mechanics, together with solid mechanics forms what is generally called continuum mechanics, a modeling approach that describes matter on a macroscopic level rather than using the underlying information that it is built up of atoms on a microscopic level. Fluid dynamics is an active field within research and development and the answers to many questions and unresolved problems are still to be found, especially within turbulence modeling and multiphase flow interactions.

The first two-dimensional transient simulations of fluid flow governed by the Navier-Stokes equations and solved using computers was done during the late 1950ś [13] and the first simulations of three-dimensional flow was published in the late 1960ś [15]. The theory behind it was available earlier but the progress was limited by the lack of computational resources. The same restriction is still acting today by limiting what is possible to simulate and to what level of detail. Compared to the finite element method and its tools used in solid mechanics modeling, the governing equations of CFD is more complex to solve. It has to resolve fluid motion with boundary layers and turbulence which increases the number of equations and leads to higher demands on spatial and temporal resolution and thereby computational power. Refer to [48] for more information on discretisation methods solver algortihms.

2.1 Governing equations

Fluid dynamic problems often involve complex mathematics and partial differential equations, for which analytical solutions only exist for very simple steady-state cases without turbulence. The complexity has driven the development of numerical methods and algorithms, implemented into computer software. Most commercial fluid dynamic software or codes use the field of science referred to as computational fluid dynamics or CFD to solve the motion and interaction of fluids and surfaces defined as boundary conditions. CFD is based on the assumptions from continuum mechanics that the physics of fluid dynamics of any flow can be governed by three fundamental conservation equations. These are the conservation of mass, momentum and energy that form the Navier-Stokes equations of fluid flow. For multiphase flows there is a need for an additional equation governing the conservation of species. The indices c and p indicates the continuous and particulate phase, index rel represents the slip velocity or relative velocity between the phases.

The terms in the equations for conservation and transport are generally described as the rate of change of a quantity due to convection, diffusion, dissipation and local change in time. The expressions can be explained by an example. Ink poured into a river will follow the fluid motion downstream via advection. If the ink is poured into a lake without significant water flow the ink will instead disperse and spread into the water by diffusion. Convection is the combined effect of advection and diffusion but the term advection is often used interchangeably with convection. In this master thesis the numerical simulations have been solved using the second order upwind convection scheme [48]. Dissipation represents the losses due to irreversible processes such as friction. A production term is defined as the term that creates or increases the quantity. For instance, the velocity gradient term generates turbulent kinetic energy and is thereby a production term in the transport equation for turbulent kinetic energy. Similarly the dissipation term is a destruction term in the same equation.

2.1.1 Continuity equation

The first conservation equation is commonly referred to as the mass continuity equation for a fluid

$$\frac{\partial \rho}{\partial t} + \frac{\partial (\rho u_i)}{\partial x_i} = 0$$

It states that mass can not be created or destroyed within a cell without the presence of a source or sink term.

2.1.2 Momentum equation

The momentum equation originates from Newton's second law of motion and states that the rate of change of momentum is equal to the sum of forces acting on the fluid in each direction. The instantaneous momentum equation written on Cartesian tensor notation if often refereed to as the Navier-Stokes equations:

$$\frac{\partial (\rho u_i)}{\partial t} + \frac{\partial (\rho u_i u_j)}{\partial x_j} = -\frac{\partial p}{\partial x_i} + \frac{\partial \tau_{ij}}{\partial x_j} + \rho g$$

where u is the fluid velocity vector at position x in space at time t, ρ is the density, p is the pressure and τ_{ij} is the viscous stress tensor defined using the constitutive relation for a Newtonian fluid as

$$\tau_{ij} = 2\mu \left(S_{ij} - \frac{S_{kk}\delta_{ij}}{3} \right)$$

with the instantaneous mean strain rate tensor

$$S_{ij} = \frac{1}{2} \left(\frac{\partial u_i}{\partial x_j} + \frac{\partial u_j}{\partial x_i} \right)$$

The first term in the momentum equation represents the local rate of momentum change, the second term the rate of change due to convection or fluid motion. The right hand side describes the forces acting on the fluid due to pressure gradients, shear forces and gravity. The equations originates from the Newton's second law applied to fluid motion and an assumption that for a Newtonian fluid the stress acting on a fluid volume can be written as the sum of a viscous diffusion term, proportional to the velocity gradient, and a pressure term.

2.1.3 Energy equation

The third conservation equation is the energy equation, stating that the rate of change of energy is equal to the net sum of the added heat and the performed work as

$$\frac{\partial (\rho e)}{\partial t} + \frac{\partial (\rho e u_j)}{\partial x_j} = -p\frac{\partial u_j}{\partial x_j} + \frac{\partial}{\partial x_j} \left(\lambda \frac{\partial T}{\partial x_k} \right) + \Phi + S_E$$

Where e is internal energy and λ is the heat conductivity of the fluid. The first term represents the local rate of change of energy, the second term the rate of change due to convection. The terms on the right hand side describes the rate of change due to deformation work, heat transfer, dissipation and local energy sources. It conserves energy in the system by balancing temperature, pressure and internal energy in each cell [48].

2.1.4 Conservation of species

For multiphase flows, mass conservation of the individual species becomes necessary. The conservation equation is defined as

$$\frac{\partial(\rho Y_i)}{\partial t} + \frac{\partial(\rho u_j Y_i)}{\partial x_j} = -\frac{\partial \rho V_{i,j} Y_i}{\partial x_j} + S_Y$$

Where the first term represents the local rate of change of mass fraction Y for species i, the second term the rate of change due to convection of the species. The terms on the right hand side represents the rate of change of mass fraction due to the diffusion velocity vector V and mass sources, such as evaporation [46].

2.1.5 Equation of state

In compressible flows, the equations of state for a perfect or ideal gas provide the link from the momentum and continuity equation to the energy equation as $p = \rho RT$ and $i = c_v T$, where i is the specific internal energy and c_v is the specific heat coefficient at constant volume. For incompressible flow with low Mach numbers the density is assumed to be constant, making the link between the equations unnecessary. This means that the flow field can be solved without using the energy equation. In cases where the temperature field is of importance, such as in heat transfer problems, the energy equation can be solved parallel to the momentum and continuity equation [48]. The assumption of incompressible flow has not been utilised in the numerical simulations performed in this thesis, due to its invalidity at high air velocities.

2.2 Reynolds-Averaged Navier-Stokes and turbulence modeling

Turbulence is characterised by seemingly chaotic and random three dimensional fluid dynamic motion called vorticity. Turbulent flow arise at high Reynolds numbers where the inertial forces dominate the viscous forces and often produces chaotic eddies over a wide length scale spectra, vorticity and vortex shedding. The turbulent behaviour, when present, often dominates the effect of all other flow physics and the diffusive property enhances mass, momentum and heat transport. This affects and increases energy dissipation, species mixing, heat transfer and drag forces. Turbulence is highly dissipative, viscous shear stresses perform deformation work, causes the large turbulent eddies to fall apart and form smaller eddies. During this process, turbulent kinetic energy leaves the eddies as heat diffusing into the fluid until the size of the eddy reaches the Kolmogorov length scale, representing the smallest eddies in the flow, where the remaining of the kinetic energy is assumed to dissipate into heat [48].

The Navier-Stokes equations can be rewritten by the incorporation of Reynolds decomposition, a mathematical technique within the theory of turbulence to separate the steady and fluctuating parts of a given quantity into two terms, for instance $u_i = \overline{u_i} + u_i'$ and $p_i = \overline{p_i} + p_i'$ where the bar represents a Reynolds time-averaged quantity and the prime represents the fluctuating component. With the time average of a fluctuation $\overline{u_i'} = 0$ and the average of a mean component $\overline{\overline{u_i}} = \overline{u_i}$ this implementation gives the simplified momentum equation referred to as the Reynolds-Averaged Navier-Stokes, or RANS equation as

$$\frac{\partial \overline{\rho u_i}}{\partial t} + \overline{u}_j \frac{\partial \overline{\rho u_i}}{\partial x_j} = \frac{\partial}{\partial x_j}\left[-\frac{\partial \overline{p}\delta_{ij}}{\partial x_i} + \mu\left(\frac{\partial \overline{u}_i}{\partial x_j} + \frac{\partial \overline{u}_j}{\partial x_i}\right) - \rho\overline{u_i' u_j'}\right]$$

The last term $-\rho\overline{u_i' u_j'}$ in the equation describes the momentum transport by turbulence and is referred to as the Reynolds stress tensor. This nonlinear and symmetric second order tensor term requires additional modeling to close and be able to solve the RANS equation. The term has been modeled using several different approaches using zero, one, two or more equations. The most commonly used turbulence models utilise a two equation approach. A transport equation is a partial differential equation containing a time dependent term, a convection term, a diffusion term and source terms.

The Boussinesq assumption [34] introduces a turbulent viscosity or eddy viscosity to characterise the transport and dissipation of energy at the small turbulent scales that are not resolved in RANS. The assumption is that the Reynolds stresses can be related to the mean strain tensors as

$$\sigma_{ij} = -\rho\overline{u_i' u_j'} = 2\mu_t S_{ij} - \frac{2}{3}\rho k\delta_{ij} = \mu_t\left(\frac{\partial U_i}{\partial x_j} + \frac{\partial U_j}{\partial x_i}\right) - \frac{2}{3}\rho k\delta_{ij}$$

This hypothesis is the base of most turbulence models. Other modeling approaches for resolving turbulence are DNS, see Section 3.4, LES Section 3.5 and the Lattice Boltzmann method, Section 3.6.

2.2.1 $k-\varepsilon$ realizable

The $k-\varepsilon$ is the most widely used turbulence model for industrial applications. It is a two-equation model based on the Boussinesq assumption, with transport equations for turbulent kinetic energy k and its dissipation rate ε. There are many different versions available developed to improve the original model for specific and general applications. Parallel to these versions there are several methods to resolve the turbulent behaviour in the near-wall region where the model is assumed to be invalid by using one or two layer wall functions or no wall function at all. The use of wall functions takes away the need for high resolution boundary layer cells and saves computational time and memory.

In this thesis work the realizable $k-\varepsilon$ turbulence model with a two-layer shear driven wall-treatment and a second order upwind convection term were used. This model is more reliable than the standard $k-\varepsilon$ for many applications, especially in regions close to stagnation points, due to its realizability of the normal stresses [5]. It is known to predict swirling flows and the spreading rate of jet streams more accurately, which is important when modeling spray nozzles.

The transport of turbulent kinetic energy is formulated as

$$\frac{\partial k}{\partial t} + \overline{u_j}\frac{\partial k}{\partial x_j} = \nu_t\left[\left(\frac{\partial u_i}{\partial x_j} + \frac{\partial u_j}{\partial x_i}\right)\frac{\partial u_i}{\partial x_j}\right] - \varepsilon + \frac{\partial}{\partial x_j}\left[\left(\nu + \frac{\nu_t}{\sigma_k}\right)\frac{\partial k}{\partial x_j}\right]$$

where the first term is the local change of k in time, the second term represents the change due to convection, the third term is production of k due to velocity gradient of the mean flow and the last two terms represents dissipation and diffusion of k.

The realizable model introduces a new transport equation for the turbulent dissipation rate ε. This is formulated as

$$\frac{\partial \varepsilon}{\partial t} + \overline{u_j}\frac{\partial \varepsilon}{\partial x_j} = \frac{\partial}{\partial x_j}\left[\left(\nu + \frac{\nu_t}{\sigma_\varepsilon}\right)\frac{\partial \varepsilon}{\partial x_j}\right] + C_{\varepsilon 1}s_\varepsilon - C_{\varepsilon 2}\frac{\varepsilon}{k + \sqrt{\nu\varepsilon}}$$

where the terms represents local rate of change of dissipation followed by convection, diffusion production and dissipation. The kinematic eddy viscosity ν_t is defined as

$$\nu_t = C_\mu \frac{k^2}{\varepsilon}$$

where the important model parameter C_μ is expressed as a function of the mean flow and turbulence properties rather than assuming it to be constant as in the standard model. The expression is formulated as

$$c_\mu = \frac{1}{A_0 + A_s U^* \frac{k}{\varepsilon}}$$

The two-layer wall treatment is a computationally efficient and relatively precise method where the flow closest to the wall is divided into two layers. In the first layer the ε and μ_t profiles are specified based on wall distance. The specified ε profile is blended smoothly with the result from solving of the transport equation further away from the wall. The transport equation for k is solved in the entire flow field [5].

2.2.2 $k-\omega$ SST

The $k-\omega$ is a two-equation turbulence model similar to the $k-\varepsilon$ in which transport equations are solved for the turbulent kinetic energy k and and a specific dissipation rate ω, defined as the dissipation rate per unit turbulent kinetic energy $\omega = \varepsilon/k$. This model was used to investigate the spray sensitivity to choice of turbulence model.

The advantages of the $k-\omega$ model compared to $k-\varepsilon$ are better prediction of boundary layers under negative pressure gradients and that the model can be applied to the entire flow field without the use of wall functions. A disadvantage is that the boundary layer prediction is very sensitive to the ω of the mean flow, making the model extremely sensitive to inlet boundary conditions, especially for internal flows. This problem was solved by blending it with a standard $k-\varepsilon$ model far from the wall. In this way the advantageous features of both models can be used. The mixing is done by increasing the significance of an additional cross divisional term further away from the wall according to some specified blending function. The result is that the $k-\varepsilon$ model is used in the fully turbulent region far from the wall while the $k-\omega$ model is used to model the boundary layer close to the wall.

A model commonly used in the aerospace industry that utilises this blending is the Shear-Stress Transport or SST $k-\omega$ turbulence model which also includes a modification to the linear constitutive relation as $\mu_t = \rho k T$ [5]. This results in a transport equation for k given as

$$\frac{\partial(\rho k)}{\partial t} + \frac{\partial(\rho U_j k)}{\partial x_j} = \frac{\partial}{\partial x_j}\left[\left(\mu + \frac{\mu_t}{\sigma_k}\right)\frac{\partial k}{\partial x_j}\right] + P_k - \beta^* \rho k \omega$$

The terms on the left hand side represent the rate of change of k and the transport of k by convection. The right side terms are diffusive transport of k, production and dissipation. In a similar way the transport equation for ω is

$$\frac{\partial(\rho\omega)}{\partial t} + \frac{\partial(\rho\omega U_j)}{\partial x_j} = \frac{\partial}{\partial x_j}\left[\left(\mu + \frac{\mu_t}{\sigma_{\omega,1}}\right)\frac{\partial \omega}{\partial x_j}\right] + \gamma_2\left(2\rho S_{ij}S_{ij} - \frac{2}{3}\rho\omega\frac{\partial U_i}{x_j}\delta_{ij}\right) - \beta_2\rho\omega^2 + 2\frac{\rho}{\sigma_{\omega,2}\omega}\frac{\partial k}{\partial x_j}\frac{\partial \omega}{\partial x_j}$$

Where the terms represent the same phenomena but with one additional term. The last term is a cross-divisional source term due to the transformation of $\varepsilon = k\omega$ in the diffusion term of the ε transport equation [48].

2.3 Computational fluid dynamics

CFD can be used to study the small scale phenomena like the interaction between a single droplet and a liquid wall film or the atomisation and breakup of the continuum exiting a spray nozzle as well as large scale phenomena such as wind around skyscrapers and water flow in rivers and dams.

When performing simulations using CFD, a volume domain is generally created from the given geometry. The domain is then divided into a discrete cells to form a mesh. The Navier-Stokes equations, or in most cases the RANS equations, are discretised using a discretisation scheme such as finite difference, finite volume or finite element. The finite volume method is used in STAR-CCM+ and most other commercial CFD codes. This scheme converts the volume integrals of the partial differential equations governing the flow into surface integrals for each computational cell using the divergence theorem. The surface integrals are evaluated as fluid fluxes and since the flux into a fluid volume equals the flux out of the volume, the scheme is said to be conservative. When the boundary conditions are set up the solver iteratively attempts to find a better and better solution to the system of equations using a solver algorithm such as the SIMPLE algorithm used in STAR-CCM+ [5]. The flow field is finally post-processed to visualise and output useful results.

2.3.1 Pressure-velocity coupling

Uncoupled CFD solvers computes each velocity component and the pressure field from the flow equations without respect to the others. The fields are then corrected to fulfill the continuity equation and the new field are predicted using the SIMPLE algorithm. This is commonly known as segregated approach. It gives relatively fast convergence but is unsuitable for compressible flows.

A coupled solver simultaneously solves the momentum and continuity equations and is generally robust even for cases with dominant source terms such as buoyancy and rotation, or compressible flows with shocks. The convergence rate is mesh independent and the solution time scales linearly with mesh size.

2.3.2 Modeling of time in fluid dynamic simulations

Time can in general be modeled using a steady or unsteady approach. Steady simulations are used to find a steady state solution where the time is not advancing, making time steps irrelevant. Using a steady solver for an unsteady problem is equivalent to running an unsteady simulation with an extremely inaccurate time-step. Steady simulations are specially accurate for low Reynolds number, single-phase flow. The resulting steady-state flow field can preferably be used as initial conditions for unsteady simulations. Spray droplets tracked as a dispersed phase can be modeled using a steady approach but this is in most cases no recommended. Unsteadiness in the problem generally results in limited convergence or even divergence of the solution.

Unsteady simulations can be run either implicitly or explicitly to find a transient solution to the fluid flow problem. Some problems, especially involving physics such as time varying boundary conditions, vortex shedding, morphing or sliding mesh, free fluid surfaces or transient heat transfer obviously require transient simulations. In explicit simulations the current time-step is calculated by time integration of the last step and does hence not depend on any unknown variables from the current step. An implicit simulation on the other hand does depend on unknown variables and for this reason requires the system of equations to be solved simultaneously.

3 Numerical Modeling of Multiphase Flow

In a multi-component fluid such as air composed primarily of nitrogen, oxygen and hydrogen the components or chemical species are mixed at a molecular level. The micro scale mixing enables modeling of the mixture behaviour using a single phase with modified properties. The assumption is valid for mixtures with similar molecular weights of major constituents, similar momentum connected to the species diffusion, similar convection velocity and normal temperatures, for which dissociation and condensation of the species is insignificant. Single phase flow can hence be either single component, such as a flow of water or hydrogen in a pipe, or multicomponent such as the flow of air around a car or the flow of emulsions like milk or oil-water.

The species of a multiphase flow is mixed at a macroscopic level and the phases have different convection velocities. A fluid phase generally refers to the thermodynamic state, solid, liquid or vapor, of the matter. When modeling, the term phase is widened to define a volume of matter with distinguishing properties that can be tracked within the system. This implies that a phase could also be referred to as liquids or gases of different density, droplets of different size or solid particles of different shapes. A phase can hence be defined as the solid, liquid or vapor state of the matter rather than its molecular components and signified by an interface separating the states.

There are two different types of multiphase flows, dispersed flows and stratified flows, such as free surface flows and annular film flow in pipes. Similar to single phase flow, multiphase flow can be either single or multi-component. Steam-water and gas-liquid refrigerants flows are single component multiphase flows and typical examples of that these are in most cases flows containing a liquid and its vapor. A typical multicomponent flow with species mixed at a macroscopic level is liquid water and air with one of the phases dispersed in the other as droplets or bubbles. A phase is said to be continuous if it is possible to pass from one point in the fluid to any other without crossing a phase boundary, consequently a phase is dispersed if it is not materially connected to the rest of the phase, as for a droplet. There are four types of dispersed phase flows:

- Gas-liquid flows such as air bubbles in water, separated flows and water droplets in air
- Gas-solid flows with solid particles as the dispersed phase, involving industrial applications like pneumatic transport, fluidized beds and cyclone separators
- Liquid-solid flows such as hydro transport, sediment transport and slurry flows
- Three-phase flows such as combustion of droplets and solid particles in air inside a furnace

Liquid spray in air is a multi-component, multiphase flow of gas-liquid type weather the spray is single or multi-component in itself. Multiphase flows can be modeled using several different approaches depending on physics, application and the available computational resources. Spray simulation are generally performed using the Eulerian-Lagrangian approach and steady or unsteady RANS but can also be modeled on a macro scale using the Eulerian-Eulerian concept to save simulation time at the expense of accuracy and information loss. The Volume of Fluid method and direct numerical simulations have been used to develop and calibrate models used in the previously mentioned modeling approaches. Large eddy simulations and the Lattice-Boltzmann method is probably the future of spray and multiphase flow simulations. The remaining of this chapter will be used to describe the ideas behind and the common applications of these modeling techniques.

3.1 Eulerian-Lagrangian modeling

This project is based on the assumption that the liquid spray mixture of water and hydrogen peroxide and the gas mixture consisting of air and the vapor produced by the evaporation of the liquid components can be modeled using an Eulerian-Lagrangian framework. This means solving the continuity and Navier-Stokes equations for the continuous gas mixture and the Newtons second law of motion for the dispersed liquid droplets. The continuous and dispersed phases are coupled through source terms in the governing equations for momentum, mass and energy for the fluid.

$$\sum F_i = m_p \frac{du_i}{dt}$$

To estimate the forces acting on the droplets in Eulerian-Lagrangian simulations the continuum flow properties such as velocity, pressure and temperature are needed at the location of the particles. These properties are generally only known at the center of the computational cells, requiring a three dimensional interpolation method to estimate the value of the properties at the center of the parcels.

The STAR-CCM+ software distinguishes between Eulerian-Lagrangian modeling and Discrete Element Modeling (DEM) in a way that DEM is an extension in which individual particles rather than representative computational parcels are tracked. This methodology enables modeling of particles with individual shapes, not restricted to the spherical particle assumption, as well as the particle contacts that can be explicitly solved.

The advantages compared to Eulerian-Eulerian modeling techniques are more detailed information on discrete particle behaviour rather than continuum dynamics. The Lagrangian tracking makes it easier and cheaper to model a distribution of particle sizes or other properties of the dispersed phase which would have to be treated as separate phases using the Eulerian technique. It also enables the flexibility to control the physical forces acting on each particle. Advantages when comparing to DEM techniques are computational cost and generally a simpler model setup.

A general limitation of Eulerian-Lagrangian modeling is the expensive tracking of a large number of individual particles or parcels with advanced physics. It is generally also restricted to spherical particles and dilute flows with a volume fraction of the dispersed phase below about 10 %.

3.1.1 The concept of tracking computational parcels as source terms

For flow cases involving a relatively small number of particles each individual particle can be tracked by formulating and solving the equation of motion for the particle centroid. In a more general case, the number of particles is too large to be computationally efficient to model individually. The concept of tracking parcels is to track a group or cloud of individual particles, often 1-10000, instead of tracking each of them. This approach is used to save simulation time and cost. Parcels can be interpreted as a discretisation of the dispersed phase in a similar way as the cells are a discretisation of the continuous phase. The point source analogy means that the parcel is treated as a single point, with mass but without volume. This means that the volume fraction of the continuous phase always equals unity. The number of parcels and cells are not arbitrary, the number must be large enough to to capture the full dynamic characteristics of the fluid problem, something that is not easily quantified. Certainty often comes from comparing results from simulations performed with different number of computational parcels.

The concept of tracking parcels is only valid for volume fractions less than 10 %, without limit on mass fraction or loading. All particles within a parcel are assumed to be spherical and to have identical properties, i.e the same diameter, velocity, density and temperature. The parcel density is typically, but not always, assumed to equal the particle density, neglecting the existence of voids. Equation of motion for the parcel includes contact force with other parcels and the surrounding walls. Applying the concept of parcels makes it easy to model turbulent dispersion. Each parcel is modeled as a source term in the continuum governing equations of mass, momentum and energy, at the location of the parcel.

The point source approach has been proven successful for larger droplets and particles with a finite radius larger than the turbulent Kolmogorov scale of the continuous phase, resulting in relatively precise results and conquerable simulation times [39].

3.1.2 Coupling between the fluid phases

When running a one-way coupled multiphase Eulerian-Lagrangian simulation the continuous Eulerian phase influences the discrete Lagrangian phase through the drag and other forces in the momentum equation and droplet heat transfer in the energy equation, the continuous phase however is not influenced or fed back with information (source terms) from the dispersed phase. As a consequence of this the dispersed phase can be tracked as a part of the normal post-processing of the results from the continuum simulation. In the case of high speed, average size water droplets in air the coupling effect is too large to be neglected. However, in other multiphase applications, the one-way coupling may be a reasonably good assumption for dilute flows with small, low density particles or high carrier phase densities [8].

When using the two-way coupling each parcel is influenced by the continuous phase through the equation of motion, heat and mass transfer equations and considered as a point source in the governing equations for mass, momentum and energy for the continuum phase. The coupling enables modeling of evaporation and condensation of droplets. The disadvantage of using the two-way coupling is the increased simulation time since the phase equations need to be solved simultaneously [8].

3.1.3 Eulerian and Lagrangian time steps

The time step of the continuous fluid is dependent on the characteristic time scales of the flow field and the numerical methods used to find the solution. This time step is generally determined by the user during pre-processing. The time step connected to the Lagrangian phase and the numerical integration of Newton's second law of motion for each droplet, often referred to as the time step for particle-fluid interaction, is often determined individually for each droplet or representative parcel based on the particle response time. To avoid aliasing, a fraction of less than half of the particle response time must be used, this leads to a maximum time step for particle-fluid interaction in the order of magnitude of 10^{-7} s for a small water droplet and 10^{-2} s for a large droplet. The time step must however be smaller than the time step chosen for the continuous fluid simulation for accurate particle tracking to be possible. The collisional time step is a characteristic time describing the frequency of particle-particle interactions [5].

3.1.4 Methods for distribution of computational load to cluster CPUs

Load balancing is a software feature which distributes the calculation work from the fluid dynamic solver to the available computational resources, also called cores or CPUs. The new version 8 of STAR-CCM+ (2013) provides a dynamic load balancing feature for Lagrangian simulations. In previous versions, the domain decomposition is completely controlled by the domain representing the Eulerian phase. The partitioning solver dividing the computational load between the available CPUs by approximately distributing the equal the number of cells to each core based on cell topology. This partitioning method has shown to give good performance for single phase simulations.

For Eulerian-Lagrangian simulations of multiphase flow the accumulated CPU time is often dominated by solving the particle physics. In special cases, where the distribution of the dispersed phase is relatively homogeneous, the above described approach may still give satisfying performance. In cases where the distribution of particles is concentrated to only a part of the domain, as is often the case in spray simulations, the lack of particles in one cell region causes the assigned CPU to finish the iteration on a fraction of the the time it takes for another CPU to solve the cell region with a concentration of particles. This causes a CPU load imbalance which reduces the parallel efficiency, average CPU load and overall performance of the solver. Consequently, a domain decomposition based completely on the continuous phase is far from optimal.

A Lagrangian load-balancing solver was implemented in the software to overcome the CPU load imbalance induced by not taking the computational load of the Lagrangian phase into account during domain decomposition. The load-balancing solver collects information about the CPU load required to solve the Lagrangian physics in each Eulerian cell with respect to the current particle distribution. This information is provided to the partitioning solver as one of the requests generated by physics solvers and mesh topology changes. The partitioning solver dynamically executes the load balancing and distributes the combined load to the available CPUs. Individual tests have shown a decrease in accumulated CPU time of about 25-30 % when using this feature.

3.2 Eulerian-Eulerian modeling

The behaviour of a dispersed phase consisting of droplets, bubbles or particles is sometimes modeled and approximated as a continuum with modified properties. The term Eulerian-Eulerian indicates that both the dispersed phase and the surrounding fluid are modeled as continuous Eulerian phases, unlike the a Lagrangian phase which is modeled and tracked as a discrete phase governed by the equation of motion of each particle or droplet. This approach, also known as the two-fluid approach or multi-field modeling, can be used to model

sprays and other dense flows by assuming the cloud of droplets to behave like a continuum, with interfaces to the surrounding phase. Mass, momentum and energy exchange between the phases can still be modeled through source terms at the location of the shared interface.

The particulate phase is averaged to obtain probability density functions and mean properties, or fluid properties needed to solve the Navier-Stokes equations for the dispersed phase in the same way as the surrounding fluid. The droplet mass per volume, also referred to as the bulk density is used as the density of the continuous phase representing the droplet cloud. The average droplet velocity in an averaging volume is used as the velocity of the phase. The fluid viscosity of the droplet phase is more complex to predict and several methods have been used, generally observed and correlated from experimental data or related to the eddy viscosity of the carrier phase. The consequence is that a droplet size distribution need to be divided and modeled as one phase for each size, or approximated by a single droplet diameter. Separate phases increase the set of equations that need to be solved and increases the computational cost [8].

The granular kinetic theory excludes some of the empiricism by introducing the granular temperature, a measurement of the kinetic energy of the dispersed phase oscillations [11]. The granular temperature can be used to estimate the stresses and transport coefficients of the dispersed phase. In STAR-CCM+ the change between the flow kinetic dominated granular flow model and the collision dominated frictional theory is made based on the level of packaging [5].

A disadvantage is that all droplets in the same phase are assumed to consist of identical, smooth and rigid spheres without rotation. Since the dispersed phase is modeled as a continuum, all detailed information about each droplet is lost. The Eulerian-Eulerian approach is unable to model long-duration contacts, only instantaneous collisions and introduces accuracy problems when modeling phase changes. Collisions and phase interactions are better resolved in Eulerian-Lagrangian simulations [48].

3.3 The Volume of Fluid method

Unlike the Eulerian-Eulerian modeling concept the Volume of Fluid method is a one-fluid approach. Several different techniques have been used in the past to predict the motion and behaviour of free boundaries and fluid phase interactions such as the surface interface between ocean waves and the air above the surface. A simple but powerful and efficient method for this purpose is the Volume of Fluid method, also known as VOF. This is a simple multiphase advection model that keeps track of the interface between the phases by tracking the distribution of each phase. This is done by solving the transport equation for the volume fraction of the phases in the domain where s_{α_i} is the source term for phase number i.

$$\frac{d}{dt}\int_V \alpha_i dV + \int_S \alpha_i (v - v_g) dA = \int_V s_{\alpha_i} dV$$

The fluid flow is computed by solving the Navier-Stokes equations in the same way as conventional CFD. The phases are assumed to share pressure, velocity and temperature fields which leads to that the same basic governing equations for momentum, mass and energy as for single phase flow can be solved using fluid properties of the mixture weighted by the volume fractions. The VOF technique can be used for modeling of phase changes such as ice cubes melting in water or boiling of water with steam bubbles forming at the hot bottom of the pot.

The VOF method has a tendency to smear out and create a diffuse interface closer to a region rather than a surface. A sharp interface is obtained by the use of a second order discretisation scheme and a high sharpening factor. Sharp interfaces are important in surface tension dominated flows such as sloshing of oil or diesel in a tank or filling of milk or carbonated beverages in bottles or cartons. Exaggerated sharpening may lead to unnatural alignment of the interface with the grid and non-physical results.

VOF simulations on single droplet level to study breakup, collisions, agglomeration vaporisation heating and acceleration phenomenon has been reviewed in [36]. The VOF methodology has been used in several studies and industrial cases to investigate the formation of droplets during primary atomisation of a liquid jet in nozzles simulations of primary atomisation [45].

Other innovative applications of the VOF methodology are injection molding of non-Newtonian, low density polyethylene [30].

3.4 Direct numerical simulations

Direct numerical simulations or DNS is a concept of resolving all scales of a flow field by using a grid size finer than the smallest turbulent Kolmogorov length scales at which energy dissipates, combined with a time step shorter than the shortest Kolmogorov time scales of the flow equivalent to the period of the fastest fluctuations. DNS provides a direct solution to the instantaneous continuity and Navier-Stokes equations [48] without the use of empirically closuring turbulence models. The equations for an incompressible turbulent flow gives three velocity components and a pressure field that is closed by the system of four equations. Performing a direct numerical simulation is very computationally expensive when put in relation to the more commonly used RANS or LES simulation methods and thereby not yet conveniently applicable to industrial applications [48].

For multiphase flows however, there is no DNS without empirically adapted models since the phase interactions need to be modelled using collision models, volume fraction field or interface tracking. DNS simulations of multiphase flow have been used to study the physics of individual droplets, develop and calibrate models for droplet drag models, atomisation, breakup and coalescence, models which are now used in commercial codes. The process of using direct numerical simulations of multiphase flow at a high level of detail for small control volumes to develop models and close system of equations for simulations at a lower level of detail is often referred to multiscale modeling. Multiscale modeling is a common approach used in engineering, mathematics, physics, meteorology and computer science. Multiscale modeling of multiphase flows also includes using Eulerian-Lagrangian simulations to provide information to Eulerian-Eulerian modeling.

3.5 Large eddy simulations

Large eddy simulations or LES is a concept of fluid dynamic modeling that utilizes the advantages of both RANS and DNS. The method filters the unsteady Navier-Stokes equations and the computational domain spatially, solves the closed system of equations and resolves the mean flow and large eddies using direct numerical simulation without empirical modeling. The effect of the small eddies with a turbulent length scale below a certain threshold are modeled using ordinary RANS turbulence modeling and included by the use of a sub-grid scale model [48].

The increase in available computational resources has made large eddy simulations more applicable to industrial applications and complex geometries during the last years. LES simulations have recently been used to model large scale turbulent dispersion of water droplets in clouds in the sky [44] and in important engineering applications such as spray combustion [49].

LES has the potential to give more realistic and precise results for spray simulations by taking the transient effect of the large scale eddies into account in a more sophisticated manner than transient RANS simulations. However, LES requires a finer spatial and temporal discretisation and is dependent on the performance of the subgrid turbulence model, making it more computationally expensive and to some extent Reynolds number limited.

3.6 Lattice Boltzmann method

Numerical simulations of fluid dynamics using the Lattice Boltzmann method of modeling is different from conventional CFD modeling in the sense that the governing equations describing the dynamics of the flow is formulated on a higher level of detail, the level of particles. This higher level of information is known as the meso scale, whereas conventional CFD acts on a macroscopic scale with the flow properties defined in terms of pressure, temperature and velocity. The meso modeling is based on the kinetic theory [20], probability functions of particle motion describing the brownian motion and kinetic energy of molecules. These form

the already discretized Lattice Boltzmann equations. The equations can be used to derive the Navier-Stokes differential equations for which a differencing scheme such as finite volume or finite differencing has to be applied [7].

The results of a fluid dynamic simulation based on the Lattice Boltzmann method are not in the form of pressures, temperatures, and velocities but these quantities can simply be derived and averaged from the given results.

The advantages of using Lattice Boltzmann simulations instead of conventional CFD methods are the linear convection term, the possibility for local and fully parallel simulation performance, faster geometry domain setup without mesh generation, fully realizable boundary conditions [52] turbulence modeling by a modified relaxation time, simpler models for complex physics such as multiphase flows and the absence of diverging solutions due to instabilities. The Lattice Boltzmann method is limited to low and medium Reynolds numbers. Software based on this method are today available as open-source, freeware and commercial codes. Some parts of Lattice Boltzmann modeling of fluid dynamics are still under considerations, more information is given by [40].

4 Modeling of Evaporating Aseptic Spray

Modeling droplet behaviour involves estimating the forces acting on it due to relevant physical phenomena such as gravity, drag pressure gradients. The droplet position and velocity vector is updated through multiple integration of Newtons second law of momentum for the droplet, formed by the resultant force and droplet mass. Complex modeling involves two-way coupling between the phases through the governing equations of mass, momentum and energy for the fluid. This enables modeling of multicomponent droplet atomisation, breakup and agglomeration, condensation, boiling and evaporation, droplet-droplet collisions and wall impingement, multiple chemical reactions and liquid film forming on wall surfaces. The relevant physics will be described in the order they intuitively occur. The droplet behaviour and affect of these phenomenon can be described and characterised by dimensionless numbers based on the properties of the continuous and dispersed phases as well as the flow. These dimensionless numbers are thoroughly described in Appendix A. The indices c and p indicates the continuous and particulate phase, index rel represents the slip velocity or relative velocity between the phases.

4.1 Atomisation

Atomisation is the process that converts the bulk liquid into a cloud of droplets with a wide diameter distribution, in other word it works as a primary breakup of the water mixture jet to form a spray. Different atomisation methods are used in different applications but the common goal is generally to produce small, evenly distributed droplets that evaporate quickly. Atomisation is utilised in carburetors, airbrushes, spray bottles and shower heads.

During the primary breakup, the liquid is forced through a small diameter orifice, driven by forces created through high pressure or high relative velocity between the liquid and the surrounding gas. The liquid jet is torn apart by high shear forces, overcoming the surface tension of the liquid. The surface tension of the liquid stabilises the jet as well as the droplets produced, it prevents breakup and leads to larger droplets. The increased viscosity damps the internal motion, reduces agitation and increases the average droplet size. The liquid density causes jet and droplets to resist acceleration and results in larger droplets and a quicker spray penetration [2].

Numerical simulations of atomisation or primary breakup of a continuous fluid to droplets in spray nozzles have been performed and investigated using VOF methods [10] and LES-VOF [17].

The reason behind the process of atomisation is to maximise the surface area of the interface between the continuous and dispersed phases since an increase in area directly increases the transport of heat and mass by evaporation of the liquid. This means that, through the atomisation process, the evaporation rate is increased by several orders of magnitude in comparison to the bulk material that is not disintegrated through atomisation [9].

The performance of the atomisation process depend on the nozzle geometry, flow properties and the viscosity, density and surface tension of the liquid. For a new nozzle geometry or mass flow, the atomisation process is generally unknown and complex to model. For this reason the droplet injection distribution is often assumed and based on experience. In this thesis the diameter distribution is based on experimental measurements of droplet size downstream of the nozzle.

4.2 Droplet injection and diameter distributions

A Lagrangian spray injector is generally specified by direction, velocity, spray angel, mass flow, number of parcels per second and the droplet properties: temperature, diameter distribution and mixture composition. The droplets are injected as a solid or hollow cone originating from a point, or in the normal direction of a surface.

The droplet size distribution injected in a nozzle is either mono-dispersed or poly-dispersed. Mono-dispersed droplet distributions with identical droplets are often used to isolate and study specific phenomena of the dispersed phase. Poly-dispersed distributions are generally closer to reality, often specified using a normal, log-normal, or Rosin-Rammler distribution [19]. The distribution can also be specified as a user defined probability density function or a cumulative density function table for mass, volume or number of droplets. The Rosin-Rammler distribution was developed to describe the volume distribution of particles as a function of diameter. In STAR-CCM+ the Rosin-Rammler distribution is extended to a generic cumulative Weibull size distribution depending on mass or volume and defined as

$$F(D) = 1 - exp\left(-\left(\frac{D}{D_{ref}}\right)^{q}\right)$$

in which the exponent q and the reference diameter are specified by the user together with the upper and lower diameter limit. This distribution is often used for numerical simulations of sprays in industrial applications.

Time randomized parcel injection within the time step can be used to improve the appearance of animations by avoiding groups of parcels to appear to travel forward together. This feature should however not affect the accuracy of the solution.

4.3 Volume fraction

Droplet injection from a single point or surface can result in high volume fractions of droplets. The volume fraction of a dispersed phase in a cell is defined as the fraction of the cell occupied by Lagrangian parcel volumes. One of the fundamental assumptions of Eulerian-Lagrangian modeling, the point source approach and the additive droplet forces is that the flow is dilute. The dilute flow assumption is reasonable for volume fractions up to 0.1. In a spray nozzle however, the volume fraction of droplets is assumed to be higher, making a limitation on the allowed volume fraction required. This is done by a limiting parameter in the two-way coupling solver. In this case the default limit of 0.25 was used. For higher volume fractions the motion of the dispersed phase is dominated by internal collisions rather than by the fluid motion of the surrounding phase. The flow around each droplet will be affected by drafting effects and flow around the neighbouring droplets, making the general force expressions inaccurate. The accuracy of heat and mass transfer is also affected by decreased inter-particle spacing.

To improve stability when the volume fraction of the Lagrangian phase is limited the continuous phase source terms are limited proportionally to the ratio between the maximum and the current volume fraction. The terms are split into explicit and implicit components to further enhance stability, especially for cases with strong phase coupling.

4.4 Secondary breakup

After initialisation of the droplets, the secondary breakup is modeled to predict the breakup of large drops into smaller droplets due to high destructive forces. The destructive forces are counteracted by the surface tension and viscosity trying to maintain the spherical shape and hold the droplet together. The stability of the droplets is described by the dimensionless Weber and Ohnesorge numbers. These are used to characterise the magnitude of the destructive forces and divide the breakup into breakup regimes. The goal of modeling the secondary droplet breakup is to predict whether breakup occurs and the droplet diameter distribution resulting from it.

The first regime represents initial breakup through vibrational waves causing droplets to split into two child droplets. This is called vibrational breakup and happens at $We \sim 12$. At slightly higher $We < 20$ the droplet forms a disc, the disc expands into a wake of low pressure behind it, traps air in the middle and turns into a shape similar to a bag. It then starts breaking up from behind, disintegrated by the shear and vibrational forces, often with an additional streamer in the center for $We < 50$. Stripping breakup, when the circumference of the droplet falls behind and liquid is sheared or stripped off from the volume and broken

down into small droplets generally occur at $We < 100$. This can continue until the whole initial droplet volume is stripped away. For $We > 100$ the breakup effect is catastrophic and the whole droplet explodes into microscopic droplets. In STAR-CCM+ there are three models available for secondary breakup modeling, TAB for vibrational, Reitz-Diwakar for bag and stripping breakup and KHRT for stripping and catastrophic.

4.4.1 Taylor Analogy Breakup

The TAB model [25] was developed for vibrational breakup at low We and defines breakup as the point when the distortion of the droplet due to drag deforms the droplet into a disc with twice the diameter of the droplet. This is calculated using the surface tension, viscosity and We of the droplet. The resulting diameter distribution is determined based on an energy balance, and [5] gives more detailed information about the model and its implementation in the software.

The velocity vector is given an additional lateral velocity proportional to the kinetic energy of the droplet oscillations prior to the breakup. This generally produces a spreading effect out of a nozzle that in some cases makes a conical injector unnecessary. The TAB model is preferably used for modeling breakup at low We but is known to give fairly accurate results with a tendency to underpredict droplet diameters, even outside its range of validity [4].

4.4.2 Reitz-Diwakar

The breakup model developed by Reitz and Diwakar [29] predicts breakup in the bag and stripping regimes. It is a relatively simple model that does not generate any child parcels but only changes the diameter of the droplets in the parcel, making it computationally inexpensive.

Bag breakup is predicted when the critical droplet We is reached, in STAR-CCM+ this is defined at $We = 12$. From this We a stable diameter D_s is computed and used as a reference. The characteristic time scale for bag breakup is calculated from the droplet diameter, density and surface tension and a model constant C_{b2} as

$$\tau_b = \frac{C_{b2} D_p}{4} \sqrt{\frac{\rho_p D_p}{\sigma_p}}$$

For stripping breakup, the stable diameter is computed from $We = max(C_{s1} Re_p^{0.5}, We_{crit})$, and the breakup time scale is defined as

$$\tau_b = \frac{C_{s2} D_2}{2|v_{rel}|} \sqrt{\frac{\rho_p}{\rho_c}}$$

where the default values for the coefficients in STAR-CCM+ are $C_s1 = 0.5$ and $C_s2 = 20$. If the conditions for both breakup regimes are fulfilled, the regime with the smallest breakup time scale is assumed to be dominating. The droplet diameter reduction rate is defined as

$$\frac{dD_p}{dt} = \frac{D_s - D_p}{\tau_b}$$

4.4.3 Kelvin-Helmholtz Rayleigh-Taylor

The Kelvin-Helmholtz Rayleigh-Taylor droplet breakup model [26] was developed to model breakup in the stripping and catastrophic regimes using a combination between the two theories. The breakup is predicted using a consideration of wave length and growth rate of the droplet instabilities, calculated from the We, Oh and droplet properties. Kelvin-Helmholtz instabilities occur due to a high relative velocity between the droplet and the surrounding continua that shears small child droplets off parent droplet while Rayleigh-Taylor oscillations take place due to droplet acceleration, representing the two breakup regimes or modes.

In the KH mode, the child droplets being stripped from the parent are accumulated and released into a new parcel when their total mass exceed a fraction of the mass of the parent, default 3 % in STAR-CCM+. The diameter of the droplets in the parent parcel is kept constant while the number of droplets in the parcel is reduced for mass conservation. The velocity vector is supplied with an additional velocity component normal representing the kinetic energy of the droplet oscillation of the parent prior to the event. This mode is available only when the condition for RT is not satisfied.

The catastrophic RT instabilities are assumed to be growing if the droplet diameter exceeds a predefined fraction of the wave length of the oscillations. If the duration time of growing critical instabilities is longer than the breakup time scale the parent parcel is shivered completely, producing one or more child parcels with a diameter based on the wave length of the oscillations, default 10 % of the wave length.

The wave length and growth rate of the droplet instabilities are used to formulate the characteristic breakup time and length scales that are used to reduce the parent droplet size in a similar sense as the Reitz-Diwakar breakup model.

The objective behind the development of the KHRT breakup model was that it should replace the original and simpler TAB model due to its higher adjustability and possibility to predict breakup more precisely after some fine-tuning. The adjustability is at the same time a drawback since it requires significant calibration and fine tuning by the user, making default settings and coefficient values useless. For this reason the TAB model is still preferred for predicting breakup at low We.

4.5 Equation of motion and forces on droplets

Commonly modeled forces for the dispersed phase are the drag force, gravitational force, virtual mass force, pressure gradient, buoyancy, history force and various lift forces. The forces are assumed to be decoupled and additive. The forces are used in the equation of motion

$$\sum F_i = m_p \frac{du_i}{dt}$$

for the dispersed phase, solved individually for each droplet or parcel to stepwise update its position. The momentum transfer between the phases is added as a source term in the momentum equation for the continuous phase.

The drag force is the force acting on a single droplet or parcel due to the relative velocity between the droplet and the continuous surrounding fluid in a uniform pressure field without relative acceleration. It is generally the most important force when the motion is not totally dominated by gravity or buoyancy. It is defined as

$$F_D = \frac{1}{2} C_D \rho_c A_p |v_{rel}| v_{rel}$$

Where A_p is the projected droplet area in the direction of the relative velocity and C_D is the drag coefficient, see Figure 4.5.1. The drag coefficient used to calculate the drag force of a droplet is often defined using the Schiller-Neumann correlation [32]. The correlation is suitable for spherical particles, liquid droplets and small-diameter bubbles and is defined as

$$C_D = \frac{24}{Re_p} \left(1 + 0.15 Re_p^{0.687}\right)$$

for $Re_p \leq 10^3$ and $C_D = 0.44$ for $Re_p > 10^3$. The drag curve for a sphere is shown in Figure 4.5.1.

Extensions of the Schiller-Neumann drag coefficient model generally uses a dynamic drag coefficient accounting for droplet distortion due to aerodynamic forces. The droplet distortion increases the overall drag force by shaping the spherical droplet into something in between a sphere and circular disk with higher drag coefficient. In the Lui dynamic drag coefficient model [21], the relative increase in C_D for a disk compared to a sphere at high Re_p is assumed to be the same for all Re_p. Intermediate shapes are interpolated between the sphere and

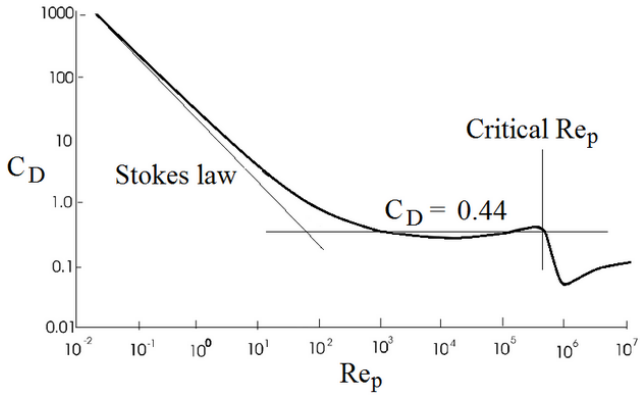

Figure 4.5.1: *Standard drag curve for a sphere*

the disk using the TAB distortion and the radial displacement normalised by the droplet diameter to form the expression

$$C_D = C_{D,sphere}(1 + 2.632y)$$

where the TAB distortion y is 0 for a sphere and 1 for a disk and

$$C_{D,sphere} = \frac{24}{Re_p}\left(1 + \frac{1}{6}Re_p^{2/3}\right)$$

for $Re_p \leq 10^3$ and $C_{D,sphere} = 0.424$ for $Re_p > 10^3$ [25].

The gravitational force is defined as $F_g = m_p g$, where g is the gravitational vector. Other body forces such as the electromagnetic coulomb force or thermophoretic forces can generally be specified as a user-defined body force by a product between the droplet volume and a field function describing the force field.

The buoyancy force $F_b = -m_p g \frac{\rho_c}{\rho_p}$ is another volume force that represents the floating effect due to the Archimedeś principle stating that any object, entirely or partially immersed in a fluid is buoyed up by a force equal to the weight of the fluid displaced by the object. This makes the force significant for low density particles in high density fluids, such as air bubbles in water, but not for water droplets in air. Due to the order of magnitude of density difference the influence of this force was neglected in this work [51].

The pressure gradient force is defined as $F_p = -V_p \nabla p_{static}$. It is important for wake regions and bubbly flows with high relative continuum density. In this case the density ratio between the surrounding air and the liquid droplets is in the order of magnitude of 10^{-3}, making the effect of the pressure gradient force negligible, however it was still included due to the insignificant computational effort needed to compute it [5].

The virtual or added-mass force corresponds to the apparent increase in droplet mass due to acceleration of the surrounding fluid when the relative velocity vector of the droplet changes. This force is significant when the relative velocity changes quickly or when the density of the fluid is large in relation to the density of the droplet. It is defined as

$$F_{vm} = c_{vm} m_p \frac{\rho_c}{\rho_p}\left(\frac{Du_c}{Dt} - \frac{dv_p}{dt}\right)$$

where c_{vm} is a coefficient describing the added mass in relation to the original droplet mass. A value of 0.5 is often used for spherical particles. Since the density of air is three orders of magnitude lower than the density of the liquid droplets, this force can be neglected. It was however included due to the reason that it may add robustness and increase convergence by decreasing the flow sensitivity to relaxation factors for momentum and pressure [5].

In the same way as the virtual mass force accounts for the form drag forces due to droplet acceleration the history force takes the viscous effects into consideration by the temporal delay in boundary layer development around the droplet. These two unsteady effects are both derived for Stokes flow but are not well established for high Re_p. Due to an accumulating integral in the force expression the history force is a computationally expensive force that is not available in STAR-CCM+ [8].

Lift forces are significant for non-spherical and rotating particles. The standard lift force follows the same formula as the drag force but with C_L as coefficient, generally with a numerical value much lower than the drag coefficient. For particles with rotation, originating from collisions, wall interaction or velocity gradients, a normal lift force will affect the trajectory in the same way as a spinning football curves. This is often referred to as the Magnus lift force. Lift forces can also appear in velocity gradients normal to the droplet velocity vector. In these cases the pressure on the side of the droplet with higher velocity will be lower than the pressure on the low velocity side according to the Bernoulli's equation. This force is significant in boundary layers where the velocity gradient normal to the general flow direction is large, especially for large particles and high density and high viscosity surrounding fluids [8]. Modeling of lift forces are not available in this kind of simulations in STAR-CCM+.

4.6 Droplet collisions and coalescence

The influence of collisions on the simulation results are significant for flows with dense dispersed phases and high loading. In general, taking the effect of droplet-droplet interaction into account leads to a significantly wider droplet diameter distribution with a majority of very small droplets and a small fraction of droplets with larger diameters than the initial.

The interaction between droplets by collisions and coalescence or agglomeration, when droplets collide, stick together and form larger diameter droplets is modeled using a collision model. The NTC [33] and the O´Rourke [24] collision models are used in STAR-CCM+ to detect and predict the outcome of interactions between droplets. The host cell approach is used to search for potential droplet collision partners meaning that two parcels can only collide if they are positioned in the same computational cell. In each cell, the least expensive of the two algorithms is used.

In the NCT, No Time Counter collision detection model the number of expected collisions in each cell during a specific time period is assumed to be the sum of the probabilities of all possible collisions. For each identified collisional parcel couple a randomly distributed number between zero and one is generated to determine the probability of a collision to occur. For droplet dense cells with a high collisional density the O´Rourke algorithm is more computationally efficient than the NCT approach by considering all droplet parcel collision couples possible in the cell and computing the collisions directly. The switch between the two models is made automatically in each cell.

The outcome of the collision is characterised based on three dimensionless numbers, the collision Weber number describing the instability of the droplets, the impact parameter describing the collision angle and the ratio between the larger and the smaller droplet diameters. The full dynamics of the algorithm and the probability of the different outcomes are described in [18] but the general idea behind the model is that high relative droplet velocities (high collisional Weber number) give separation and splash, high surface tension low velocities lead to low instabilities and bounce while large droplets and high collision angles results in coalescence. The resulting velocity, temperature and mass of the droplets are computed from the conservation of mass, momentum and energy.

4.7 Turbulent dispersion

Turbulent dispersion of droplets occur due to transient effects in the carrier phase. There is no turbulent dispersion by the mean flow. Models for turbulent dispersion are needed to account for local variations in the flow field. A large number of simulations is needed to get statistically significant results from the different realizations. Prediction of particle motion in a turbulent flow field is problematic since there are few detailed and accurate models for turbulence, even in single-phase flow. The effects of turbulence on particle motion is significant for all but large, heavy particles that are unaffected by turbulent velocity fluctuations. For particles small enough to follow the instantaneous fluid motion, the particle dispersion is equal to the fluid element dispersion. Particles that do not follow the flow due to their inertia interacts with several eddies which reduces the particle residence time in each eddy and reduces the influence of the eddy on the particle trajectory. DNS

can be used to solve the fluid turbulence and particle dispersion without empirical closure models by resolving even the smallest, Kolmogorov length scale from the Navier-Stokes equations.

STAR-CCM+ uses a turbulent dispersion model based on work done by Gosman and Ioannides [12], similar to the discrete random walk model. A droplet is assumed to flow through eddies as it moves in the flow field. The droplet is affected by a random velocity component taken from normal distribution with zero mean value and standard deviation given by the eddy velocity scale $U_e = \sqrt{2k/3}$ during the entire lifetime or time-scale of the eddy defined as

$$\tau_e = \frac{2\mu_t}{\rho u_e^2}$$

or until the distance between the droplet and the eddy exceeds the length scale of the eddy due to a non-zero relative velocity. The eddy length and timescales are extracted from the turbulence model.

The selection of a velocity through a random number is called the Monte-Carlo method. Since a random number is used to model the dispersion several simulations needs to be done to get different realisations which can be average over to get statistically significant final results.

4.8 Droplet evaporation

The physics of evaporation allows each component of the droplet to change state individually into its vapor at the interface, vapor which is added as a source to the governing equation of mass for the continuous phase. The change of state is driven by departure from the equilibrium point of the liquid -vapor system, or in other words, by the difference in concentration of the droplet vapor between the surrounding fluid and the droplet surface. The fluid flow is assumed to consist of a binary mixture between the carrying gas and the droplet vapor. In this case the hot air is considered as a single species mixed with hydrogen peroxide and water, both in their vapor state. The multicomponent droplets are assumed to consist of a homogeneous ideal mixture of liquid components. The quasi-steady evaporation rate for each evaporating droplet component is written as

$$\dot{m}_{evap} = -g^* \varepsilon A_s ln(1 + B)$$

where g^* is the mass transfer conductance based on the diameter and slip velocity of the droplet, ε is the fractional evaporation rate of the component, A_s is the droplet surface area and B is the Spalding transfer number based on the thermodynamic properties. The transfer number and conductance are expressed and computed differently, depending on what phenomena is limiting the evaporation rate. The physical process of evaporation can be split into three separate modes. Supercritical evaporation occur when the droplet temperature exceeds the highest critical temperature for the droplet constituents. This results in instant evaporation.

Heat transfer limited evaporation is limited by already saturated vapor at sub-critical temperature surrounding the circumference of the droplet surface. Since evaporation is driven by the concentration difference the limit is when the vapor concentration in the gas around the droplet is the same as the concentration at the droplet surface. The mass transfer conductance is based on the Nusselt number and the transfer number is based on the latent heat of vaporisation and temperature of the droplet.

Vapor diffusion limited evaporation occur when the droplet evaporation rate is not limited by any of the aforementioned criterion. In this case it is limited by the maximum evaporation rate at which the vapor can diffuse from the droplet surface. The conductance parameter is based on the Sherwood number and the molecular diffusivity of the vapor. The molecular diffusivity of the vapor determines the pace at which the evaporated vapor is transported away from the high concentration region near the droplet surface. The transfer number is based on the surface equilibrium mass fraction [37].

In this case the Sherwood number is determined based on the Ranz-Marshall correlation as $Sh_p = 2(1 + 0.3Re_p^{0.5}Sc^{0.33})$, where Sc is the dimensionless Schmidt number [28]. The minimum allowed mass before the droplet is assumed to evaporate instantly was set to a default value of 10^{-24} kg. The limitation enhances computational stability and helps avoid that simulation time is spent on small, insignificant droplets.

Another, simpler method for predicting and modeling droplet evaporation is to use the D^2-law stating that the square of the droplet diameter decays linearly with time as

$$D^2 = D^2_{initial} - \lambda t$$

where λ is an evaporation constant specific for the case. The time needed to evaporate the droplet completely is found by setting $D = 0$, which gives

$$\tau_{evap} = \frac{D^2_{initial}}{\lambda}$$

This method is suitable for approximations and concept design of evaporator units [8].

4.9 Wall impingement

The interaction between droplets and walls can be modeled using the Bai-Gosman [3] or the Satoh [31] wall impingement model in STAR-CCM+. Since the Satoh model is specially developed for oil droplets in oil-mist separators, it is unsuitable for this study. The Bai-Gosman model was developed for diesel and gasoline sprays in the automotive industry, to predict whether spray droplets impinging on hot cylinder walls will break up or stick to the wall and form a thin layer of fluid film.

The Bai-Gosman model characterises the possibles outcomes of a collision between a droplet and a wall into six different modes of wall impingement, as illustrated by Figure 4.9.1. The characterisation is based on the incident We, established from the wall normal component of the droplet velocity, the Laplace number La, the wall temperature and the wall state. The wall state of a boundary can be defined as wet or dry. Wall faces modeled as fluid film boundaries are assumed to be wet if the fluid film thickness on the face is greater than zero.

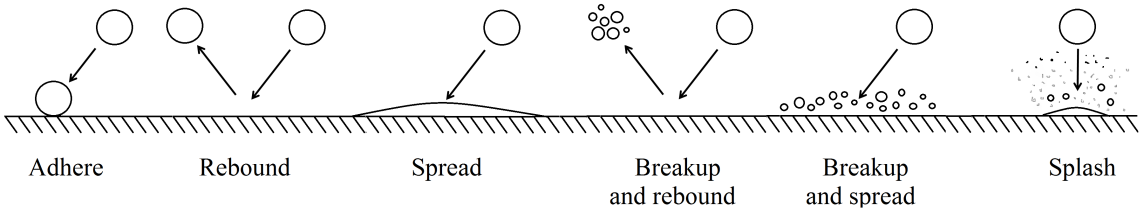

Figure 4.9.1: *Bai-Gosman impingement outcomes*

In the adhere mode the droplet sticks to the wet wall boundary. The mode does not exist for dry walls. If the wall is modeled as a fluid film boundary, the droplet transfers its mass, momentum and kinetic energy to the film. Stick occurs at very low incident velocities and low wall surface temperatures, typically for small droplets with high surface tension and low density.

During the rebound mode the droplet bounces instantaneously on the wall with a tangential coefficient of restitution of $e_t = 5/7$ and a polynomial incident angle dependent normal coefficient of restitution. Rebound typically takes place at medium wall temperatures and slightly higher velocities.

Medium to high incident We leads to the spread mode, where the droplet merges with the existing film on a wet boundary. This is implemented as a rebound with zero as the normal coefficient of restitution. If the wall is modeled as a fluid film boundary the droplet transfers its mass, momentum and kinetic energy to the film at the impact location. The lower limiting We is defined as $We_{spread} = ALa^{-0.18}$, where A is a splash onset parameter with a default value of 1320.

The breakup and rebound/spread modes occur at medium incident We and medium to high wall temperatures. For the first of the two modes, the impinging droplet shatters and rebounds from the wall. In the second, boiling induced breakup shatter and spread the droplet along the wall surface. No remainder of the initial droplet is left on the wall in these modes.

Highly unstable droplets with high incident We result in splash for any wall temperature, creating one or several child parcels with small droplet diameters selected from a Rosin-Rammler distribution. For the first temperature range, see Figure 4.9.1, a fraction of the droplet is left and merged with the wet wall or fluid

film while at higher temperature no residue of the droplet is left due to the Leidenfrost effect. The remainder of the child droplets are randomly reflected from the wall as a cone injector with velocities computed from conservation of energy. The possible outcomes, depending on We and wall temperature, of impinging droplets on wet and dry walls are illustrated in Figure 4.9.2.

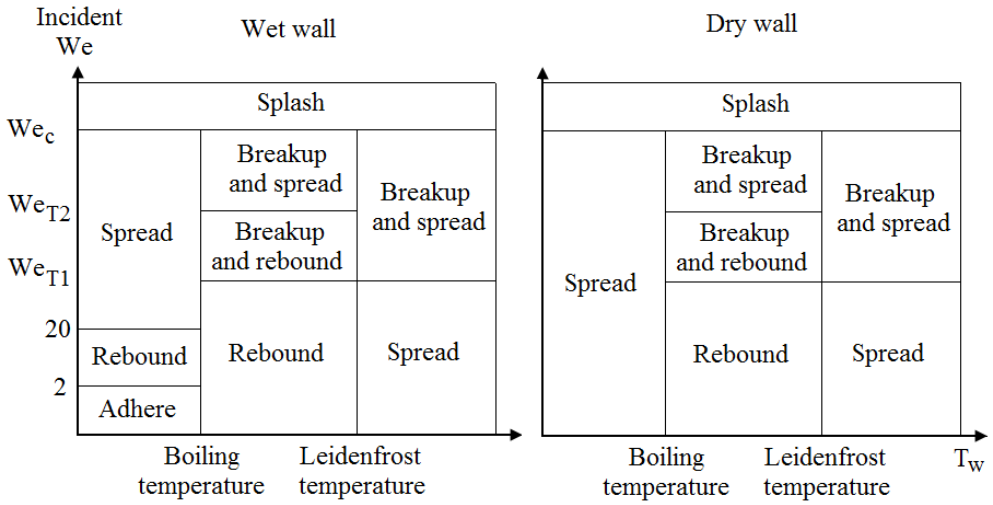

Figure 4.9.2: *Bai-Gosman impingement regimes for wet and dry walls*

The limiting We between the modes are material specific. The first critical temperature T_{12}, separating the temperature ranges one and two is assumed to be the boiling temperature of the droplet. The second critical temperature T_{23} is assumed to equal the Leidenfrost temperature of the droplet.

Leidenfrost temperature represents the temperature for which a liquid droplet starts hovering around above the surface on a bed of vapor, this phenomenon result in a lower heat transfer and evaporation rate of the droplet than for a slightly lower wall temperature due to the isolating effect of the vapor bed [16]. This can easily be studied by letting water droplets skid around in a hot frying pan, they will evaporate at a lower rate than whey would at a lower temperature.

4.10 Fluid film on solid walls

A thin layer of liquid film on solid walls is common in many engineering applications such as spray painting and surface cooling, ink-jet printers, bearing and lubrication systems and on the internal surfaces of a combustion engine. A fluid film can be used to model gravity driven flow on vertical walls, the effect of shear forces on wall film, waves and vibrations, evaporative cooling of a wall surface as well as interactions with Lagrangian phases through impinging and stripping droplets.

The dynamic characteristics of a fluid film is modeled using a two-dimensional shell mesh based on the boundary faces of the volume mesh on which the film is predicted to form. The transport of film is modeled using conservation equations for mass, momentum, energy and film species according to [5]. The velocity and temperature profiles are assumed along the thickness of the film and using boundary layer approximations. The film is assumed to be thin enough for laminar flow to be a valid assumption.

Fluid film can form on a wall boundary in several different ways. It can be defined as an initial film thickness with temperature, velocity and species composition. It can also come from a boundary defined as a fluid film inlet or from a fluid film mass source. It can form from the interaction between the Eulerian or Lagrangian and the film phase through condensing gas or droplet impingement. Phase changes such as melting and solidification of the film can also be modeled, this is useful when studying icing and deicing on automotive windscreens. The film volume is defined as the area times the film thickness of the cell.

Evaporation and condensation of fluid film is defined for film temperatures below the lowest boiling temperature of the film species. Individual mass and energy conservation for the components are used to compute the mass and energy flux. The evaporation rates of the film components are used to formulate and calculate the source

terms in the governing equations of mass, momentum and energy between the film and the surrounding fluid [5].

For temperatures above the lowest boiling temperature of the film species, liquid film boiling is modeled instead of evaporation. There are usually two types of film boiling to be considered, bulk boiling and wall boiling. The same conservation equations as for film evaporation are used for both cases but the mass flow of vapor from the film is calculated differently. For bulk boiling the the temperature of the composite film is assumed to equal the temperature of the mixture according to the rule of mixtures, vapor bubbles forming inside the film are assumed to remain at the saturation temperature and all the heat flux from the film is assumed to arise due to evaporation. The mass flow is then computed based on the latent heat of vaporisation, the heat transfer coefficient between the bubbles and the surrounding fluid and the difference between the instantaneous temperature and the saturation temperature of the fluid film [5]. Wall boiling occurs when the film boiling temperature is exceeded by the solid wall temperature. The heat flux from the hot wall to the film is proportional to the cube of the temperature difference between the two but does not reach higher than the critical heat flux of the film [50]. When the critical heat flux is reached, the heat flux decreases again, down to the the Leidenfrost temperature where it stabilises at a much lower rate. It is possible for a high temperature spray impinging a wall and producing a liquid film on the surface to cool the wall to a temperature below the spray temperature. This is caused by the vaporization of fluid film draining energy from its surroundings, the adjacent wall and fluid, generating a heat transfer from the wall and fluid to the fluid film, thereby reducing the wall temperature. This effect is taken into account when modeling fluid film in STAR-CCM+.

Edge stripping of fluid film, when droplets leave the film volume, may occur when the film travels around a sharp corner. In STAR-CCM+ the resulting droplet diameter distribution is computed according to [22] using a method based on the Rayleight-Taylor instability, analogue to the TAB model for secondary breakup of droplets. The film breakup into droplets is computed from a film based Weber number and a film Reynolds number [1]. The edge stripping droplets are injected into the region at the same direction and with the same velocity as the film. Film stripping can also occur due to adjacent fluid flow , gravity or film acceleration generating waves that induce instabilities in the film and shedds droplets. Modeling of fluid film generally demands even shorter time steps than the recommended droplet motion of maximum 3-4 cells for each time step [5].

4.11 Behaviour of individual droplets

Understanding of the behaviour of individual droplets is important in order to be able to improve the accuracy of numerical spray modeling. The absence of a solid outer surface when modeling liquid droplets in comparison to solid particles introduces some additional dynamic features. The internal fluid is affected by the relative droplet velocity generating internal circulation backwards, along the surface. The fluid in the central parts of the droplet flows in the opposite direction. The internal droplet circulation reduces the droplet drag force. The internal circulation is however sensitive to surface contaminants that causes the liquid surface to behave as a solid boundary, ruining the internal circulation and increasing the drag force. Furthermore droplets may collide and merge (also known as coalescence or agglomeration), deform, break up, evaporate, condensate and impinge on walls to cause splashing, sticking or the creation of fluid film. Deformation and stability of a droplet is dependant on the droplet density, diameter, surface tension and relative velocity [8]. Droplet deformation and stability is described using the dimensionless droplet Weber number. Droplet deformation and its effect on drag was investigated by [14].

4.12 Brownian motion

Very small particles or droplets will be in velocity equilibrium with the carrier phase flow at the location of the droplet. However there can still be a diffusion due to Brownian motion. The phenomena of Brownian motion is the random effect described as the influence of individual high-velocity molecules in the carrying fluid on the particle or droplet being tracked [8]. Even though the Brownian droplet is being constantly bombarded by approximately 10^{21} molecules/s from all directions, there will always be an imbalance between molecules hitting one side in comparison to the other, causing an instantaneous resultant force to be applied towards the

side with fewer collisions [6]. The concept of modeling Brownian motion is a simple stochastic process related to the normal distribution motivated by its mathematical simplicity and convenience rather its accuracy. The effect of Brownian motion is smaller for a dispersed phase suspended in liquid than in a gas due to the higher velocity of the gas molecules. The influence of Brownian motion is only significant for sub-micron particles or droplets and can often be neglected due to the extensive mass difference[8], so also in the present work.

5 Methodology

Two case studies were used to study parameter sensitivity in a small and controlled environment with short simulation times in order to widen the knowledge and apply the results to the full geometry. In the first case a free spray in a quadratic box was used to study general spray behaviour and solver settings. The second case was a channel with a cross flow and a spray that was used to study wall impingement and fluid film characteristics. This chapter will be used to describe the methodology and setup of the case studies as well as the numerical and experimental methodologies for the Tetra Pak A6 evaporator.

5.1 Hardware and software

The pre-processor ANSA from BETA CAE Systems was used for CAD-cleanup, geometry simplifications and for creating closed volumes out of which the boundary surfaces were exported. Pre-processing, simulation and post-processing was performed using the STAR-CCM+ version 8.02 software package and solver developed and supported by CD-adapco. Netbeans IDE 7.3 and Java Development Kit was used for scripting and writing macros to STAR-CCM+, for a consistent and quick case setup sequence. The numerical simulations were carried out using an external computational cluster at Gridcore Gompute, Gothenburg, Sweden. Lighter simulations were run on a local workstation and on the FS Dynamics cluster. The programming environment and software package Matlab from Mathworks was used for analysis and result visualisation.

5.2 Physics and modeling technique

The surrounding gas (including the air assistance in the case with the Tetra Pak evaporator) was modeled using a continuum approach in the Eulerian frame of reference. Ideal gas was assumed. The continuum fluid flow was assumed first solved using steady state RANS, after convergence the results were used as initial conditions and boundary conditions for the unsteady RANS simulation used with the Eulerian-Lagrangian tracking of spray droplets. All simulations included gravitational effects for all phases. The $k - \varepsilon$ realizable turbulence model with a two-layer all y^+ treatment was used in all cases where no other turbulence model is mentioned in the case description. In the cases where solid-fluid conjugated (coupled) heat transfer was modeled, the steady state RANS equations were solved.

The droplets in the spray were modeled as a non reacting dispersed Lagrangian phase with discrete computational parcels representing a cluster of individual droplets in the spray. The forces acting on each parcel was integrated in time to update its velocity vector and spatial position. Each parcel was considered as a point source in the governing equations for mass, momentum and energy for the continuum phase and was consequently not seen to occupy any volume. To model the feedback information a two-way coupling for inter-phase transfer of mass, momentum and energy between the phases was used.

Primary atomisation was assumed to occur prior to the spray injector and was for this reason not considered. For the Tetra Pak A6 evaporator, with high We number, secondary droplet breakup was modeled using the Reitz-Diwakar breakup model and for the spray box and wall impingement case studies the TAB breakup model was used, when nothing else is specified in case description.

The drag force, the gravitationally induced force, the virtual mass (added mass) force and the pressure gradient force were included in the equation of motion for each parcel in the Lagrangian phase. The particle Reynolds number dependent Schiller-Neumann drag coefficient correlation was used in all spray simulations. Even though all droplets are assumed to be small and spherical the Lui dynamic drag coefficient was used to account for the droplet distortion due to aerodynamic forces. Turbulent dispersion was modeled, whereas Brownian motion was not considered.

Droplet evaporation and Eulerian-Lagrangian energy transfer was modeled using the Sherwood number and the Ranz-Marshall method, with a minimum mass limit of 10^{-25} kg. The density and specific heat of each

droplet was varied as a polynomial of the temperature, see Appendix D. The saturation pressure was modeled according to the Antoine equation [27], see Appendix D.

The Bai-Gosman wall impingement model was used to model the interaction between droplets and solid walls. The results were presented with and modeling of fluid film and droplet collisions. Fluid film related convergence problems was solved by specifying a narrower specific heat polynomial range for the liquid droplets to avoid the enthalpy from exceeding the gas enthalpy, leading to a negative latent heat of vaporisation at extreme temperatures. Specifying a higher than expected maximum temperature for the Antoine equation used to compute the droplet saturation pressure and limiting the minimum and maximum allowed temperatures for the continuum and the fluid film also helped to avoid problems with non-monotonically increasing saturation pressures and divergence.

5.3 Spray box

The aim of running simulations on a small and simplified geometry was to perform a parameter sensitivity analysis for a general spray case as well as finding a methodology of best practice, a good enough compromise between reasonable computational cost and sufficient accuracy. Such an analysis would be impractical to run the Tetra Pak A6 evaporator due to the required simulation time. Typical parameters such as time step, mesh size, mesh type and number of inner iterations and sub steps were investigated. The focus however, was laid on parameters and settings with potential to save a significant amount of time while maintaining simulation accuracy. The case study was used to investigate the influence of different models, options and settings with the objective of finding a balance between accuracy and computational cost as well as investigating the general behaviour of a spray. Measurements such as spray penetration length, spray width and total evaporated droplet mass were compared. The input data for the case study was based on the Tetra Pak evaporator setup where possible.

The geometry consists of a simple cubical fluid region with side length 100 mm. The spray injection point was located in the middle of the top face, two cells from the wall, pointing in the direction of the gravity vector. The meshes were refined around and downstream of the the injection point. The standard mesh is shown in Figure 5.3.1. The continuum was initialized as stationary air with a static temperature of 290 °C, the same temperature as the heated air in the Tetra Pak A6 evaporator, but with no inlet or outlet.

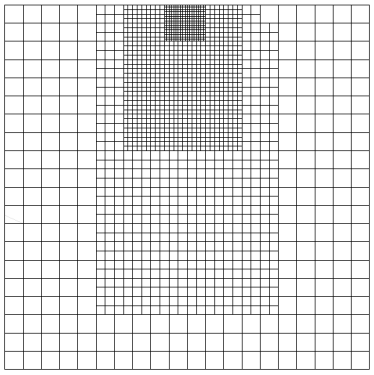

Figure 5.3.1: *Standard mesh used for the spray box case study*

In the standard case the spray was specified as a single point, full cone spray injector with 35° outer cone angle and a poly-dispersed Rosin-Rammler diameter distribution of droplets between 1-100 μm, with a mean diameter of 10 μm. Mono-dispersed droplet injection was used when the droplet diameter was varied. The droplets were injected with an ambient droplet temperature of 30 °C, mass flow of 2 g/s and species mass fraction of 35 wt% hydrogen peroxide and 65 wt% liquid water. One million parcels per second were injected. Important parameters, models and meshes were varied one at a time.

5.4 Channel flow with spray and wall interaction

The aim of this case study was to investigate the behaviour of droplet-wall interaction by studying wall impingement and formation of liquid wall film on the surface. The interaction is an important physical phenomena in the spray nozzle used in the evaporator of the Tetra Pak A6 since the spray interacts with a concave spherical cup 4 mm after the injection. The sensitivity of the liquid wall film to mesh size and boundary conditions was investigated by simulating the physical behaviour in a geometry and setup originating from [3], a study on the interaction between diesel spray in a channel flow.

After the first mesh sensitivity analysis of the fluid film the conclusion was made that a further parameter study on the film would be problematic because the deviation effect of the severely mesh dependent film would be more significant than the parameter studied.

The geometry consists of a 200 mm long channel with a 32x172 mm cross section. The spray injector was positioned in the middle of the top face, in the middle of the first cell, with an angle of 20 deg to the wall normal in the flow direction. The fluid region was in the standard case meshed with 2 mm, semi-structured, trimmed hexahedral cells, see Figure 5.4.1.

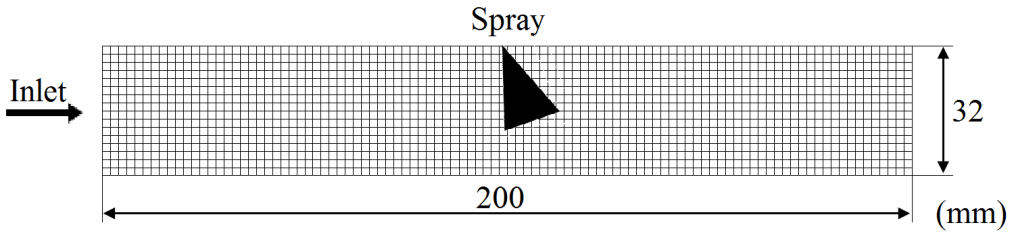

Figure 5.4.1: *Standard mesh used for the wall impingement case study*

An average cross flow velocity of 15 m/s and ambient temperature of 30 °C was used. The fields for velocity, pressure, static temperature, turbulent kinetic energy, turbulent dissipation rate and species mass fraction from a steady state RANS simulation was used as initial conditions for the unsteady spray simulations. A flow with fully developed boundary layer was produced by implementing a periodic interface boundary condition between the inlet and outlet boundaries of the fluid region. The resulting inlet velocity profile was used as a velocity inlet boundary condition.

In the standard case the spray was specified as a single point injector with 32 deg outer cone angle, a velocity of 20 m/s and a poly dispersed Rosin-Rammler diameter distribution of droplets between 1-100 μm, with an average diameter of 10 μm. Mono-dispersed droplet injection was used when the diameter was varied. A massflow pulse of 4.7 g/s during 0.07 s was injected at 1000 parcels/ms with a temperature of 30 °C. The simulations were run for 0.02 s. Droplet evaporation was not modeled. Simulations were performed with and without fluid film and collision modeling.

Fluid film thickness and the total mass fraction of the spray forming film on the wall were extracted and compared for different cases. The droplet diameter and velocity were sampled on the outlet boundary to investigate the post-collisional effect of modeling fluid film and collisions.

5.5 Tetra Pak A6 evaporator

The evaporator was modeled from the perforated plate, on which the nozzle head is mounted, to a plane 300 mm downstream of the nozzle. This part of the geometry was assumed to be sufficient, since the experimental measurements was performed by sampling droplet diameters and velocities on a plane 27 mm downstream of the tip of the nozzle.

A semi-structured mesh with trimmed hexahedral cells, refined in the high-gradient regions inside, around and downstream of the nozzle was used, see Figure 5.5.1. The average cell size inside the nozzle was 0.15 mm. The cup, on which the spray droplets impinge, was especially refined to capture the behaviour of the fluid film, to

a minimum cell size of 0.05 mm. Outside the nozzle the cell size gradually grew from 0.6 to 10 mm far away from the nozzle. Three prism mesh layers was used to resolve the boundary layer on the nozzle geometry and evaporator walls.

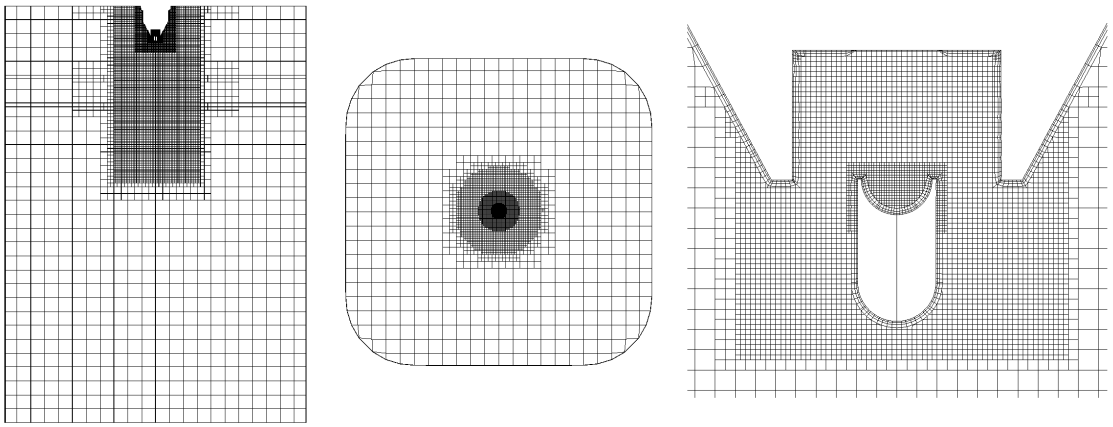

Figure 5.5.1: *Tetra Pak evaporator mesh: side, top and nozzle*

The top surface was modeled as a massflow inlet with an airflow of 80 kg/h and a temperature of 290 °C. The turbulence was specified using a turbulence intensity of 0.2 and a length scale of 0.2 mm, corresponding to the average hole size of the perforated plate designed to evenly distribute the flow over the cross section. Since the fluid film and the Bai-Gosman droplet-wall interaction model is highly wall temperature dependent the thermal boundary conditions on the nozzle head surfaces were thoroughly investigated using the conjugated solid-fluid heat transfer methodology described in Appendix C. The resulting temperature field was used as a thermal boundary condition on the nozzle head wall. The sidewall of the evaporator was modeled as an adiabatic slip wall.

The air-assistance of the spray was specified by the injection surface inside the nozzle. It was modeled as a velocity inlet with ambient temperature and a velocity of 250 m/s, corresponding to an airflow of 6.2 kg/h from the heater. The injection temperature of the spray droplets and the air-assistance was investigated using conjugated solid-fluid heat transfer, see Appendix B. The temperatures were set to 35 °C. The spray was injected from the same surface with a massflow of 5 kg/h, divided into 35 wt% H_2O_2 och 65 wt% H_2O. The droplet diameters were randomly sampled from a normal distribution with mean diameter 10 μm, standard deviation 4 μm and a range from 1 μm to 100 μm, based on the experimental data. The droplets were injected normal to the injection surface, with a velocity of 60 m/s. Approximately 1000 parcels/ms were injected based on the result from the spray box case study. Droplet collisions and fluid film were modeled in the cases where the opposite is not stated.

A single-phase, steady-state RANS simulation with only the hot airflow and the ambient air-assistance was run. The velocity, pressure, static temperature, turbulent kinetic energy, turbulent dissipation rate and species mass fraction fields from the steady simulation were then used as initial conditions for the unsteady spray simulations. The steady state velocity on the inlet boundary was used as velocity inlet boundary condition for the transient spray simulations. An Eulerian time step of 10^{-6} to 10^{-5} s, with 3-5 inner iterations, two-way coupling every time step and a maximum of 200-400 Lagrangian sub-steps was used, based on the results from case study of the spray box. The number of maximum sub-steps was continuously monitored and adjusted to result in approximately 1 % of the parcels reaching the maximum allowed number of steps.

In the case where only 1/4 of the geometry was modeled the symmetry planes were modeled with slip boundary condition and the tangential velocity at the planes were extrapolated from the adjacent cell using either the Hybrid Gauss-LSQ gradient or the Green-Gauss gradient method. The Hybrid Gauss-LSQ method uses a combination of the Gauss and weighted LSQ methods for all field variables while in the Green-Gauss gradient method the weighted least-squares method is used for the pressure and the simple Gauss method, originating from the Gauss divergence theorem, is used for all other variables. The heat flux through the symmetry plane is set to zero and the boundary temperature is extrapolated using the same reconstruction gradients method as the velocity. For the Lagrangian phase the boundary condition of the symmetry plane can be specified

as either escape, where the droplet and its mass, momentum and energy is removed from the computational domain, or reflect, making the droplet rebound perfectly elastic from the boundary face without losing any energy [5]. In this study the reflect condition was used.

The droplet diameter and vertical velocity of all parcels passing the measurement plane 27 mm downstream of the nozzle tip were sampled. The velocity and diameter profiles were averaged, plotted and compared to the experimental data. The Sauter mean diameter profile, standard deviation profiles for diameter and velocity were also investigated. Probability density functions and cumulative density functions for all droplet diameters and velocities sampled up to 14 mm from the centerline of the spray were also produced to compare the overall statistical diameter and velocity distributions. Temperature, velocity and H_2O_2 concentration field were also plotted to visualize the numerical results.

5.5.1 Improvement of thermal boundary conditions

The wall surface temperature of the nozzle head is of great significance for the behaviour of both fluid film and the Bai-Gosman wall interaction regimes. In previous simulations the nozzle head walls were modeled with adiabatic thermal boundary conditions and the spray outlet temperature was assumed to equal the temperature of 30 °C in the container of the liquid spray mixture and air compressor. This way the effect of heat transfer from the nozzle and the thin tubing, reaching through hot air 290 °C) from the evaporator wall to the nozzle head is not taken into account. The nozzle surface temperature and the spray injection temperature are investigated in Appendix B and C respectively.

5.6 Experimental measurement technique

The experiment was conducted at the Optigas evaporation rig at Tetra Pak in Lund. A full scale prototype of the Tetra Pak A6 filling and packaging machine was investigated. The STERIS Turbosonic nozzle #007 and evaporator geometry described in Section 1.5 was used. Inspection windows were installed on the evaporator walls for visual inspection and laser measurements. The hot evaporator was thermally insulated from the surrounding ambient air.

The experiment was conducted with an airflow from the heater through the evaporator of 80 kg/h at 290 °C. This gives an average vertical velocity of approximately 0.8 m/s over the cross section of the evaporator. The spray nozzle was provided with 6.2 kg/h of pressurised air and 5 kg/h of a liquid mixture of 65 wt% water and 35 wt% hydrogen peroxide, all at an ambient temperature of 30 °C, measured in the external liquid container.

Phase Doppler Interferometry [23] was used to measure the droplet diameter and vertical velocity on a 2D plane 27 mm downstream of the nozzle. Two dimensional laser scans of planes perpendicular to the flow direction were performed by traversing the measurement point, the intersection between the two laser beams, to for a grid with steps of 2 mm. The diameter and velocity were sampled for each droplet passing through the 0.1x0.1 mm area around the intersection point.

An average of 37850 droplets were sampled for each test point, with a minimum of 11100, maximum of 50000 and a standard deviation of 7250. Unrealistic data samples, such as high negative velocities due to non spherical shapes or droplets that only partially passed the measurement volume, were removed from the data before further post-processing. The experimental data was post-processed to visualise the average and Sauter mean diameters, velocity and standard deviation distributions across the width of the spray. Probability and cumulative density functions were produced for both diameter and velocity to visualise the statistical distributions. To get statistically significant results only the measurement points within a radius of 13 mm from the spray center were analysed. According to numerical simulations, this range covers 99.9 % of the droplet massflow, see Figure 6.3.10.

6 Results and Discussion

This chapter will be used to present the results from the case studies together with the results from the numerical and experimental analysis of the Tetra Pak A6 nozzle and evaporator.

6.1 Spray box

A study of spray parameters and a sensitivity analysis for solver and setup settings was performed. The general spray parameter study showed intuitive results, the water component of the droplets initially evaporated about ten times faster than the liquid hydrogen peroxide component. Higher injection velocity gave faster evaporation in time, but slower in distance, meaning that the rate was higher but at a fixed distance from the injection point, a lower mass fraction had been evaporated, see Figure 6.1.1. The figure shows the total evaporated droplet mass in the fluid region. Higher velocity of the heated surrounding gas gave similar results as higher spray velocity.

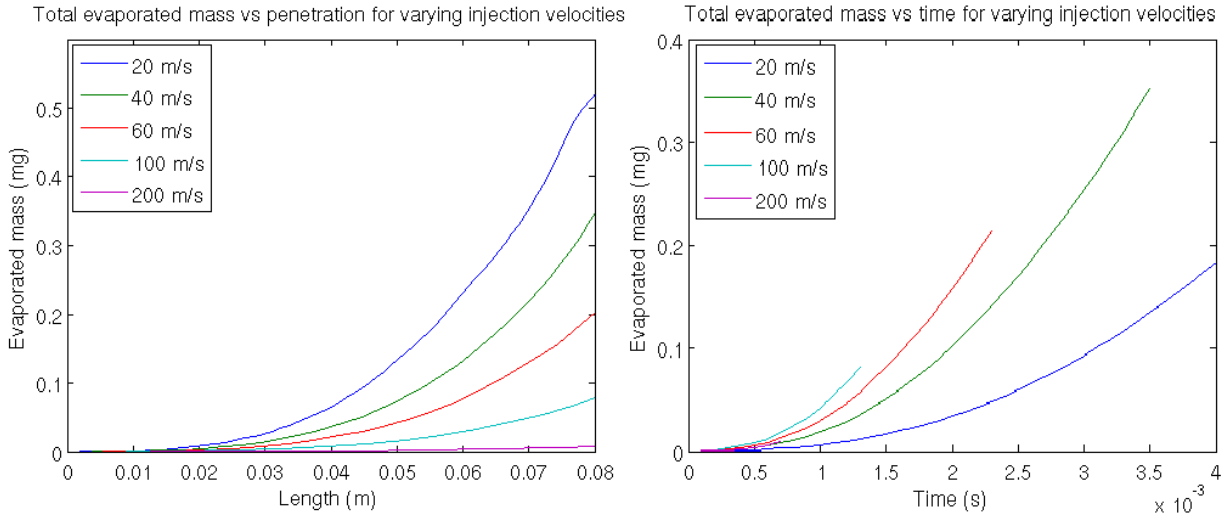

Figure 6.1.1: *Total evaporated droplet mass vs penetration length and time for varying injection velocities*

Increased outer cone angle for the spray resulted in a higher evaporation rate, and a higher mass fraction of evaporated droplets per penetration length, see Figure 6.1.2. Higher spray injection temperature and smaller droplet diameters both resulted increased droplet evaporation.

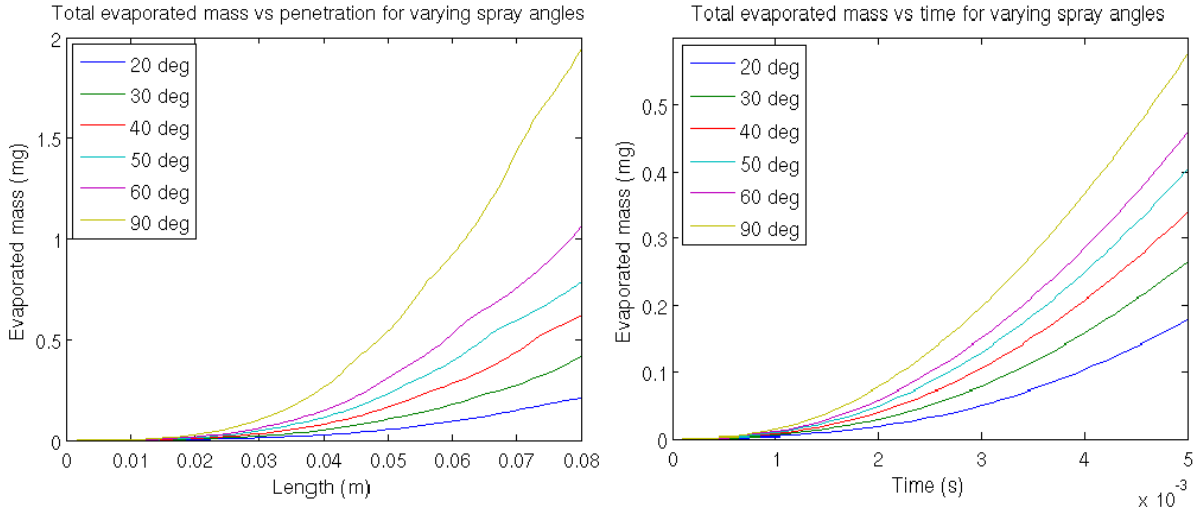

Figure 6.1.2: *Evaporation vs penetration length and time for varying spray angles*

6.1.1 Simulation time

Simulation time increased fairly linear with increasing number of time steps, solver iterations and Lagrangian substeps. Increasing the number of steps or iterations by a factor of two seemed to double the run time. Choice of turbulence model and modeling of droplet-droplet collisions did not have a significant impact on the solution time.

6.1.2 Cell type

The spray sensitivity to the type of computational cell was studied by comparing hexahedral, polyhedral and tetrahedral cells. Polyhedral and trimmed hexahedral cells resulted in grids with similar number of cells for a fixed base size, while the tetrahedral cell type produced a mesh with three times the number of cells. As can be seen in Figure 6.1.3 to 6.1.4 the polyhedral and hexahedral cells gave very similar spray results while the tetrahedral cells resulted in a slightly narrower spray with lower droplet evaporation rate. The figures show the spray penetration length, width and evaporated droplet mass plotted against elapsed time.

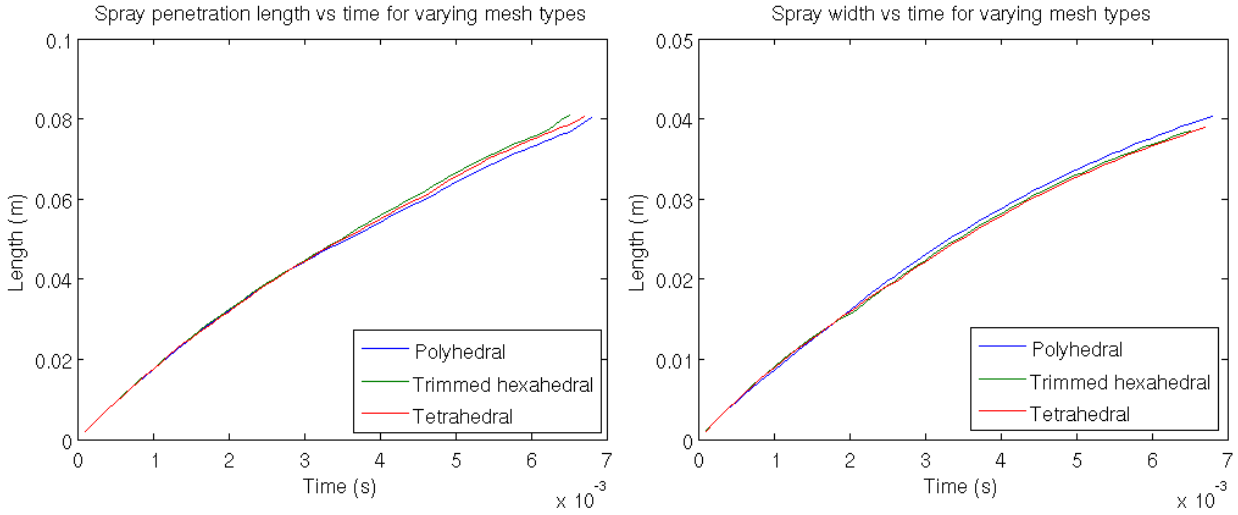

Figure 6.1.3: *Spray penetration and width for varying cell types*

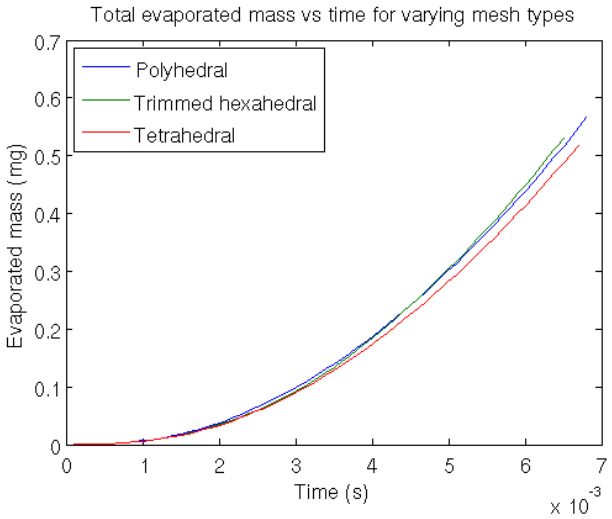

Figure 6.1.4: *Evaporation for varying cell types*

6.1.3 Cell size

The spray sensitivity to cell size was analysed by varying the side length of the quadratic hexahedral cells in a homogeneous computational domain from 0.5 to 8 mm. As can be seen in Figure 6.1.5 to 6.1.6 cell sizes from 0.5 to 4 mm gave similar spray behaviour while the 8 mm grid resulted in faster spray penetration and higher droplet evaporation rate.

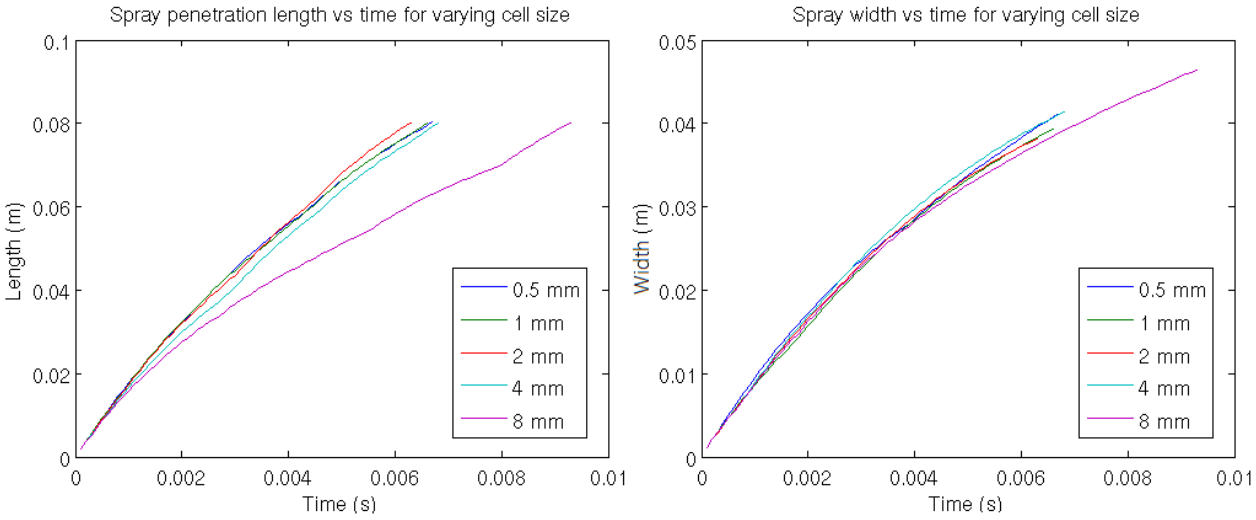

Figure 6.1.5: *Spray penetration and width for varying cell size*

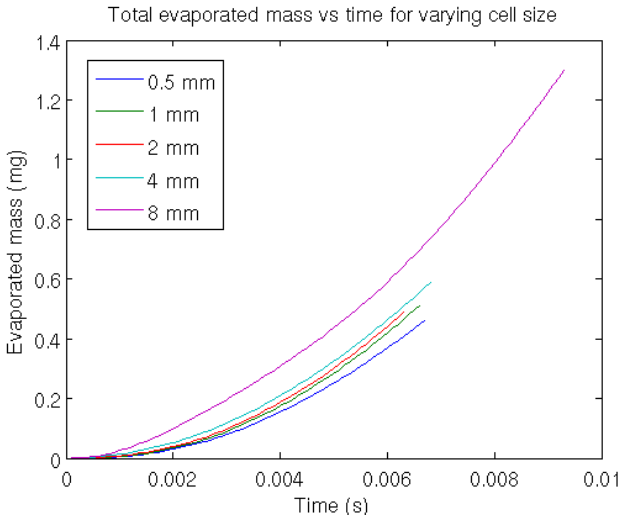

Figure 6.1.6: *Evaporation for varying cell size*

In Figure 6.1.6 it can also be concluded that the droplet evaporation rate decreases slightly with increased number of cells.

6.1.4 Turbulence model

The spray sensitivity to turbulence model was studied by comparing four different models, the standard and realizable $k-\varepsilon$ models and two $k-\omega$ models based on the Menter and Wilcox theories. As shown in Figure 6.1.7 to 6.1.8 the spray seem very independent of the choice of turbulence model in this simple test case.

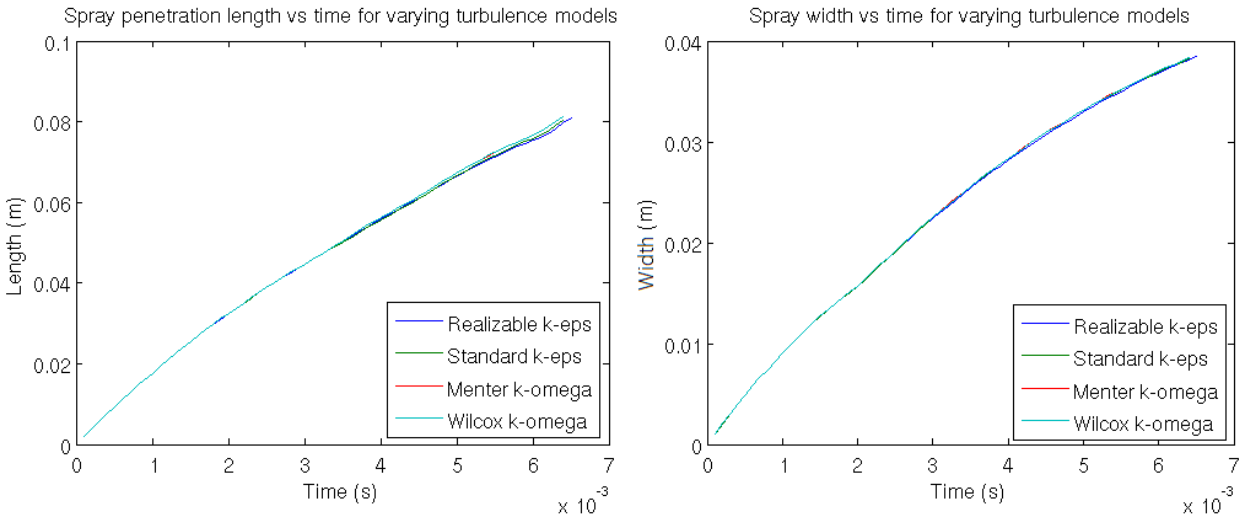

Figure 6.1.7: *Spray penetration and width for varying cell size*

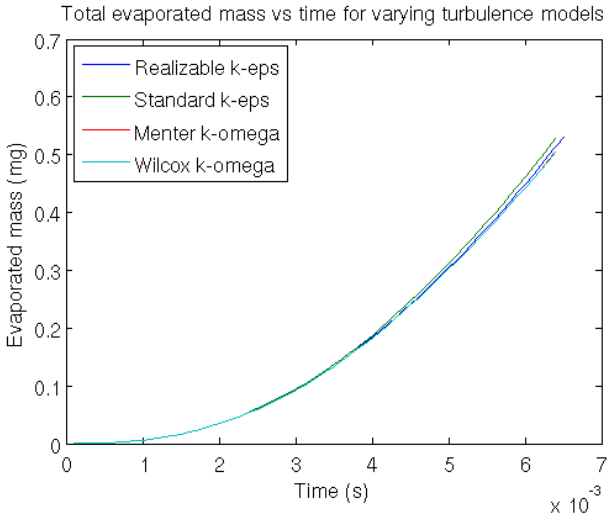

Figure 6.1.8: *Evaporation for varying turbulence model*

6.1.5 Time step

The time step determines the updating frequency for the Eulerian phase. The simulation time increased linearly with decreasing time step. As shown in Figure 6.1.9 the two medium time steps resulted in very similar dynamics of the spray while the longer and shorter time steps stands out in their respective directions. The trend shows increasing penetration velocity for increasing Eulerian time step.

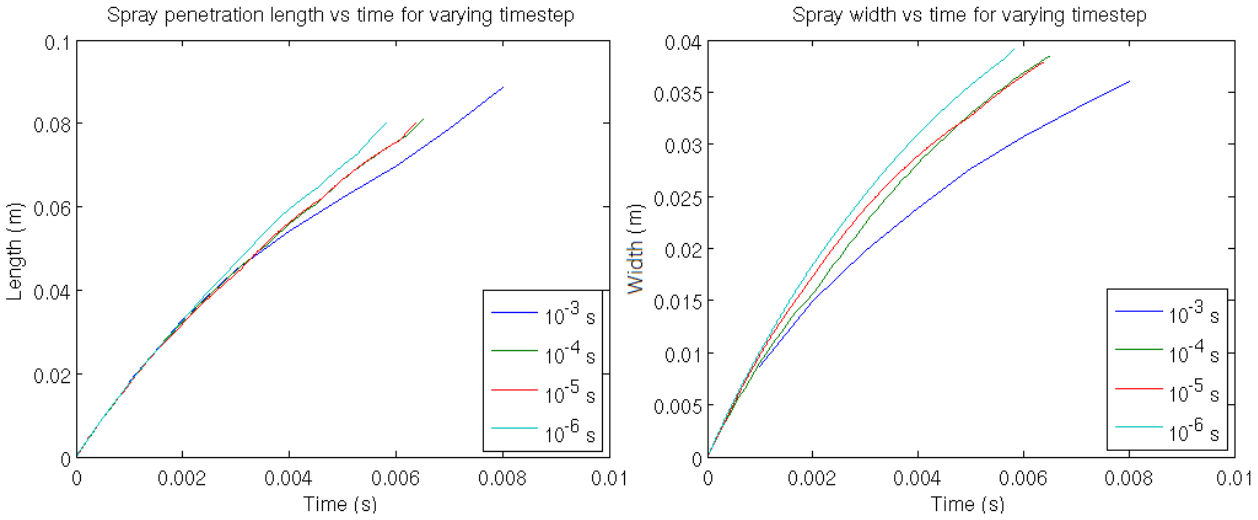

Figure 6.1.9: *Spray penetration and width for varying Eulerian time step*

In Figure 6.1.10 the two shortest time steps resulted in very similar thermal droplet behaviour while the evaporation rate decreased with coarser time steps.

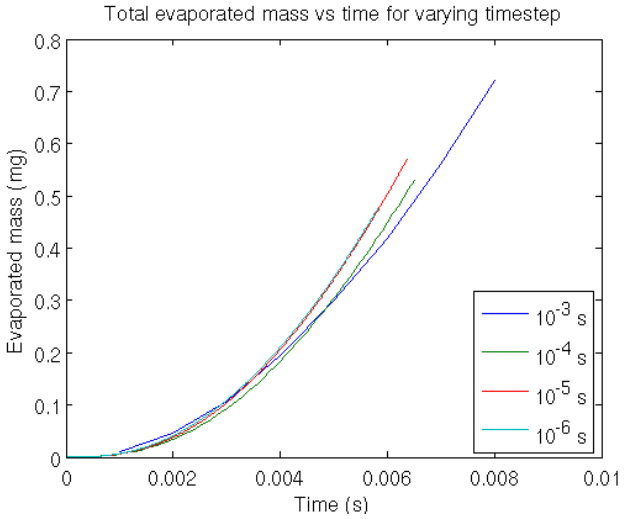

Figure 6.1.10: *Evaporation for varying Eulerian time step*

6.1.6 Inner iterations

The maximum number of inner iterations determines when to stop the inner iterations in the implicit Eulerian solver and march the solution forward to the next time step of the transient solution. Figure 6.1.11 shows very similar spray dynamics for inner iterations from 5-30 and decreasing penetration velocities for decreasing number of iteration.

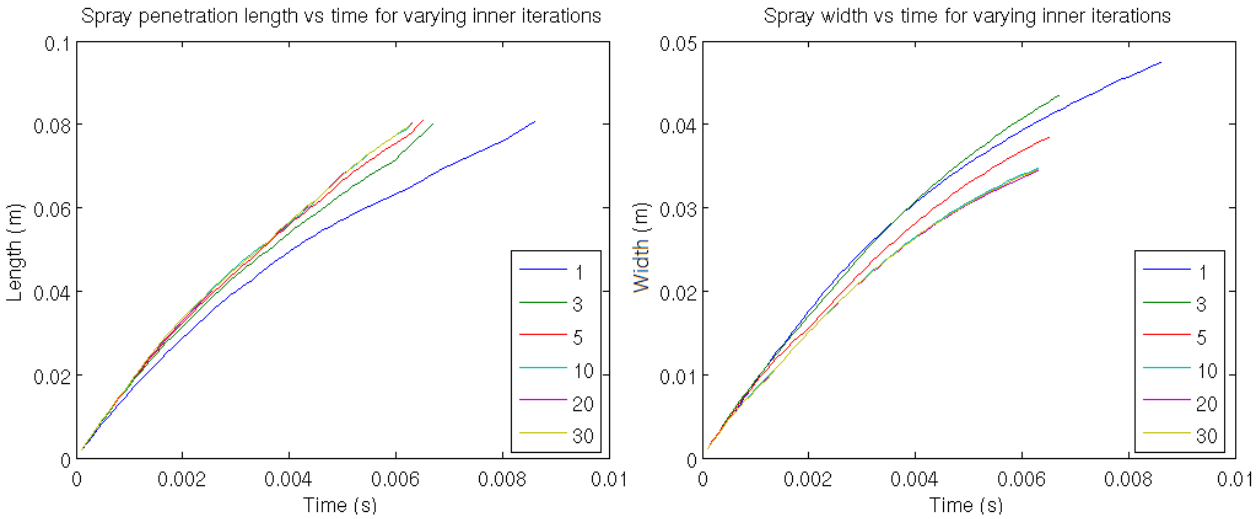

Figure 6.1.11: *Spray penetration and width for varying inner iterations*

Figure 6.1.12 shows similar droplet evaporation rates for inner iterations from 1-30

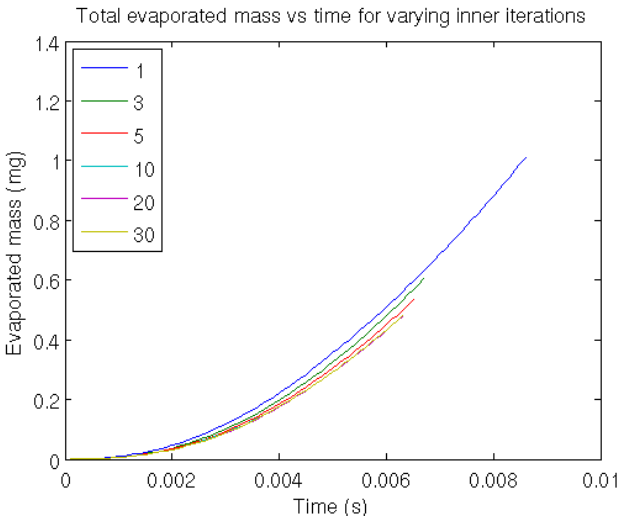

Figure 6.1.12: *Evaporation for varying inner iterations*

6.1.7 Lagrangian solver frequency

The Lagrangian solver used for implicit unsteady analyses can be run every Eulerian iteration or only after the first iteration of each Eulerian time step. Figure 6.1.14 and 6.1.14 show that running the solver only once per time step gives consistent results for time steps shorter than 10^{-5} s but highly inaccurate spray width and droplet evaporation rates for time steps longer than 10^{-4} s.

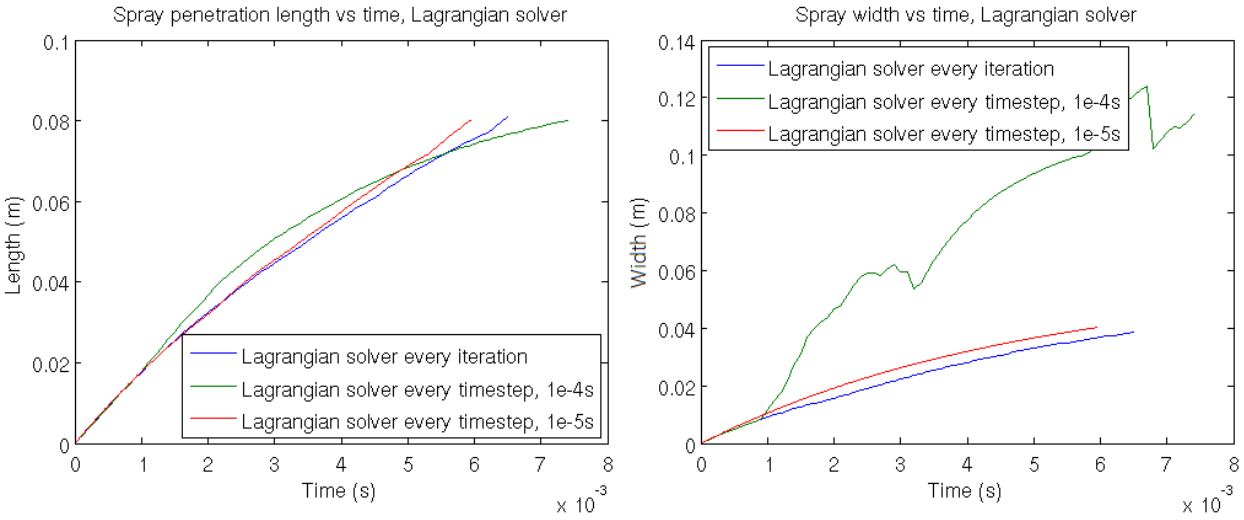

Figure 6.1.13: *Spray penetration and width for varying Eulerian and Lagrangian solver setting*

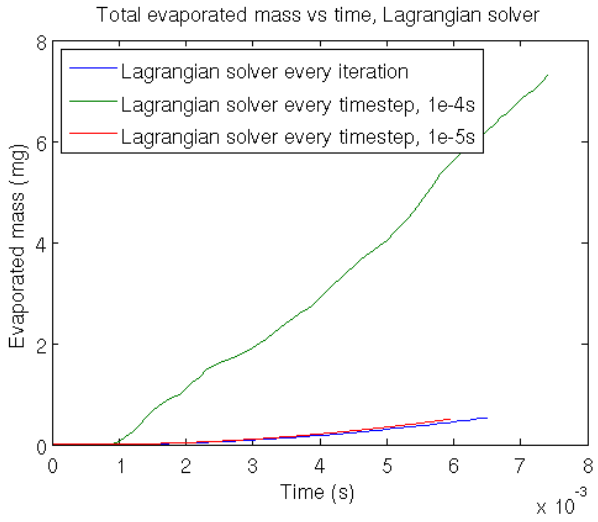

Figure 6.1.14: *Evaporation for varying Eulerian and Lagrangian solver setting*

6.1.8 Lagrangian substeps

The sensitivity to maximum specified number of substeps for which the parcels are tracked, to avoid problematic parcels from being tracked indefinitely, was evaluated based on the fraction of parcels reaching the maximum number of substeps. The trajectories of these problematic parcels were prematurely terminated for the current time step. As shown in Figure 6.1.15 the spray penetration velocity is very similar for up to 30 % of the droplets reaching the maximum number of Lagrangian sub-steps.

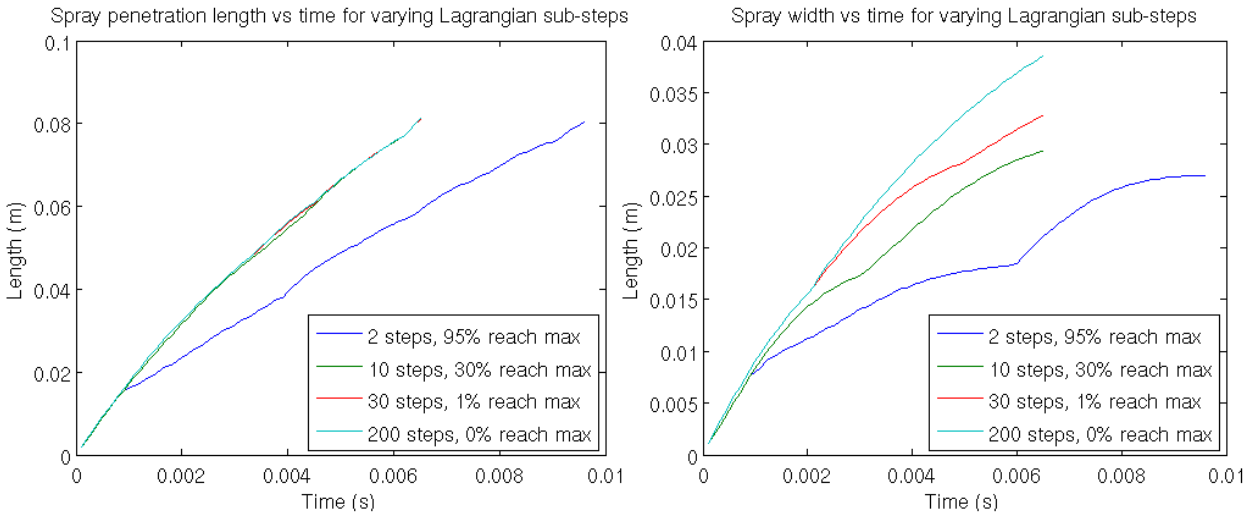

Figure 6.1.15: *Spray penetration and width for varying maximum number of Lagrangian substeps*

Figure 6.1.16 shows very similar droplet evaporation rates for 0-1 % of prematurely terminated droplet trajectories but highly under predicted evaporation rates for decreased number of substeps.

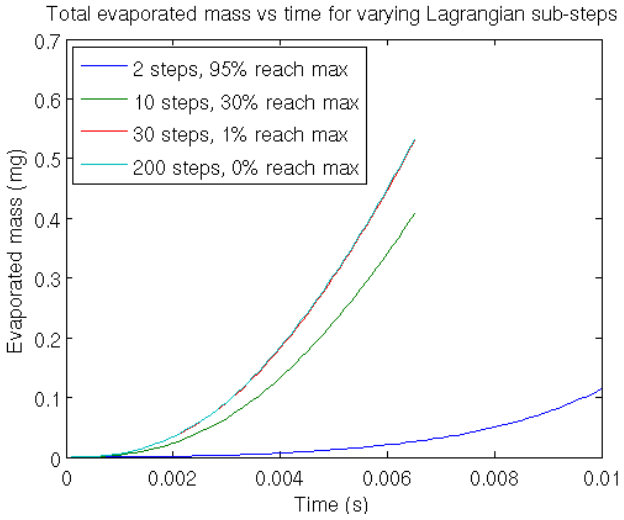

Figure 6.1.16: *Evaporation for varying maximum number of Lagrangian substeps*

6.1.9 Parcel injection rate

The number of parcels/s injected into the domain affects the statistical significance of the results, especially when sampling each parcel on a plane or interface downstream of the injection point. In Figure 6.1.17 and 6.1.18 the results are compared without respect to interface sampling effects. The results show steady spray dynamics and droplet evaporation rates for parcel injection rates down to about 100 parcels/ms but this conclusion is assumed to be case dependent.

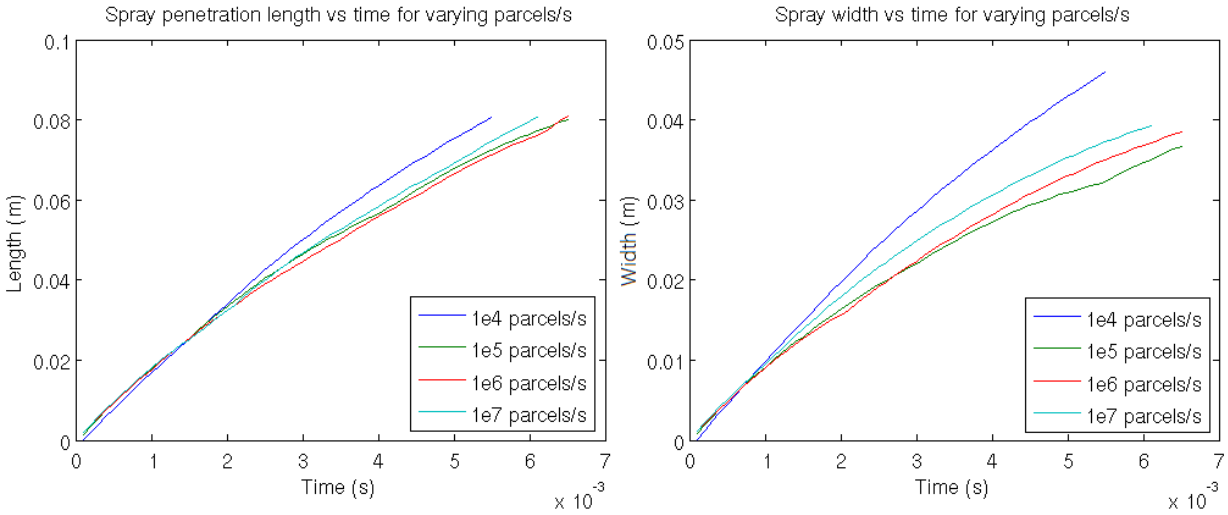

Figure 6.1.17: *Spray penetration and width for varying parcel injection rates*

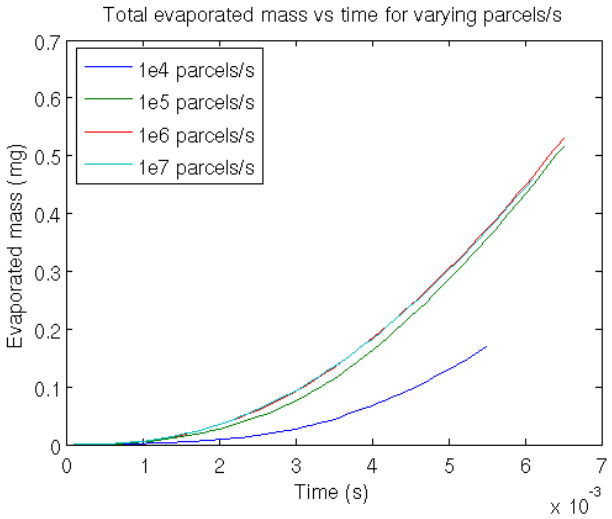

Figure 6.1.18: *Evaporation for varying parcel injection rates*

6.1.10 Collisions

The sensitivity to collisions was evaluated by comparing the results for simulations with and without modeling of collision, see Figure 6.1.19 and 6.1.20. Modeling of collsions resulted in decreased penetration velocity and a narrower spray with lower droplet evaporation rates for a fixed penetration length.

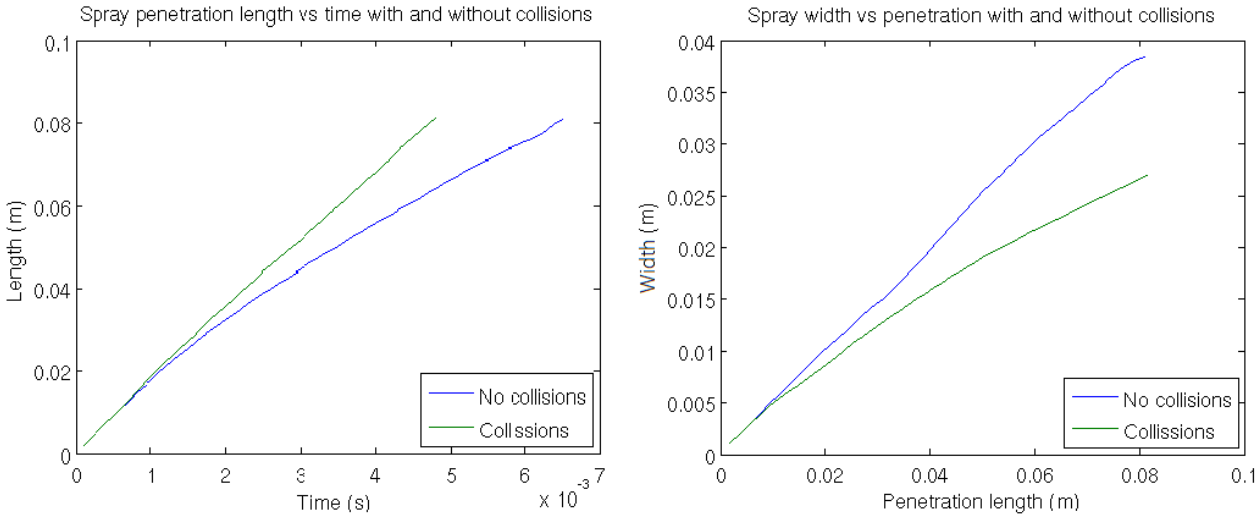

Figure 6.1.19: *Spray penetration and width with and without modeling of droplet-droplet collisions*

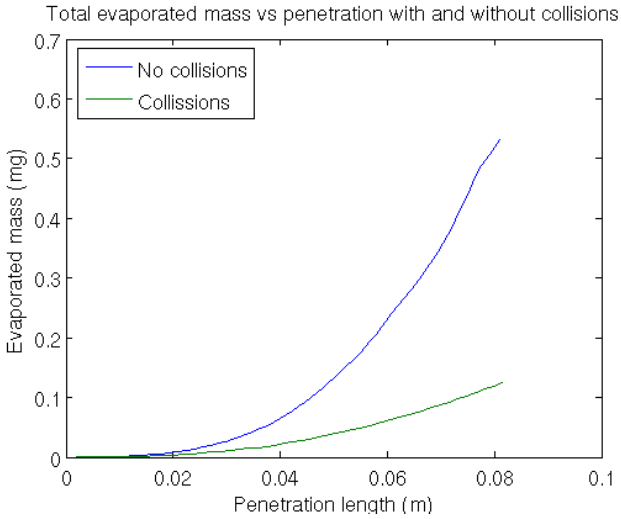

Figure 6.1.20: *Evaporation with and without modeling of droplet-droplet collisions*

6.2 Channel flow with spray and wall interaction

The wall iteraction sensitivity to modeling of fluid film and collisions are shown in Figure 6.2.1 and Figure 6.2.2. Droplet coalescence is included in the collision model used, this is the only phenomena that can result in droplet sizes larger than the initially injected droplet diameters. This is clearly shown in Figure 6.2.1, where the simulations without collisions resulted in an outlet droplet diameter range from 9.5-10 μm, with an average of 9.89 μm and standard deviation of 0.6 %, while simulations with collisions activated resulted in a diameter range from 8-200 with an average of 14.8 μm and a standard deviation of 67 %.

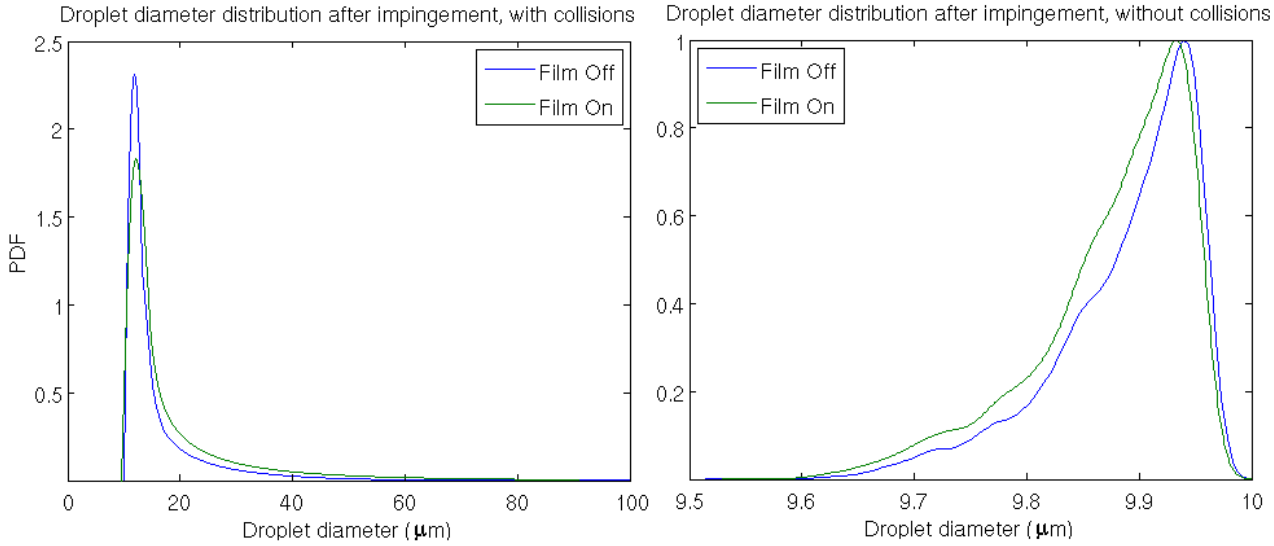

Figure 6.2.1: *Probability density functions of droplet diameters sampled on outlet boundary with and without modeling of fluid film and droplet-droplet collisions*

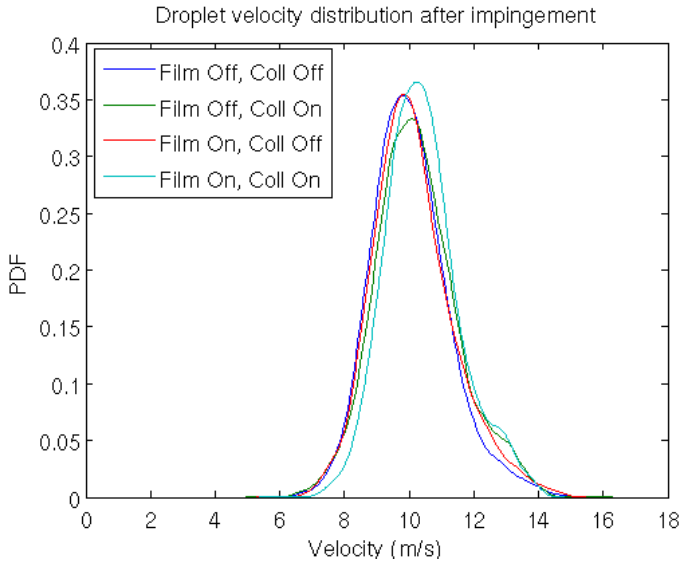

Figure 6.2.2: *Probability density functions of droplet velocities sampled on outlet boundary with and without modeling of fluid film and droplet-droplet collisions*

Modeling of fluid film on the lower spray impingement wall boundary did not have a significant impact on post-impingement droplet velocity and diameter distributions measured on the outlet boundary of the region, regardless of whether droplet-droplet collisions were modeled or not. Collisions resulted in a slightly higher standard deviation of droplet velocity with 12.6 % compared to 11.5 % without collisions. Film resulted in 1.3 % higher mean velocity.

6.2.1 Sensitivity to cell size

The whole region was meshed and simulated with homogeneous hexahedral cells with side lengths from 0.5-6 mm. The film thickness was integrated over the film affected area on the wall and multiplied with the average film density to give the total mass of agglomerated fluid film. The film mass was compared to the total injected spray mass of a single pulse to form the mass fraction of droplets transformed into film on the wall. This is shown for different cell sizes to the left in Figure 6.2.3.

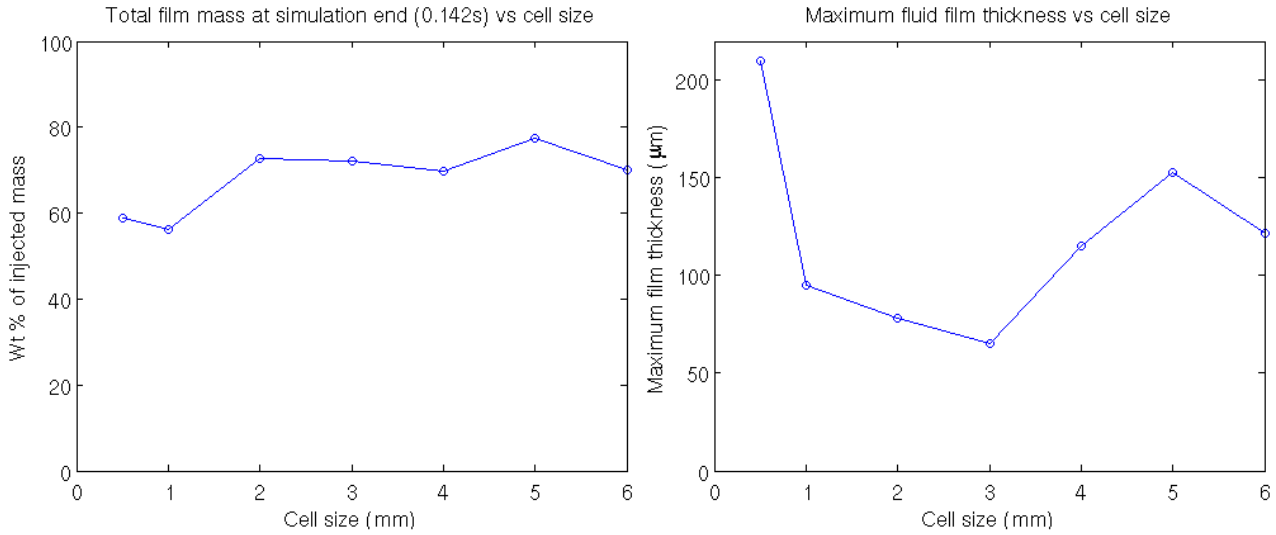

Figure 6.2.3: *Mass fraction of spray to form fluid film and maximum film thickness for varying cell size*

To the right in Figure 6.2.3, the maximum wall film thickness for different cell sizes is shown. It is clear that this is a less predictable measurement of the behaviour of the film since it is dependent of the statistics of a parcel impinging on a single cell. The asymptotic effect of the maximum thickness measurement when the cell size approaches zero and causing instabilities and divergence problems is a reason not to refine the mesh too much on fluid film boundaries.

6.3 Tetra Pak A6 evaporator

The experimental data was post-processed to visualise the average and Sauter mean diameters, velocity and standard deviation distributions across the width of the spray 27 mm downstream of the spray nozzle. Probability and cumulative density functions were produced for both diameter and velocity to visualise the statistical distributions. To get statistically significant results only the measurement points within a radius of 13 mm from the spray center were analysed. According to numerical simulations, this range covers 99.9 % of the droplet massflow, see Figure 6.3.10.

6.3.1 Experimental measurements

Since the droplet flow rate was significantly higher close to the centerline of the spray than in the periphery but the sampling is done for a similar number of droplets for each measurement coordinate the overall average velocity and diameters were over-influenced by the peripheral droplets. A total of 1 549 700 droplets were analysed. Unrealistic data samples, such as high negative velocities due to measurement problems of non-spherical droplets were removed. The test was set up and post-processed using the methodology described in Section 5.6. The results are compared to the numerical simulations in Section 6.3.3.

The left half of Figure 6.3.1 shows that the measured droplet diameters varies from very small to about 190 μm for all test points over the central cross section of the evaporator. The rings represents the average diameter for each test point. The right half shows that the standard deviation of droplet diameters is of the same order of magnitude as the average values with a 30 % lower standard deviation in the outer parts than in the central parts of the spray in the radial direction. This is assumed to occur due to a combined effect of higher volume fraction and collision probability in the central parts, with a higher collision rate leading to a wider diameter distribution in combination with that some of the injected droplets passes outside the nozzle cup without breaking up through wall impingement. According to simulations these droplets passes the measurement plane at an average spray radius of approximately 2 mm, resulting in larger droplets and a higher standard deviation in the central parts of the spray.

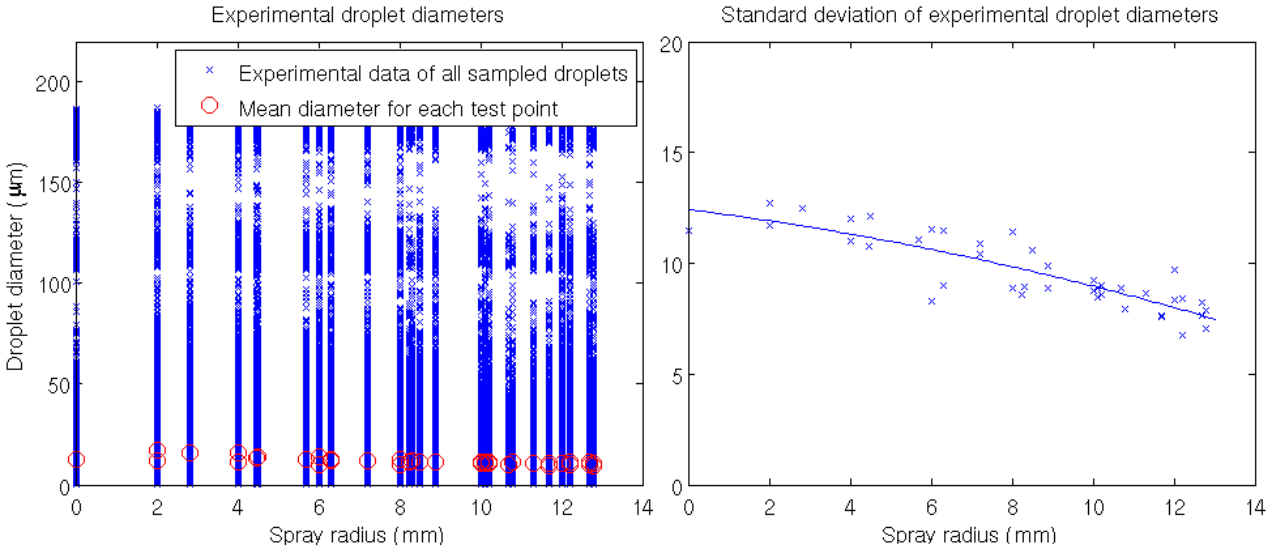

Figure 6.3.1: *Measured droplet diameters and average diameter per test point*

The left part of Figure 6.3.2 shows that the averaged measured droplet diameters decreases almost linearly with increasing spray radius. In the outer region the velocity of the surrounding fluid is lower due to lower volume fractions and thereby lower momentum transfer. This results in higher slip velocities, higher We, more breakup and smaller droplets in the outer regions. The passing droplets described in the last section are also assumed to result in larger droplets in the central region. The lower droplet velocities in the peripheral also increases the droplet residence time which gives a higher fraction of evaporated droplet mass before the measurement plane and thereby smaller diameter droplets. Considering all sampled droplets gives an average

diameter of 11.7 μm with a standard deviation of 9.8 μm. The average diameter measured in the middle is 25 % larger than the average diameter of all sampled droplets while the average diameter at a radius of 13 mm from the spray center is 14 % lower than the overall mean value.

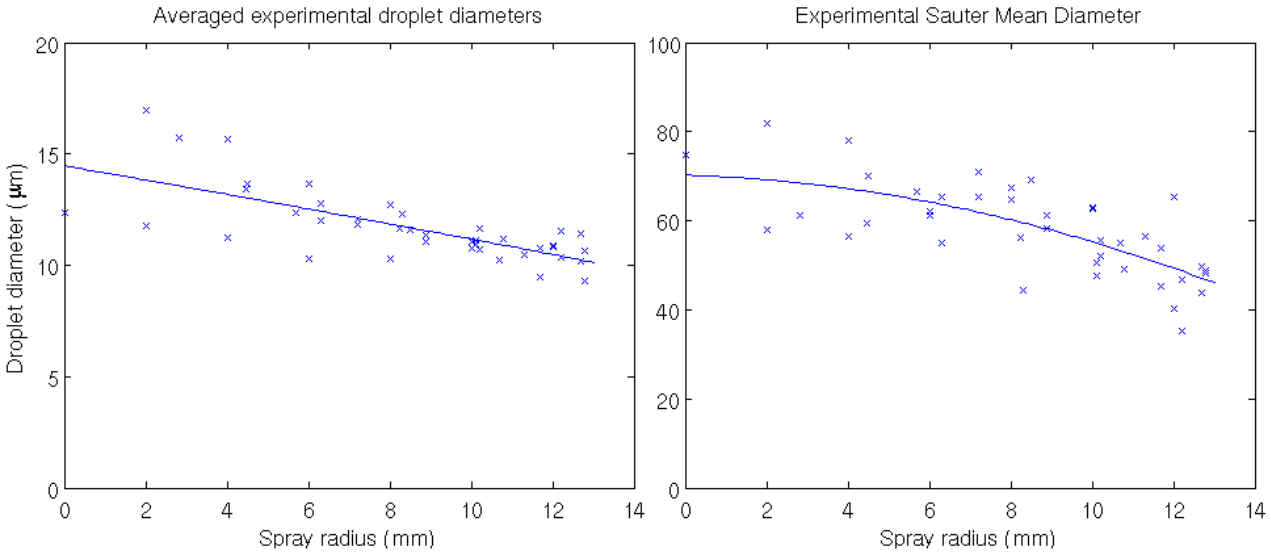

Figure 6.3.2: *Average droplet diameter and Sauter mean diameter profiles*

The Sauter mean diameter takes the importance of larger droplets into account on mass transfer and evaporation rates by increasing the influence of these droplets on the mean diameter measure. The Sauter mean diameter of the entire droplet sample, 59.4 μm, was measured to be four times higher than the average diameter. In the same way as the average diameter the Sauter mean diameter decreases further away from the center of the spray.The right part of Figure 6.3.2 shows the Sauter mean diameter d_{32} profile defined for every test point as

$$d_{32} = \frac{\sum d^3}{\sum d^2}$$

The diameter distributions are visualised by the probability and cumulative density functions and compared to the numerical distributions in Figure 6.3.13. The result shows that 44 % of the droplets are in the diameter range of 10-20 μm, 49 % of the diameters are below 10 μm and 1 out of thousand droplets is sub-micron size. 1 % of the spray consists of large droplets with diameters over 40 μm and about one per mille above 170 μm.

The left part of Figure 6.3.3 shows the average vertical velocity for each measurement point with an overall mean velocity of 15.5 m/s and standard deviation of 6.1 m/s for all sampled droplets. The average velocity decreases towards the outer region of the spray due to decreasing momentum transfer, increasing slip velocities and drag forces as well as smaller droplet diameters that are more heavily affected by the velocity of the surrounding fluid. As shown in the right figure the standard deviation of the velocity increases with increasing spray radius due to the decreasing volume fraction, momentum transfer and homogeneity.

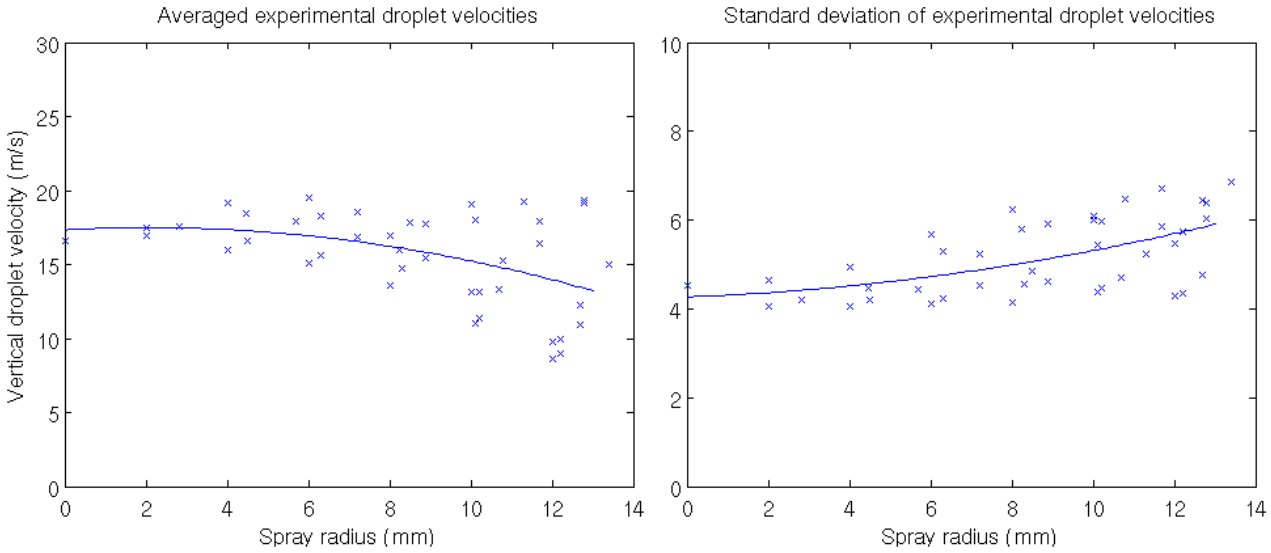

Figure 6.3.3: *Average droplet velocity profile and standard deviation over the cross-section*

The velocity distributions for all measurement points combined are shown statistically as probability and cumulative density functions in Figure 6.3.10. The measurement results show that 89 % of the droplet velocities are in the range 5-25 m/s, 58 % are between 10-20 m/s, 1 % is below 1 m/s and 1 % is above 30 m/s.

6.3.2 Numerical simulation

The simulations were set up according to the methodology described in Chapter 5 and Section 5.5 in particular. The results from the numerical simulations are compared to the experimental reference in Section 6.3.3.

Steady state with air-assistance and heating air flow only

The resulting scalar fields for pressure, static temperature, turbulent kinetic energy, turbulent dissipation rate, species mass fraction and the velocity vector field from the single-phase, steady-state RANS simulation was used as initial conditions for the unsteady spray simulations.The steady state velocity on the inlet boundary was used as velocity inlet condition. The steady temperature and velocity fields are visualised in Figure 6.3.4.

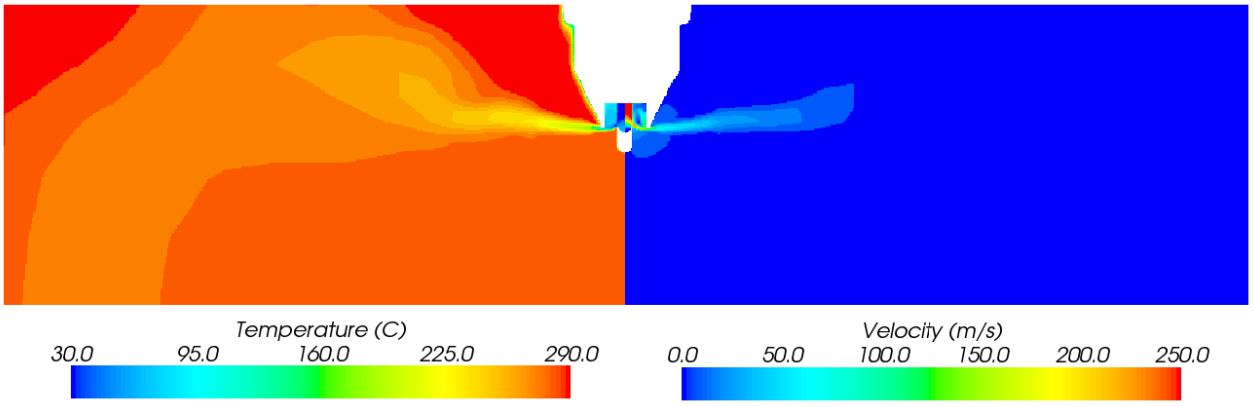

Figure 6.3.4: *Steady state temperature and velocity fields*

Unsteady Eulerian-Lagrangian spray simulation

The swirling air flow around the sides of the nozzle and the increased air velocity due to the strong momentum coupling downstream of the nozzle are shown as a line integral of the velocity vector in Figure 6.3.5.

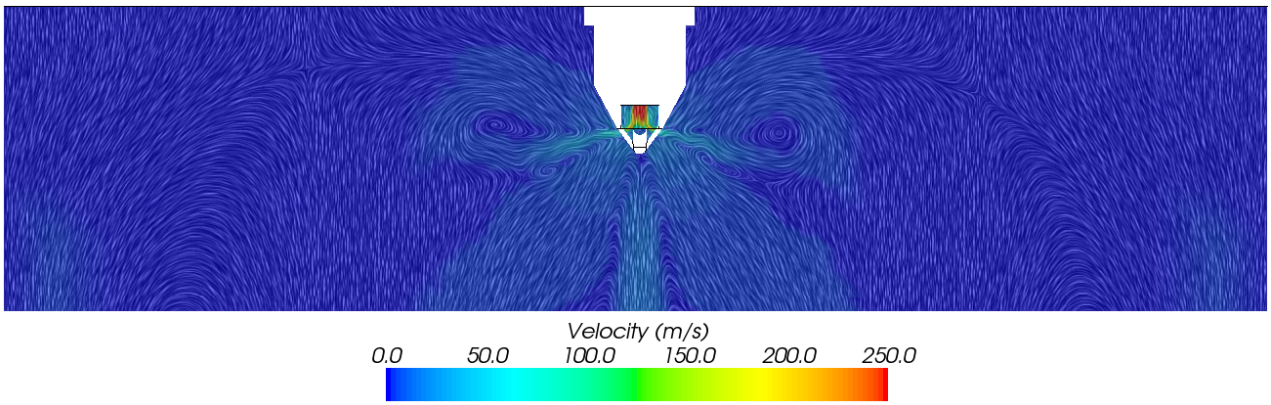

Figure 6.3.5: *Line integral convolution of the flow, coloured by absolute velocity*

The unsteady fluctuations occurring just outside of the nozzle outlets and how the heated airflow around the nozzle is cooled down by the ambient liquid spray droplets are shown in Figure 6.3.6.

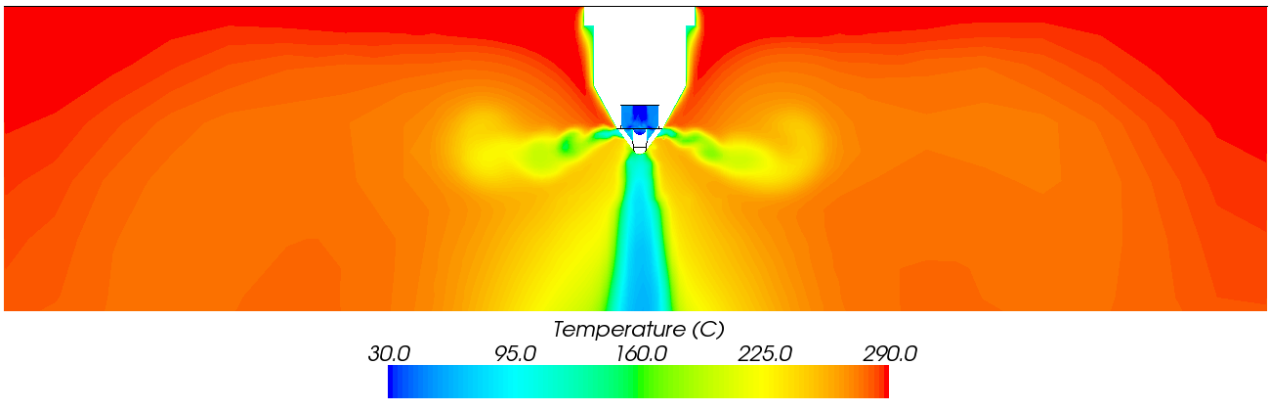

Figure 6.3.6: *Temperature field*

Figure 6.3.7 and 6.3.8 show the mass fractions of the vaporised droplet components in the heated airflow in the evaporator around the nozzle.

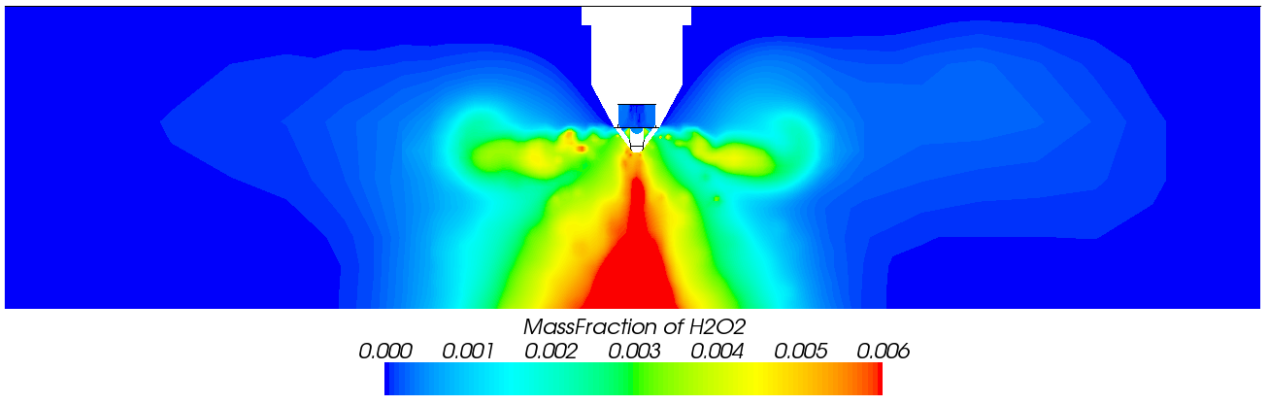

Figure 6.3.7: *Mass fraction of hydrogen peroxide vapour*

The figures show an almost ten times higher mass concentration of steam than hydrogen peroxide in the top of the evaporator due to the higher relative droplet evaporation of water.

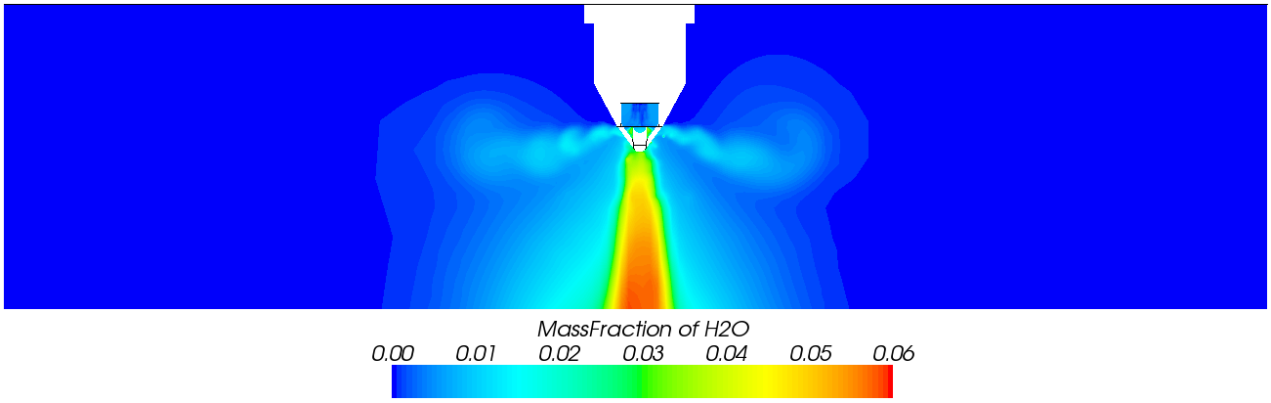

Figure 6.3.8: *Mass fraction of steam*

Figure 6.3.9 shows the distribution of small and large droplets and their representative velocities in the spray. The largest dots represents droplet diameters 0.3-1.2 mm. Each point in the figure corresponds to one parcel, which represents about 0.2-10000 droplets, this reduces the impact of the large diameter parcels shown in the figure since they generally have a low droplet count below unity.

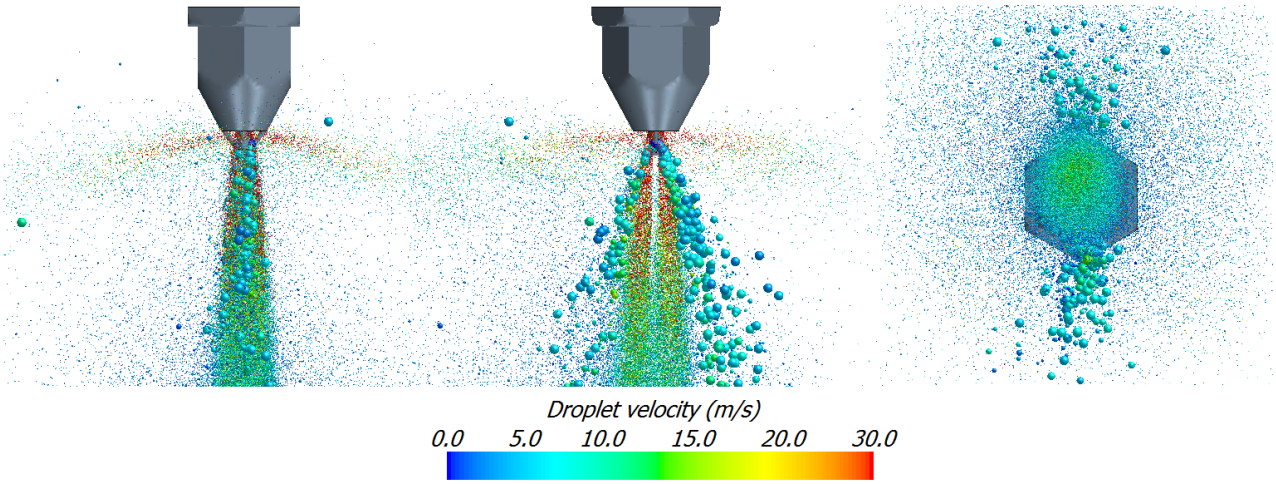

Figure 6.3.9: *Spray visualisation, coloured by absolute velocity, sized by droplet diameter*

The approximate droplet mass flux distribution as a function of radial distance from the spray center is shown in Figure 6.3.10. It shows that the majority of the droplet mass flow is centred around the middle of the spray with 99.9 % within a distance of 14 mm from the spray center.

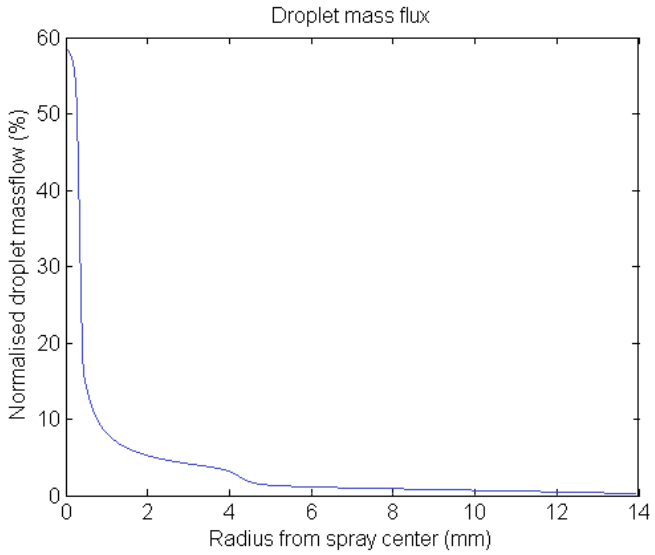

Figure 6.3.10: *Droplet mass flux*

Simulation using quarter geometry and symmetry planes

The Eulerian-Lagrangian spray modeling in combination with symmetry planes resulted in convergence problems and extreme velocities and temperatures in the internal and external fluid regions of the nozzle head. To solve this problem the time step was reduced, which resulted in similar simulation times as the standard solutions. Tracking inaccuracy due to the symmetry planes was observed in early and intermediate results, unphysical behaviour such as droplets avoiding the coordinate axes and symmetry planes. Compared to the experimental droplet velocity and diameter profiles and density functions the accuracy of the quarter geometry simulation is of the same magnitude as the full geometry simulations, see Figure 6.3.11 to 6.3.13.

Improvement of thermal boundary conditions

It is uncertain whether the increase of a few degrees in the spray mixture injection temperature had any significant influence on the droplet evaporation or the diameter and velocity distributions on the interface downstream of the nozzle since the energy needed to increase droplet temperature from 30 to 35 °C only corresponds to approximately 1.5 % of the total energy needed to evaporate a 30 °C droplet, due to the high relative effect of the latent heat of vaporisation. See results in Appendix B.

The change in nozzle head surface temperature did not have any significant effect on the spray nozzle performance due to the fact that the wall behind a fluid film covered surface in STAR-CCM+ is always thermally modeled as adiabatic. It did however have a slight effect on the temperature of the pre-heated airflow close to the nozzle head surface. See results in Appendix C.

6.3.3 Comparison between numerical and experimental results

The experimental test results and the numerical simulation results were compared by their average and standard deviation of droplet diameter and velocity against the radial distance from the center of the spray. The diameter and velocity distributions were statistically evaluated and compared using probability density functions. All cases presented in this section were run with modeling of collisions. Four different numerical cases were compared to the experimental reference. The first case was run on the standard geometry with modeling of fluid film and with normally distributed droplet injection diameters with a mean of 10 μm and standard deviation of 5 μm. The second case was run without fluid film. The third with a mono-dispersed droplet diameter injection with diameter 10 μm. The last case was run using symmetry planes and a quarter of the standard geometry, without fluid film. The average and standard deviation of droplet diameters for the

different cases and the experimental reference are shown in Figure 6.3.11, plotted against radial distance from the center of the spray. Due to the droplet mass flow profile shown in Figure 6.3.10, the significance of the diameter and velocity profiles reduces drastically 0-4 mm from the center of the spray and does not affect the overall performance of the spray further away.

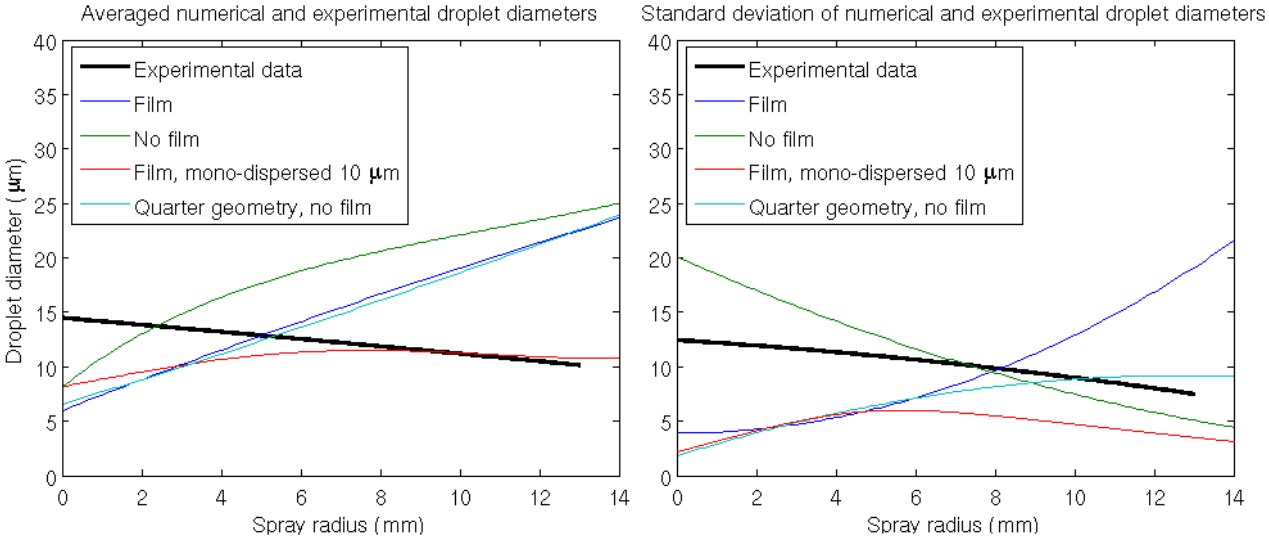

Figure 6.3.11: *Comparison of droplet diameter profiles*

The average numerical diameters seem to increase further away from the center while the average decreases slightly in the experimental reference case. The average and standard deviation of droplet velocity are visualised in the same way in Figure 6.3.12. Further conclusions will not be drawn considering the insignificance of the average diameter and velocity profiles in the outer regions of the spray.

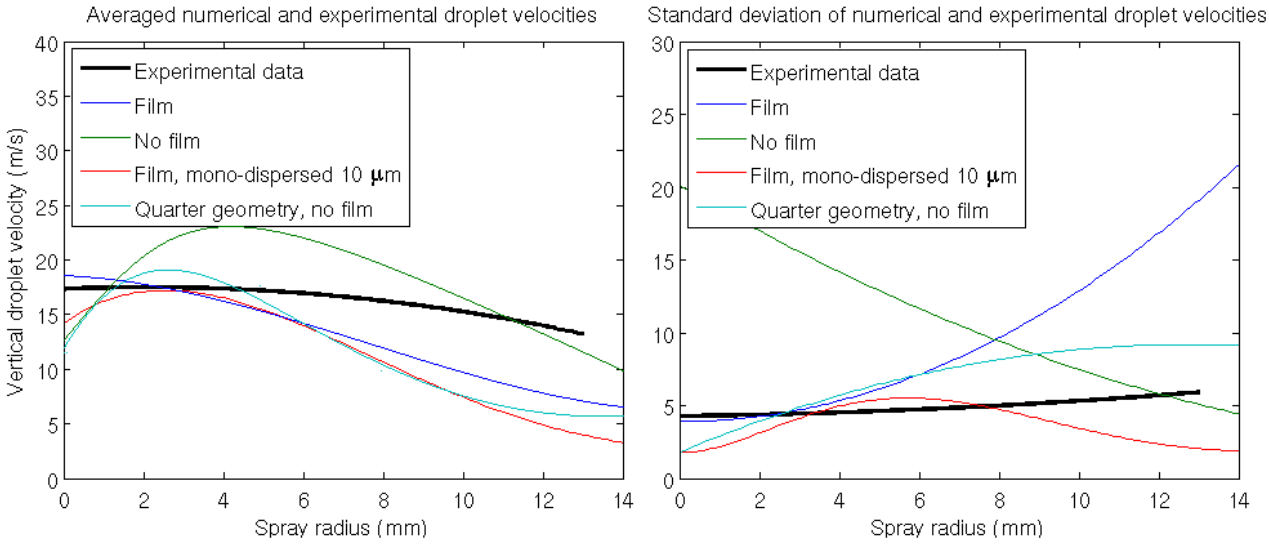

Figure 6.3.12: *Comparison of droplet velocity profiles*

The probability density functions for droplet diameter and velocity distributions in Figure 6.3.13 were produced using the statistical ksdensity function in Matlab, returning a probability density estimate based on a normal kernel function with 200 equally spaced bins for the numerical data and 1000 bins for the experimental droplet samples. Simulations with and without modeling of fluid film on the internal nozzle surfaces showed little to no difference in final results. Mono-dispersed injection of droplets resulted in good velocity conformance but a peaking probability of droplet diameters around the specified injection size. Simulation using symmetry planes resulted in poorer but acceptable results considering both velocity and diameter probability distributions. Considering the simulation time was very similar to the others cases, this approach is not recommended for this type of spray simulations.

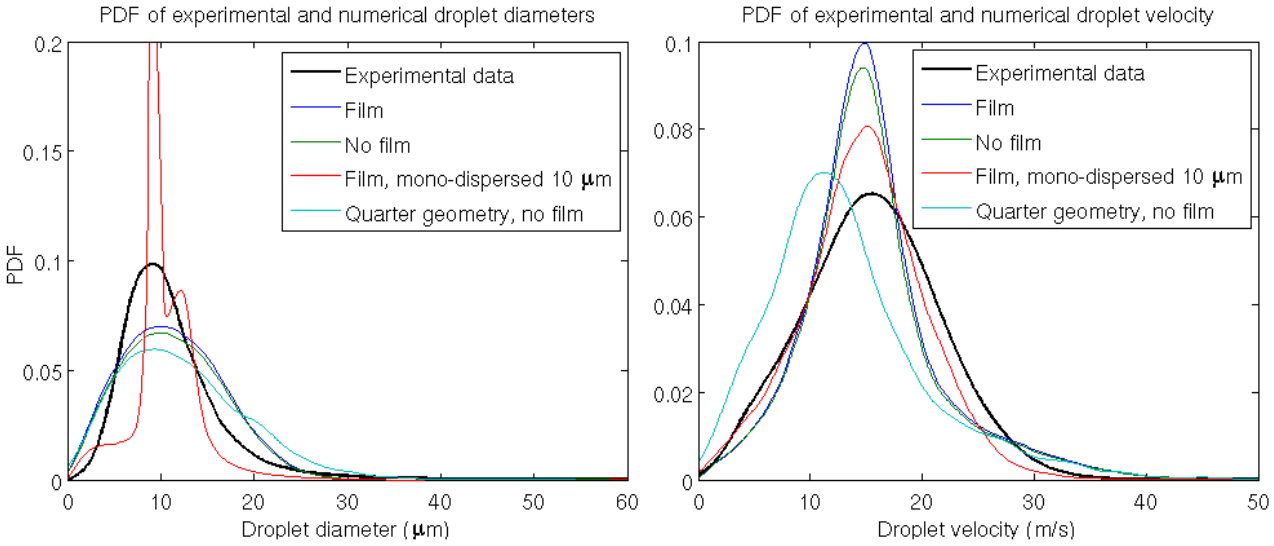

Figure 6.3.13: *Comparison of probability density functions for droplet diameter and velocity*

Average and standard deviation of droplet diameters and velocities are tabulated for comparison in Table 6.3.1. The average numerical Sauter mean diameter turned out to be 75 % lower than the experimental. The other properties were about the same range as the experimental reference. The result from the initial simulation with mono-dispersed droplets of 10 μm turned out with a very low standard deviation of droplet diameters, as expected.

Table 6.3.1: Comparison of overall averages and standard deviations

Case	Avg v (m/s)	Std v (m/s)	Avg d (μm)	Std d (μm)	SMD (μm)
Experimental	15.5	6.1	11.7	9.8	59.4
Film	15.3	4.1	6.7	4.6	12.5
No film	20.4	15.6	9.2	6.5	21.4
Film, mono-dispersed 10 μm	17.8	6.9	13.4	3.6	14.2
Quarter geometry	14.2	7.3	8.5	4.9	13.5

7 Conclusion and Recommendations

The spray itself has not shown to be very mesh dependent. Unlike single phase simulations, for which the accuracy of the simulation principally improves with decreased cell size until all scales of the flow are resolved, Eulerian-Lagrangian simulations are sensitive to exaggerated mesh refinements. Too small cells, with an order of magnitude close to the droplet diameter, can cause numerical instabilities for the Lagrangian phase. The instabilities might even spread and contaminate the surrounding fluid if the phases are two-way coupled.

Mesh refinements on fluid film boundaries improves the resolution and dynamics of the film but extreme refinements have shown to lead to overprediction of local film thickness in individual cells due to the increased significance of a single parcel. The total film volume has on the other hand shown to be fairly mesh independent.

To set up a general spray simulation, use a cell size that is fine enough to accurately represent the important details of the geometry but is still several times larger than the largest droplet diameters. Implement prism layers to resolve the boundary layers using wall functions as for a single phase simulation. Refine the mesh in high gradient regions and increase the cell size far away from intensive areas. Refining the mesh too much does not lead to a more accurate solution as in single phase flow. Use hexahedral cells for a propitious balance between simulation time and numerical accuracy. Setup related recommendations are presented in the following points.

- Using symmetry planes to reduce the number of cells in a spray simulation often leads to convergence problems and parcel tracking inaccuracies. Convergence problems can be solved by reducing the Eulerian time step but this results in longer simulation times, thus the advantage of using symmetry is gone.
- Decrease the inner iterations for the Eulerian phase to between 3-10 (default 25). Use a time step as coarse as possible while still resolving the transient effects of the mean flow and avoiding divergence, up to about one millisecond for low velocities. For high velocities and complex geometries a time step of 10^{-5} to 10^{-6} s might be required. A parcel injection rate of 10^2 - 10^3 parcels per millisecond has shown to be sufficient in most cases, not considering parcels transmitting into fluid film and decreasing the actual number of parcels in the region.
- To find a suitable droplet injection velocity, start with a lower droplet injection velocity than expected, this way the time step can be increased without divergence and preliminary results can be obtained faster. In this case the initial assumption was to set the injection velocity equal to the air-assistance velocity, simulations showed that the correct value was closer to 1/3 of the air velocity. Since the average velocity and diameter does not vary more than a few percent in the significant area in the spray center, representing the majority of the droplet massflow, it might be an idea to use a simplified experimental measurement technique sampling form only one point. Significant reductions in experimental and simulation time would be possible with an accurate method for estimating the injection velocity of the spray droplets. Normal distributed droplet injection velocities would widen the probability function for droplet velocity and bring the simulation results even closer to reality.
- Run the Lagrangian solver every Eulerian time step for time steps in the order of magnitude of 10^{-5} s and shorter depending on droplet velocity, to save simulation time. Run the solver every iteration for time steps coarser than 10^{-5} s to maintain accuracy. Monitor and decrease the maximum number of Lagrangian iterations or sub-steps continuously during the simulation until about 1 % of the parcels reach the maximum number of sub-steps, to decrease simulation time and avoid simulation time to be spent on problematic parcels. 1 % generally corresponds to a maximum number of substeps in the range 20-400, depending on the flow and the strength of the coupling between the phases.
- Modeling of fluid film can complicate convergence but decrease simulation time by swallowing parcels. Including fluid film did not lead to major differences in velocity and diameter distributions. A disadvantageous consequence of modeling fluid film is that it makes it harder to estimate the parcel injection rate required to be able to obtain statistically significant results, especially when sampling droplet diameter on interface planes. Film related divergence can be avoided by decreasing the under relaxation factors for the film velocity and thickness and narrowing the allowed temperature ranges for both film and continuum. Narrowing the polynomial range for specific heat to helps avoid negative latent heat of vaporization due to higher liquid than gas enthalpies at extreme temperatures. The maximum temperature in the

Antoine equation for the film constituents can also be specified higher than the expected temperature to avoid the saturation pressure from not increasing monotonically with temperature.

- Modeling of droplet collisions have a significant effect on diameter distribution downstream of the injection point, especially for dense sprays and nozzle geometries with internal wall interactions. Collision modeling has not shown to have a significant impact on simulation time.

The wide diversity of multiphase flow applications in industry will continue to drive the need for better predictive models and measurement techniques, even for spray simulations. In the same way as spray models were developed specifically for diesel injection sprays, models developed and adapted specifically for other applications will probably approach when the industry becomes more mature. In the future, adaptive methods capable of changing and optimising model parameters during the simulation, for improved accuracy and simulation time consumption may even be used.

Appendices

A Dimensionless numbers relevant for this case

The Stokes number is a measure of how fast a particle or droplet reacts to changes in the flow field. For Stokes numbers much smaller than unity the particle is said to be in velocity equilibrium with the carrying phase and it quickly follows every small change in the flow. When close to unity the particle follows the major changes in the flow and at very high Stokes numbers the motion of the particle will be essentially unaffected by the flow. The Strokes number is defined as the ratio of the particle response time to a characteristic time of the flow

$$St = \frac{\tau_{xp}}{\tau_f}$$

where the time scale of the continuum $\tau_f = L_f/U_f$ and the particle response time for a general case is

$$\tau_{xp} = \frac{\rho_p d_p^2}{18\mu_f} \frac{24}{C_D Re_p}$$

for which the last fraction equals unity for Stokes flow. The indices c and p indicates the continuous and particulate phases, index rel represents the slip velocity or relative velocity between the phases. The Reynolds number is the ratio of inertial forces to viscous forces in the flow used to characterise flow regimes such as laminar and turbulent flow. It is often the result of dimensional analysis of fluid dynamic problems and is commonly used to determine the dynamic similitude between different experimental cases such as small scale and full scale testing. It is defined based on a characteristic length scale of the flow as

$$Re = \frac{\rho_f u_f L_f}{\mu_f}$$

On the other hand the particle Reynolds number is based on the diameter and relative velocity between the particle and the surrounding fluid. It is important for estimating the forces on the particle and it is defined as

$$Re_p = \frac{\rho_f |u_{rel}| d_p}{\mu_f}$$

The Weber number is a ratio of destructive droplet inertia to constructive droplet surface tension. The Weber number is a measurement of the instability of a droplet and is important for the modeling of secondary droplet breakup and drag correction. It is defined as

$$We = \frac{\rho_f |u_{rel}|^2 d_p}{\sigma_p}$$

The Laplace number, also known as the Suratman number is the ratio of surface tension to viscous forces and describes the relative significance between the two. It is used in the Bai-Gosman wall impingement model and defined as

$$La = \frac{\rho_p \sigma_p d_p}{\mu_p^2} = \frac{Re^2}{We}$$

The particle Nusselt number is a heat transfer coefficient representing the ratio of the convective to conductive heat transfer coefficient, used when modeling droplet evaporation. It is defined as

$$Nu_p = \frac{h d_p}{k}$$

Associated to the particle Nusselt number the particle Sherwood number Sh_p is a mass transfer coefficient or conductance, representing the ratio of convective to diffusive mass transport. Both numbers are generally

defined empirically using the Ranz-Marshall correlation [28], suitable for viscous flows and particle Reynolds numbers below 5000.

The Eötvös number is used together with the Morton number to describe the shape of deformed drops or bubbles moving in a surrounding fluid. It is proportional to the ratio of buoyancy force to surface tension and defined as

$$Eo = \frac{g|\rho_f - \rho_p|d_p^2}{\sigma_p}$$

The Morton number is only dependant on the properties of the continuous phase but is used in drag correction laws to predict the transition between particle Re_p dependent behaviour and surface tension dominated behaviour.

$$Mo = \frac{g\mu_f^4}{\rho_f \sigma_p^3} = \frac{We^3}{FrRe^4}$$

The Froude number represents the ratio of body inertia to gravitational force and is used to determine the drag force of a partially submerged objects. It is defined in different ways depending on application but a common definition is

$$Fr = \frac{u_p^2}{gd_p}$$

The Ohnesorge number relates the viscous effects to the inertial and surface tension forces. It is used in the modeling of secondary droplet breakup and is defined as

$$Oh = \frac{\mu_f}{\sqrt{\rho_f \sigma_p d_p}} = \frac{\sqrt{We}}{Re_p}$$

Other industrial spray application such as diesel spray with combustion or urea spray with chemical reactions in after treatment systems involve additional dimensionless numbers.

B Estimation of spray injection temperature

This investigation will estimate the spray temperature for the pressurised air and liquid droplets exiting the injector. The steady-state temperature was calculated using two different simplified approaches and steady state RANS. The first was to model the surface temperature distribution on the nozzle head by modeling conjugated (coupled) heat transfer between the whole solid nozzle head and the heated airflow around it. The second was to consider flow inside a solid tube with length equivalent to the real tubes and nozzle, surrounded by a flow of hot air for water and air respectively. The solid was modeled using the properties of standard UNSS30200 stainless steel with an initial temperature of 290 °C. In both approaches the internal solid heat conduction was discretized using the finite volume method [5].

In the first approach the spray was simplified and modeled as only being the air assistance airflow through the thin tubes and the nozzle equivalent to 250 m/s and an injection temperature of 30 °C. A radial airflow of 80 kg/h at a temperature of 290 °C was set for the perforated tube where all the air enter the evaporator, see Figure B.0.1. The perforated plate around the waist of the nozzle was modeled as a porous baffle region with an assumed porosity of 0.5. A semi-conformal hexahedral mesh with contact interfaces and 340 000 solid cells and 2 million fluid cells, refined around the nozzle and the thin tubes was used.

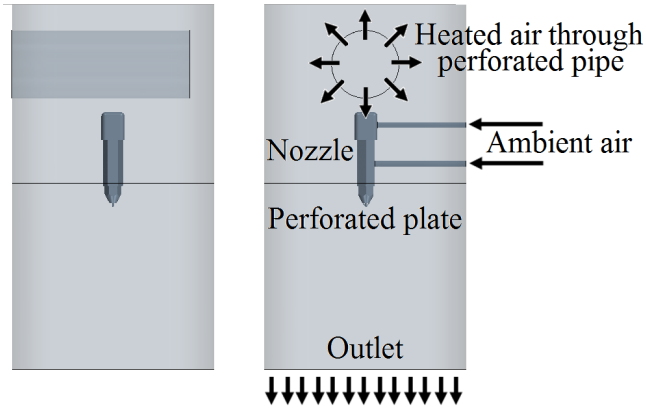

Figure B.0.1: *Geometry and setup*

When using equivalent polyhedral and trimmed hexahedral cells the values for the temperature probes in the solid nozzle converged after approximately 1100 iterations and 52000 seconds of accumulated CPU time for the polyhedral compared to 500 iterations and 8500 seconds for the hexahedral. The spray injection temperature from simulation of coupled solid/fluid heat transfer with only air assistance of 250 m/s and no liquid air, was 45 °C. The temperature field is shown in Figure B.0.2.

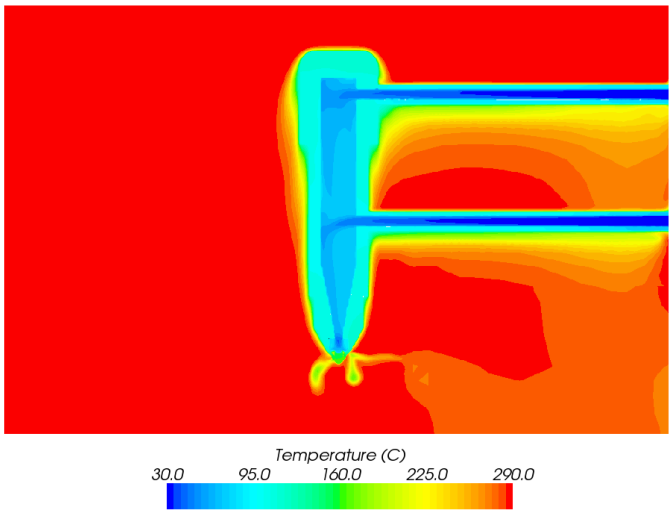

Figure B.0.2: *Instantaneous solid and fluid temperature field*

In the second approach the mesh consists of three different continuum regions, the inner fluid representing the flow of water and air to the nozzle respectively, the solid stainless steel tube with outer diameter 6 mm and thickness 1 mm, as well as the outer fluid region with 290 °C heated air with a vertical velocity of 1 m/s. A conformal polyhedral mesh with contact interfaces and 4×10^3 inner fluid cells, 8×10^3 solid cells and 326×10^3 cells in the outer fluid cells was used. See Figure B.0.3.

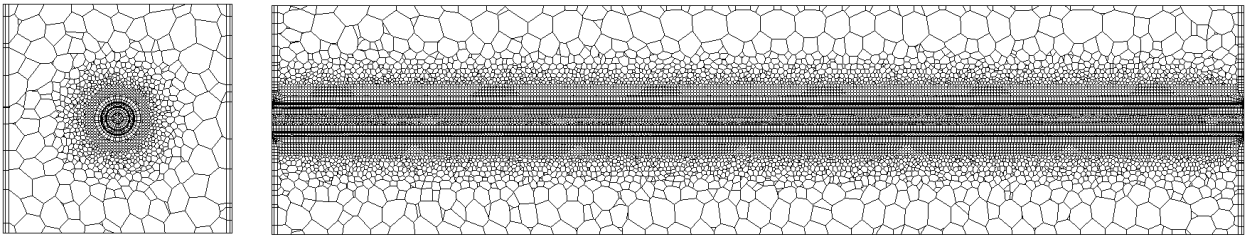

Figure B.0.3: *Mesh used for the pipe approach*

The case was solved using steady-state RANS for a flow of 6.2 kg/h air and 5 kg/h of water respectively. The results for the air and water were investigated and compared to the results obtained using the first approach. The resulting temperature and velocity fields are visualised in Figure B.0.4.

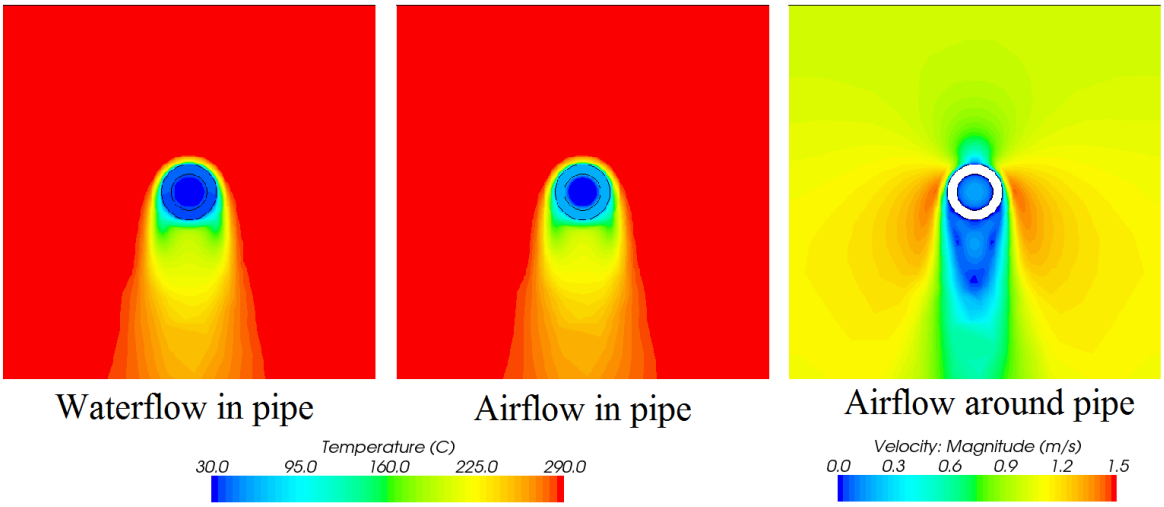

Figure B.0.4: *Cross-sectional solid/fluid temperature and velocity fields for flow of water and air in a thin pipe surrounded by low velocity hot air from the heater*

The result from this setup with internal flow of air gave an average solid tube temperature of 65 °C, average outlet temperature 38 °C, average outlet velocity 126 m/s and an average heat transfer of 12.6 kW/m^2, or 27 W. With internal water flow the simulation results showed an average solid tube temperature of 40 °C, average outlet temperature 34 °C, average outlet velocity 0.17 m/s and an average heat transfer of 14.3 kW/m^2, or 30 W.

If the mixing between air and water in the nozzle is assumed to be complete an energy balance can be set up to describe the combined temperature for the mixture as

$$c_{p,water}\dot{m}_{water}(T_{mixture} - T_{water}) = c_{p,air}\dot{m}_{air}(T_{air} - T_{mixture})$$

Using the mass flows through the nozzle for the spray mixture and the air assistance as mentioned earlier, and the specific capacity of 4181 and 1012 J/kgK for water and air respectively, solving this equation gives an estimated spray outlet temperature for the mixture of 35 °C.

The lower, conservative temperature out of the two approaches was used for further simulations of the spray due to the fact that an overestimated droplet temperature would result in over prediction of the fraction of evaporated droplets further down. This increases the risk of liquid hydrogen peroxide being left in the carton bottle after the swirl of sterile air used to remove the gaseous aseptic treatment.

C Estimation of nozzle surface temperature

This investigation will estimate the surface temperature distribution on the nozzle head by modeling conjugated (coupled) heat transfer between the solid nozzle head and the heated airflow around it. Simulating full unsteady conjugated heat transfer between the solid and fluid implicitly including a dispersed spray phase and fluid film cooling the nozzle surface would have been far too computationally time consuming. For this reason the spray consisting of pressurised air and a liquid water-hydrogen dioxide was modeled using airflow only. The case was solved using steady state RANS simulation. The solid nozzle was modeled using the properties of standard UNSS30200 stainless steel with an initial temperature of 290C and the internal heat conduction in the solid was numerically discretized using the finite volume method [5].

The air representing the spray was injected at the top of the lower nozzle head at 30 °C and 250 m/s. A massflow of 80 kg/h of heated air at a temperature of 290 °C was injected at the top of the surrounding fluid region. A conformal polyhedral mesh with 10^6 fluid cells and 140 000 solid cells and contact interface surfaces was used. The mesh was refined around the nozzle, especially around the the tip and around the central parts of the nozzle in the vertical direction. The resulting surface temperature distribution is visualised in Figure C.0.1.

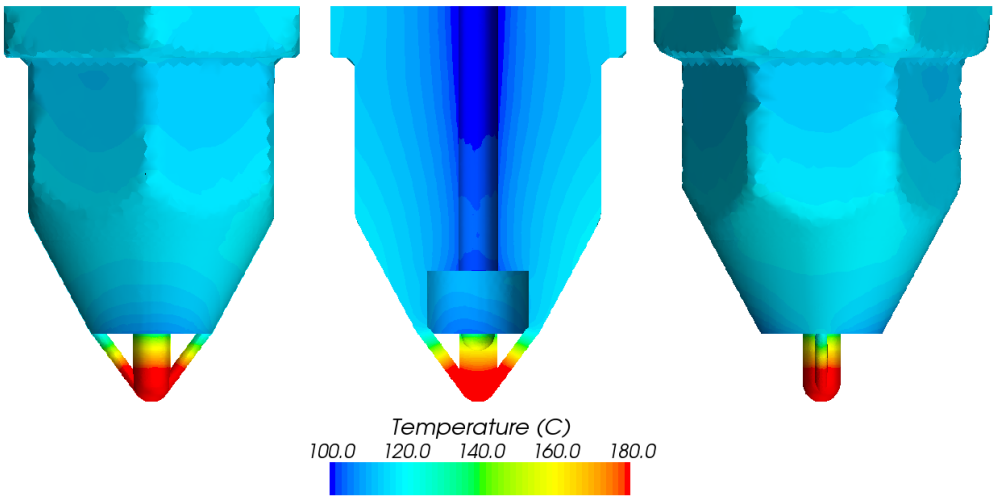

Figure C.0.1: *Nozzle surface and inner cross-sectional temperature fields*

The resulting nozzle head surface temperature from this simulation was exported to a table and used as temperature boundary condition for more the more detailed spray simulations.

D Polynomial droplet properties

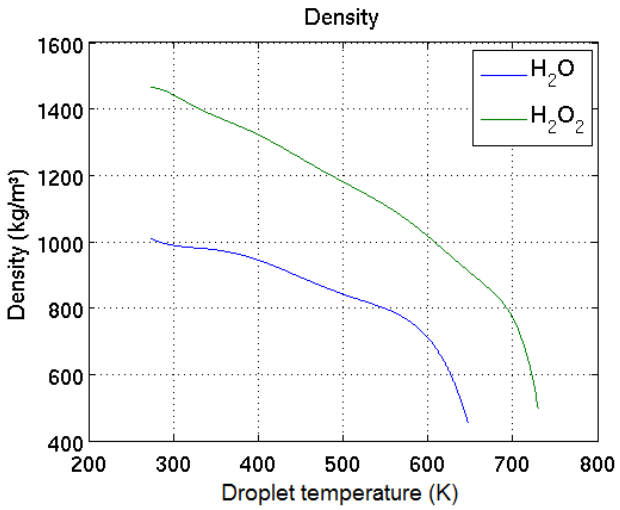

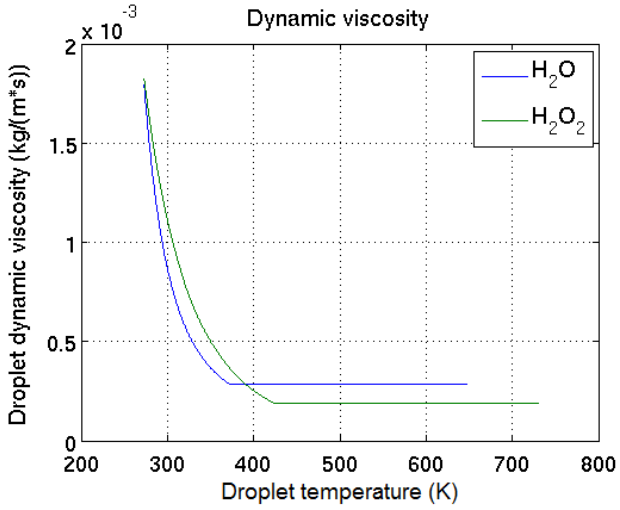

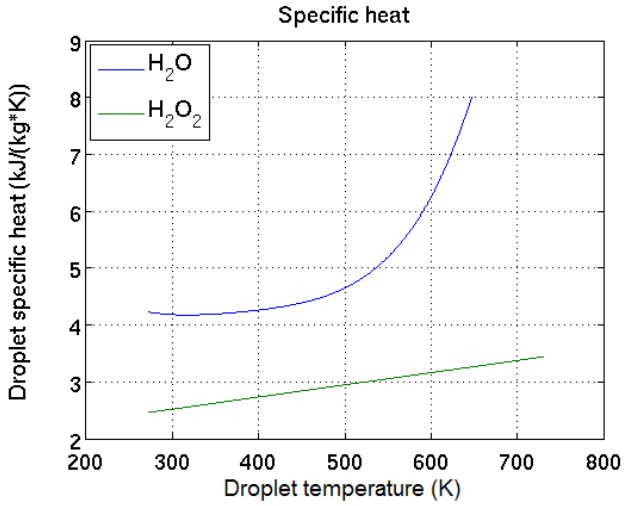

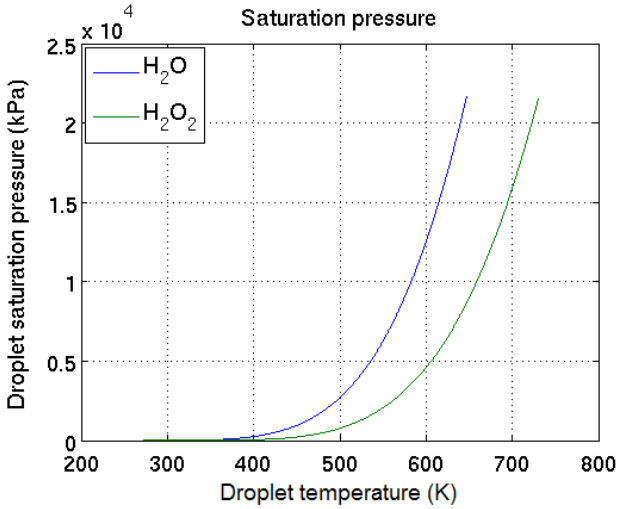

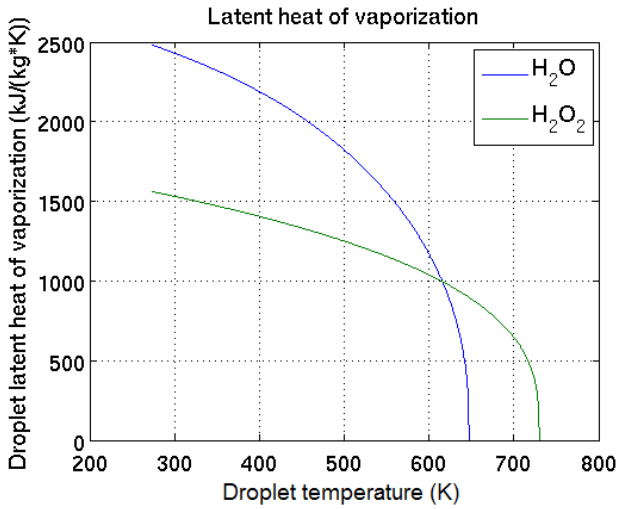

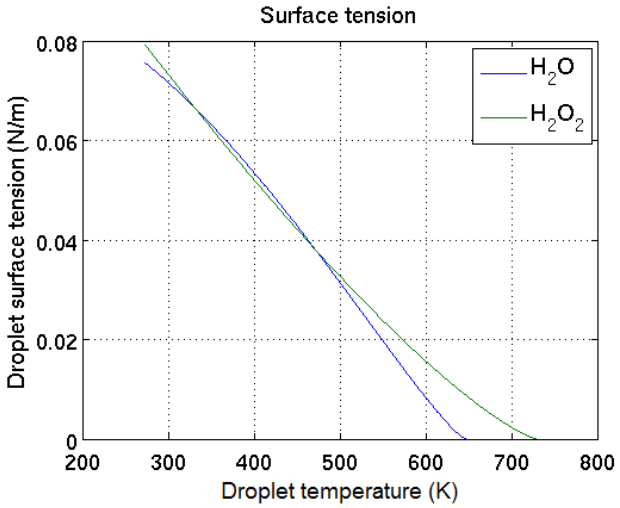

References

[1] T. Arai and H. Hashimoto. *Disintegration of a thin liquid sheet in a concurrent gas stream.* Proceedings of the Third International Conference on Liquid atomization and Spray Systems, London (1985).

[2] N. Ashgriz and SpringerLink. *Handbook of atomization and sprays: theory and applications.* New York: Springer, (2011). ISBN: 9781441972644, 1441972641, 1441972633, 9781441972637.

[3] C. Bai, H. Rusche, and A. Gosman. *Modeling of gasoline spray impingement.* Atomization and Spray (2002).

[4] C. Baumgarten and SpringerLink. *Mixture formation in internal combustion engines.* Berlin: Springer Berlin Heidelberg, (2006).

[5] CD-adapco. *User Guide: STAR-CCM+ Version 8.02* (2013).

[6] S. Chandrasekhar. *Stochastic Problems in Physics and Astronomy.* Reviews of Modern Physics 15.1 (1943), 1–89.

[7] S. Chen and G. D. Doolen. *Lattice Boltzmann Method for fluid flows.* Annual Review of Fluid Mechanics 30.1 (1998), 329–364.

[8] C. T. Crowe. *Multiphase flows with droplets and particles.* Boca Raton, FL: CRC Press, (2012). ISBN: 9781439840504, 1439840504.

[9] C. T. Crowe. *Multiphase Flow Handbook.* Hoboken: CRC Press, (2005). ISBN: 0849312809, 9780849312809.

[10] D. Fuster et al. *Simulation of primary atomization with an octree adaptive mesh refinement and VOF method.* International Journal of Multiphase Flow 35.6 (2009), 550–565.

[11] I. Goldhirsch. *Introduction to granular temperature.* Powder Technology 182.2 (2008), 130–136.

[12] A. Gosman and E. Ioannides. *Aspects of computer simulation of liquid-fuelled combustors.* AIAA, J. Energy (1983).

[13] F. H. Harlow. *Fluid dynamics in Group T-3 Los Alamos National Laboratory.* Journal of Computational Physics 195.2 (2004), 414–433.

[14] B. T. Helenbrook and C. F. Edwards. *Quasi-steady deformation and drag of uncontaminated liquid drops.* International Journal of Multiphase Flow 28.10 (2002), 1631–1657.

[15] J. A. S. Hess. Progress in Aeronautics Sciences 8 (1967).

[16] F. P. Incropera. *Fundamentals of heat and mass transfer.* New York: Wiley, 2007. ISBN: 9780471457282, 0471457280.

[17] J. Ishimoto et al. *Integrated Simulation of the Atomization Process of a Liquid Jet Through a Cylindrical Nozzle.* Interdisciplinary Information Sciences 13.1 (2007), 7–16.

[18] C. Kralj. *Numerical Simulation of Diesel Flow Processes.* Imperial College, London (1995).

[19] A. H. Lefebvre. *Atomization and sprays.* New York: Hemisphere Publishing, (1989). ISBN: 9780891166030, 0891166033.

[20] R. L. Liboff. *Kinetic Theory: Classical, Quantum, and Relativistic Descriptions.* New York, NY: Springer New York, (2003). ISBN: 9780387217758, 9780387955513, 0387217754, 0387955518.

[21] A. Liu, D. Mather, and R. Reitz. *Modeling the Effects of Drop Drag and Breakup on Fuel Sprays.* SAE Paper 930072 (1993).

[22] F. Maroteaux et al. *Liquid film atomization on wall edges - Separation criterion and droplets formation model.* Journal of Fluids Engineering - Transaction of the ASME 124.3 (2002), 565–575.

[23] V. G. McDonell and G. S. Samuelsen. *Application of two-component phase doppler interferometry to the measurement of particle size, mass flux, and velocities in two-phase flows.* International Symposium on Combustion 22.1 (1989), 1961–1971.

[24] P. ORourke. *Collective Drop Effects on Vaporizing Liquid Sprays.* Department of Mechanical and Aerospace Engineering, Princeton University (1981).

[25] P. ORourke and A. Amsden. *The TAB method for Numerical Calculation of Spray Droplet Breakup.* SAE Paper 872089 (1987).

[26] M. Patterson and R. Reitz. *Modeling the Effects of Fuel Spray Characteristics on Diesel Engine Combustion and Emission.* SAE Paper 980131 (1998).

[27] B. E. Poling et al. *The properties of gases and liquids.* New York: McGraw-Hill, (2001). ISBN: 9780071455589, 0071455582, 9781591244790, 0070116822, 159124479X, 9780070116825.

[28] W. Ranz and W. Marshall. *Evaporation from drops Parts I and II.* Chem. Eng. Prog (1952).

[29] R. Reitz and R. Diwakar. *Effect of Drop Breakup on Fuel Sprays.* SAE Paper 860469 (1986).

[30] C. Salinas, D. A. Vasco, and N. O. Moraga. *Twodimensional nonNewtonian injection molding with a new control volume FEM/volume of fluid method.* International Journal for Numerical Methods in Fluids 71.12 (2013), 1509–1523.
[31] K. Satoh et al. *Development of Method for Predicting Efficiency of Oil Mist Separators.* SAE Technical Paper Series (2000).
[32] L. Schiller and A. Naumann. *Ueber die grundlegenden Berechnungen bei der Schwerkraftaufbereitung.* VDI Zeits (1933).
[33] D. P. Schmidt and C. J. Rutland. *A New Droplet Collision Algorithm.* Journal of Computational Physics 164.1 (2000), 62–80.
[34] F. Schmitt. *About Boussinesq's turbulent viscosity hypothesis: historical remarks and a direct evaluation of its validity.* Comptes Rendus Mecanique 335 (2007).
[35] F. G. Schmitt. *About Boussinesq's turbulent viscosity hypothesis: historical remarks and a direct evaluation of its validity.* Comptes rendus - Mcanique 335.9 (2007), 617–627.
[36] W. A. Sirignano and G. Tryggvason. *Fluid Dynamics and Transport of Droplets and Sprays.* Journal of Fluids Engineering 122.1 (2000), 190.
[37] D. B. Spalding. *A standard formulation of the steady convective mass transfer problem.* International Journal of Heat and Mass Transfer 1.2 (1960), 192–207.
[38] D. Stone. *Tetra Pak launches Tetra Evero Aseptic.* (2011).
[39] S. Subramaniam. *Lagrangian-Eulerian methods for multiphase flows.* PROGRESS IN ENERGY AND COMBUSTION SCIENCE 39.2-3 (2013), 215–245.
[40] S. Succi. *The Lattice Boltzmann Equation for Fluid Dynamics and Beyond.* Oxford University Press, New York (2001).
[41] H. S. team. *Hydrogen Peroxide, Human & Environmental Risk Assessment on ingredients of household cleaning products* (2005).
[42] Tetra Pak Campaign. *Tetra Evero Aseptic.* Accessed online 4-June-2013. (2013). URL: `http://campaign.tetrapak.com/life/content/images/downloads/Medium_TetraEveroAseptic_exploded_bottle.jpg`.
[43] Tetra Pak Campaign. *Tetra Pak A6 iLine.* Accessed online 4-June-2013. (2013). URL: `http://campaign.tetrapak.com/life/content/images/downloads/Medium_A6.jpg`.
[44] R. K. Theres Franke and H. Noppel. *The influence of cloud turbulence on droplet growth and precipitation.* International MetStrm Conference (2011).
[45] G. Tomar et al. *Multiscale simulations of primary atomization.* Computers and Fluids 39.10 (2010), 1864–1874.
[46] U.Engdar. *CFD modeling of turbulent flows in industrial applications with emphasis on premixed combustion in gas turbines.* Lund Institute of Technology, (2005).
[47] U.S Food and Drug Administration. *Substances Utilized To Control the Growth of Microorganism.* Code of Federal Regulations (2012).
[48] H. K. Versteeg and W. Malalasekera. *An introduction to computational fluid dynamics: the finite volume method.* Harlow: Pearson Prentice Hall, (2007). ISBN: 0131274988, 9780131274983.
[49] A. M. V.N Prasad. *LES Calculations of Auto-Ignition in a Turbulent Dilute Methanol Spray Flame.* Aeronautical and Mechatronic Engineering, University of Sydney (2006).
[50] F. White. *Heat and Mass Transfer.* Addison Wesley, 1988. ISBN: 9780201170993.
[51] J. O. Wilkes and S. G. Birmingham. *Fluid mechanics for chemical engineers: with microfluidics and CFD.* Upper Saddle River, N.J: Prentice Hall, (2006). ISBN: 9780131482128, 0131482122.
[52] Z. Yang. *Analysis of Lattice Boltzmann Boundary Conditions.* University of Konstanz (2007).